Electron Microscopy for Visualization of Interfaces in Adhesion and Adhesive Bonding

Shin Horiuchi

Abstract This chapter provides an overview of electron microscopy techniques to investigate interfaces in polymeric materials and adhesive bonds. First, how the instruments of energy-filtering transmission electron microscopy (EFTEM), scanning transmission electron microscopy (STEM), and scanning electron microscopy (SEM) work and are operated is briefly described. The principles of electron energy-loss spectroscopy (EELS) and energy-dispersive X-ray spectrometry (EDX), which are spectroscopic techniques associated with these instruments, are described. Next, the specimen preparation techniques, such as ultramicrotomy, heavy metal staining, focused ion beam (FIB) fabrications, and replica method, which are essential for these electron microscopy tasks, are introduced. This chapter also reviews advanced electron microscopy techniques, such as STEM-EDX-tomography, chemical phase mapping using electron energy-loss near-edge structure (ELNES), and in situ tensile TEM. Numerous examples of the application of these techniques to various surfaces and interfaces present in polymer alloys and composites, crystalline polymers, adhesive bonds, and metal substrate surfaces are presented.

Keywords EFTEM · STEM · SEM · EELS · ELNES · EDX · Tomography · Polymer blend · Composite · Interface

Supplementary Information The online version contains supplementary material available at https://doi.org/10.1007/978-981-99-4456-9_2. The videos can be accessed individually by clicking the DOI link in the accompanying figure caption or by scanning this link with the SN More Media App.

S. Horiuchi (✉)
Research Laboratory for Adhesion and Interfacial Phenomena (AIRL), National Institute of Advanced Industrial Science and Technology (AIST), 1-1-1, Higashi, Tsukuba 305-8565, Ibaraki, Japan
e-mail: s.horiuchi@aist.go.jp

S. Horiuchi et al. (eds.), *Interfacial Phenomena in Adhesion and Adhesive Bonding*,
https://doi.org/10.1007/978-981-99-4456-9_2

1 Instrumentation of Electron Microscopy

Studying interfaces in polymer and polymer/metal hybrid materials is crucial for developing adhesives, polymer blends and composites, and optoelectrical materials. These interfaces exist in various situations, such as laminates, between a matrix polymer and dispersed domains in the case of polymer blends and composites, and between hard substrates such as glass or silicon wafers in optoelectrical devices. However, accessing interfaces localized in various situations can be challenging. Identifying chemical interactions in buried interfaces is challenging as most surface analytical techniques have limited applicability. X-ray photoelectron spectroscopy (XPS) [1–4] and time of flight secondary ion mass spectrometry (ToF-SIMS) [3–5], combined with etching techniques, have been employed for the investigation of adhesive interfaces. XPS, which can detect signals from a depth of only a few nm and is sensitive to the chemical states of elements, has been frequently used to analyze thin surface structures [6–9]. However, XPS's lateral resolution is insufficient to resolve heterogeneous structures in the surface thin layer. To analyze buried interfaces non-destructively, sum frequency generation (SFG) spectroscopy [10, 11], infrared spectroscopy (IR) [12, 13], and scanning Kelvin probe (SKP) [14] have been used. Most studies have been performed with model samples that mimic the bonded interfaces, such as ultrathin polymer layers cast on metal, representative functional molecules adsorbed on metal, or metal thin films deposited on polymer substrate to serve as flat interfaces covered with a thin counter layer. Many experimental techniques, such as Rutherford backscattering spectrometry (BRS) [15, 16], forward recoil spectrometry (FRES) [17–23], neutron reflection (NR) [24–28], nuclear reaction analysis (NRA) [26, 29–31], rheometry [32, 33], X-ray reflectometry (XR) [34, 35], fluorescence spectroscopy (FS) [36, 37], dynamic light scattering (LS) [38], positron annihilation lifetime spectroscopy (PALS) [39], and nuclear magnetic resonance spectroscopy (NMR) [17, 40, 41], have been employed to study polymer/polymer interfaces. However, BRS, FRES, NR, and NRA cannot measure the concentration profile directly. Deuterated samples (or special preprocessing) are necessary, although these techniques have high resolution with a scale of angstrom. On the other hand, assumptions must be made for rheometry, FS, ellipsometry, XR, LS, and PALS to obtain corresponding interfacial concentration profiles. While IR and Raman spectroscopies provide helpful information at large interdiffusion depth in interfaces, they are limited by a depth resolution of ~0.1–1 μm.

The structures of materials used in industry are often complex, containing multiple phases or additives to achieve specific properties. As a result, industrial material interfaces can exist in various scenarios, making applying conventional techniques for their characterization challenging. Therefore, there is a need for a technique that can analyze interfaces without requiring special sample preparations. Electron microscopy, with its high spatial resolution, is a valuable tool for studying small structures. Recent advances in instrumental and analytical techniques have made it possible to observe and analyze small features of materials at atomic resolution. Electron microscopy is also a promising technique for understanding interfacial

phenomena in adhesion and adhesive bonding. Although current advanced electron microscopes are capable of atomic-scale imaging and analysis, the interfaces are difficult to be analyzed because they are buried inside materials in various situations. As mentioned in "Introduction—Interfaces in Adhesion and Adhesive Bonding" chapter, the interfaces in adhesion and adhesive bonding have multiple structures on a wide range of length scales from molecules to micrometer levels, such as chemical bonds, polymer chain entanglement, distributions of molecular weight and functional groups of polymers, crystallinity, and so on. The high spatial resolution capability of electron microscopy alone is insufficient to analyze such various structures. This chapter provides an overview of the instrumental and analytical techniques that electron microscopy can provide for analyzing metal/polymer and polymer/polymer interfaces.

An electron microscope irradiates a sample with electrons as an incident probe and detects various signals generated by interactions with the sample, thereby extracting information on the surface and internal structure of the sample. One of the characteristics of the electron is that it interacts with a specimen with high probability. The scattering probability (scattered electrons/incident electrons) is approximately 10,000 times that of X-rays, making it possible to obtain a large amount of structural information from a small region. Figure 1 shows various signal information generated by the specimen and electron beam interaction. By detecting and analyzing the signals from the target region, it is possible to know the atomic arrangement, composition, electronic state, etc. When high-energy primary electrons are incident on solid, various processes occur. In a thin specimen, the electron beam traverses the specimen, and the electron–solid interaction creates the signals. The elastic scattering involves no change in the energy of the primary electron, although there may be significant changes in direction. In transmission electron microscopy (TEM), elastic scattering is the major mechanism by which electrons are deflected and is the main contribution to diffraction patterns and images. Inelastic scattering involves a loss in the energy of the incident electrons. The energy analysis of the inelastically scattered electrons is the bases of electron energy-loss spectroscopy (EELS).

The signals created by the electron–solid interaction are divided into two groups. One is primary or direct processes and the other is secondary processes. The elastic and inelastic scattering are categorized to be the primary processes. Secondary processes occur due to electron–electron scattering and the subsequent de-excitation of atoms in the solid, which produce X-rays, Auger electrons, photons, etc. Secondary electrons (SEs) are the electrons that escape from the specimen surface with energies below about 50 eV. There are likely to be electrons bound initially to atoms in the specimen to which a small amount of energy has been transferred within a short distance of the surface. SEs are commonly used for imaging signals in scanning electron microscopy (SEM), providing topographic contrast from the specimen surface. Backscattered electrons (BSEs) are the primary electrons that undergo large deflections and leave the specimen surface with the remainder of their energy intact. Backscattered electrons are used for imaging and chemical phase identification in the SEM since their yield is sensitive to the atomic number of the specimen.

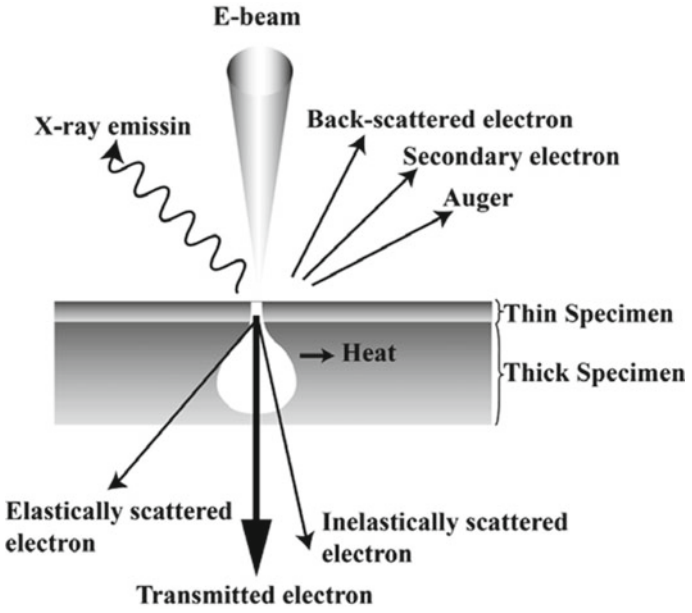

Fig. 1 Schematic diagram of the signals created during irradiation of a high-energy electron beam on a solid or transmission through a thin specimen

If an atomic electron has been ionized or excited to an empty higher energy level, the atom is in an excited, high-energy state. Subsequently, the empty electron state or hole will be filled by an electron dropping down from a higher occupied energy level and the atom will relax. The excess energy will be released via a secondary effect involving the emission of another particle or a photon of radiation. There are three ways in which this relaxation can happen: cathodoluminescence (photon), X-ray emission, and Auger emission (ejection of outer electrons). The distinct energy levels of atoms suggest that the energies of the X-rays released will have unique values for each atomic species within a sample. As a result, it is feasible to identify the specific elements located at the electron probe's position, which is the basis of energy-dispersive X-ray analysis (EDX).

Figure 2 illustrates the instrumental configurations of the three types of electron microscopes used in our studies.

(a) Energy-filtering transmission electron microscope (EFTEM).
(b) Scanning transmission electron microscope (STEM).
(c) Scanning electron microscope (SEM).

The applications of these electron microscopes will be shown in the following sections and "Interfacial Phenomena in Adhesion and Adhesive Bonding Investigated by Electron Microscopy" chapter. Here the imaging and analysis principles of

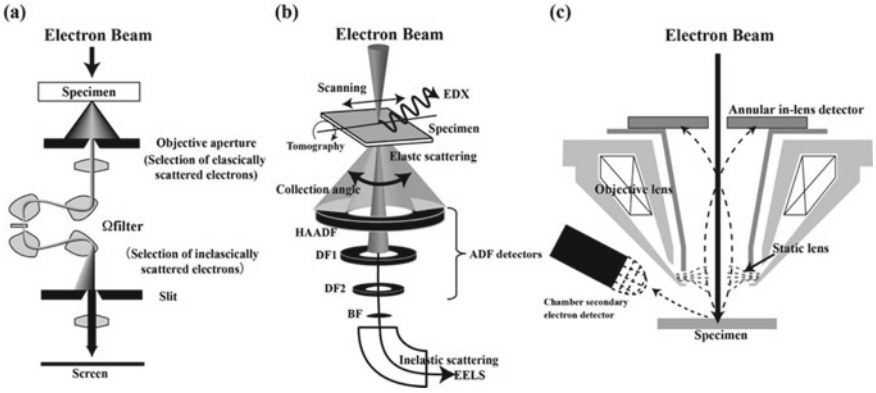

Fig. 2 Schematic diagrams of the configurations of the electron microscopes used in our works: **a** EFTEM, **b** STEM, and **c** SEM with two SE detectors

these instruments are briefly described. An electron lens in a conventional transmission electron microscope (CTEM) magnifies and creates images of elastically and inelastically scattered electrons produced when high-speed electrons pass through a thin film specimen. Image contrast and structural information can be obtained by selecting elastically scattered electrons according to the scattering angle using an objective aperture below a specimen. A viewer can see the image on the fluorescent screen below the projector lens, which converts the electron to visible light. In CTEM, the scattered electrons used for imaging are selected only via the objective aperture according to their scattering angles. Therefore, only electrons with large scattering angles contribute to contrast generation and enough contrast cannot be expected for imaging polymer specimens composed of light elements. Despite the significant impact on contrast and resolution caused by the chromatic aberration of the objective lens, the energy differences of the electrons and their variations are still not accounted for.

In EFTEM, the transmitted electrons are not only selected according to their angle but also to their energy [42, 43]. An energy filter (Ω filter) disperses the inelastically scattered electrons according to their energy. As a result, an EELS spectrum is imaged below the filter and can be seen on the screen. By insertion of a slit of variable width at the point where the EELS spectrum is formed, they are then selected for imaging with an energy loss and a defined energy width. Dual electron selection results in considerably enhanced contrast. By imaging energy-selected electrons, new information can be obtained with contrasts such as the structure-, thickness- and element-specific contrast. In addition, elemental mapping with rapid acquisition and high lateral resolution is capable of electron spectroscopic imaging (ESI). As the filter is integrated into the middle of the TEM column between the objective and projector lenses, this is called an in-column-type EFTEM. Another type of EFTEM is a post-column type, in which the filter is attached to a CTEM at the bottom below the fluorescent screen. An advantage of the in-column type over the post-column is

the possibility of seeing the energy-filtered image directly on the screen, making it easier for the viewer to find objects of interest in a specimen.

In STEM, the electron beam is focused on a spot and is scanned across the specimen area to be investigated while the transmitted electrons are collected [44]. The elastically scattered electrons are collected in the three annular dark-field (ADF) detectors which can collect the elastically scattered electrons according to the scattering angles. The bright-field (BF) detector, which is located at the lowest position in the array of detectors, collects the unscattered electrons and the scattered electrons with low scattering angles. Those four imaging detectors allow us to acquire images with different contrast simultaneously and obtain the desired contrast. Two types of spectrometers are equipped: EELS and EDX. An EDX spectrometer is located above the specimen. A post-column-type EELS spectrometer is attached to the bottom of the column, enabling the simultaneous recording of EDX and EELS spectra at a point of interest. It also can perform tomography for 3D visualization of the internal structures of a thin section. A series of tilted images with tilt angles ranging from $-60°$ to $+60°$ can be acquired and reconstruction generates a 3D volume within a specimen.

In SEM, the focused electron beam scans line by line over the surface of the specimen and forms signals based on the interactions between the beam and the specimen. The electrons interact with atoms in the specimen, producing various signals that contain information about the specimen's surface topography and composition. As stated above, SEM imaging uses SEs and BSEs emitted from the surface of the specimen. The contrast formation in the BSE mode is mainly determined by the atomic number (material contrast). In contrast, the contrast in the SE mode is primarily determined by the local inclination of the specimen surface with respect to the incident beam (topographic contrast). This effect of the SE on SEM imaging is called as "edge effect". In polymeric materials, the BSE mode cannot be expected; thus, the SE mode is mainly used for imaging the topographic features of surfaces. As described in Fig. 2c, the column of the SEM instrument used in our study integrates two detector systems for the collection of the SE signals: One is a conventional scintillator-type detector located outside the objective lens with a positively biased grid, and the other is an annular type positioned above the objective lens "on-axis". Those two detectors are called the "chamber detector" and the "in-lens" detector. The electrostatic lens formed at the entrance of the objective lens accelerates the SE electrons backward and directs them into the in-lens detector. The SE signals can be separated from BSE, which may not reach the detector because the higher kinetic energy causes different trajectories. Combining the chamber and the in-lens detectors is advantageous for low-voltage SEM imaging. As mentioned in Sect. 6, SE imaging with the two-detector system allows us to perform energy-filtered surface imaging, which offers the opportunity for high-resolution surface imaging of polymer specimens.

2 Analytical Electron Microscopy—EDX and EELS

Electron microscopes offer high-resolution imaging and elemental microanalysis, owing to element-specific electron scattering. Both energy-dispersive X-ray analysis (EDX) and electron energy-loss spectroscopy (EELS) are based on the fact that each element has a unique atomic electronic structure, and the primary electron can excite electrons on a particular shell of atoms. As illustrated in Fig. 3a, when high-energy electrons hit an atom's inner shell, an electron may be ejected, creating an electron hole. The energy difference between the outer and inner shells is then released as an X-ray. The energy of these X-rays is characteristic of the energy difference between the two shells and the atomic structure of the emitting element. An energy-dispersive spectrometer can measure the number and energy of X-rays emitted from a specimen. Thus, EDX allows for the determination of the specimen's elemental composition. Figure 3b depicts a typical EDX spectrum obtained from an STEM mode image of an aluminum 6061 alloy, providing an overview of the sample's elemental composition. The spectrum contains characteristic peaks for the excited atoms and a background continuum with low background contribution compared to EELS spectra.

In STEM-EDX, signals can be collected over a specimen area by sequential data collection, enabling the intensity of characteristic signals to represent the sample's local composition variation, as displayed in an elemental map.

The energy that primary electrons lose due to inelastic scattering is measured in EELS. Figure 4 shows a typical EELS spectrum, which presents the intensity of electrons as a function of energy loss. When a sample is thinner than the mean free path for inelastic scattering, the most noticeable aspect of the EELS spectrum is the zero-loss peak (ZLP) at 0 eV. This peak contains all elastically scattered electrons. The low-loss region of the EELS spectrum, which extends up to around 50 eV,

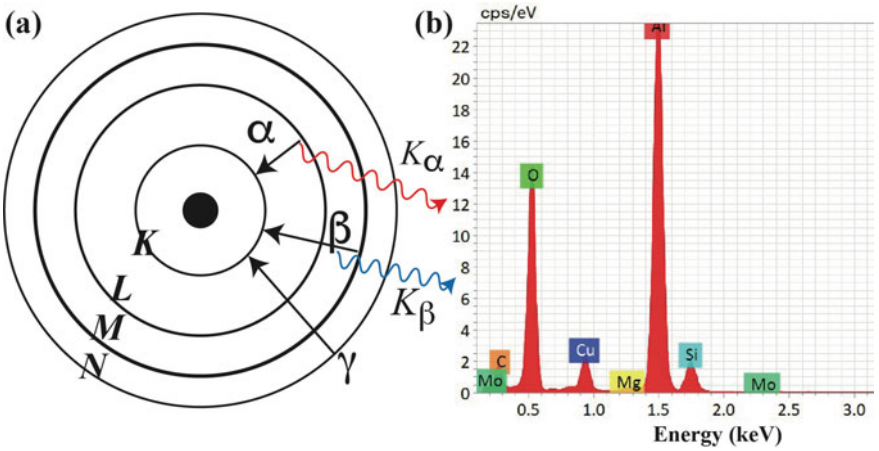

Fig. 3 De-excitation mechanisms for an atom that causes the characteristic X-ray emission from electron irradiation (**a**) and STEM-EDX spectra taken from aluminum 6061 alloy (**b**)

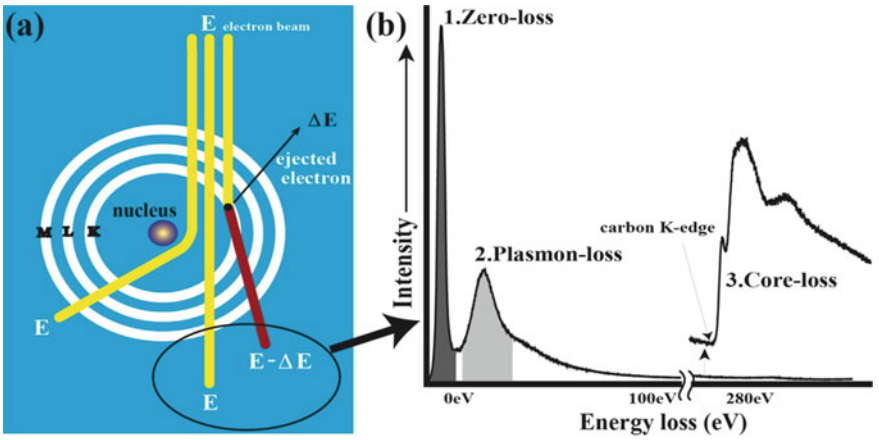

Fig. 4 Schematic diagram showing the process of the inelastic scattering and ionization of inner shell (**a**) and a typical EESL spectrum presenting zero-loss, plasmon-loss, and core-loss peaks (**b**)

corresponds to the excitation of weakly bound outermost atomic orbital electrons. This region is primarily characterized by plasmons caused by the valence electrons' resonant oscillations. It is mainly utilized to determine the thickness of the sample and correct for multiple inelastic scattering when performing quantitative microanalysis on thicker specimens.

In contrast, the high-loss region, extending from 50 eV to several thousand eV, corresponds to the excitation of electrons from well-localized orbitals on a single atomic site to unoccupied energy levels. This region reflects the atomic character of the specimen, with edges indicating the ionization of inner shell electrons and peaks known as core-loss peaks. The intensity of this region decreases monotonically, and gain changes are typically inserted in the linear intensity scale. EELS is beneficial for analyzing light elements such as those found in polymer samples, as the energy of an edge is determined by the binding energy of a particular electron shell, allowing for the identification of the atomic type [45]. Generally, the K-shell ionization edge of carbon (C K-edge) appears at around 285 eV as shown in Fig. 4b. The nitrogen and oxygen K-shell ionization edges appear at about 410 and 535 eV, respectively. The intensity under an edge is proportional to the number of atoms present, allowing for quantitative analysis.

The electron energy-loss spectroscopy (EELS) technique enables the identification of a compound's chemical state and nature by analyzing the fine modulations in the higher energy-loss region beyond the ionization edge, which typically spans an energy width of 50–100 eV. These modulations are referred to as electron energy-loss near-edge structures (ELNES), and they provide information about the electronic and bonding environment of the excited atom [46–48]. Figure 5 depicts typical examples of ELNES obtained from aluminum compounds. The EELS spectra of oxygen-containing aluminum compounds are presented in three energy-loss regions: (a) the plasmon loss, (b) Al L_{23-}, and (c) O K-edges. The powder samples of metallic Al,

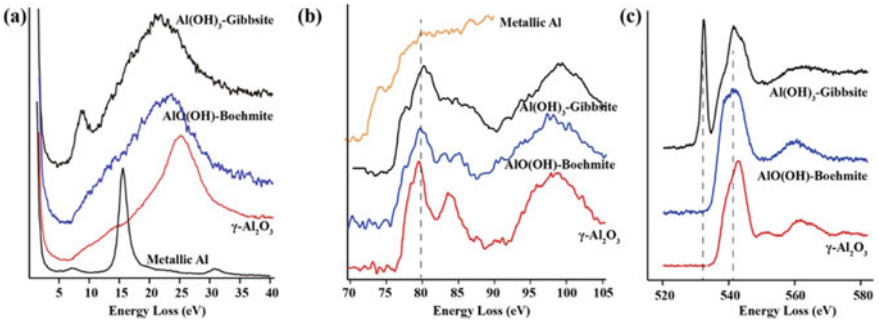

Fig. 5 EELS spectra of aluminum compounds obtained from the powder samples of metallic Al, $Al(OH)_3$ (gibbsite), AlO(OH) (boehmite), and γ-alumina: **a** plasmon-loss region; **b** Al L_{23}-edge; **c** O K-edge. All the spectra except the plasmon-loss spectra are presented after the background substruction by fitting the pre-edge regions with the power law function

γ-alumina (Al_2O_3), boehmite (AlO(OH)), and aluminum hydroxide ($Al(OH)_3$) were used to obtain these spectra, which were collected from multiple points (10 × 10 points) in the STEM mode, energy-drift-corrected, and summed into a single spectrum. The O K-edge ELNES features of the three oxygen-containing compounds show distinct differences. γ-alumina has two maxima at 550 and 563 eV energy losses, followed by a major peak at 542 eV. Boehmite has a broadened first peak, followed by only one maximum at an energy loss of 560 eV, and $Al(OH)_3$ exhibits an intense peak at 532.6 eV, followed by two maxima at energy losses of 540 and 560 eV. Thus, the O K-edge ELNES features can be used as unique identifiers to determine the chemical compositions of aluminum compounds. However, the ELNES features in these compounds are not yet fully understood [49].

The intensity of the core-loss ionization edge in an EELS spectrum relative to the background is highly dependent on the thickness of the analyzed region, making the edge less detectable as the sample thickness increases. Therefore, the specimen must be thin to obtain chemical information by ELNES. EDX; on the other hand, tolerates thicker specimens and the background signals in the EDX spectrum are much lower than those in EELS, even though EDX background signals increase with increasing specimen thickness. The energy resolution of EDX detectors is typically 100–150 eV, which gives rise to peak overlap at low X-ray energies and precludes any chemical state information. EDX suffers from severe spectral resolution issues when dealing with compounds that have overlapping X-ray lines. This issue is not present in EELS, which is generated by the primary event of energy loss, providing an advantage over EDX. In EDX, signal intensity is linked to the secondary fluorescence process resulting from de-excitation via X-ray emission, which is not the case with EELS. Therefore, the spectral energy resolution of EELS is significantly higher than that of EDX. We generally perform EDX analysis for the quick survey of the elemental composition in a region of interest (ROI) in a specimen. In contrast, EELS is performed for the detailed chemical analysis of an element of interest involved in the ROI.

3 Specimen Preparation

3.1 Preparation of Thin Sections by Ultramicrotomy

For the electron microscopic investigations by TEM and STEM, specimens must be thin enough for the electron beam to transmit to obtain fine images and reliable microanalysis. In TEM and STEM, preparing thin sections of uniform thickness and free from artifacts is a key issue for achieving reliable results. Thin sections from polymeric bulk samples are commonly prepared by ultramicrotomy. Ultramicrotomy is a standard method for preparing ultrathin sections (<100 nm) and flat surfaces for polymeric materials. This method allows high-throughput sample preparation and is also sample-friendly compared to other techniques, such as focused ion beam (FIB) fabrication. The traditional application of ultramicrotomy involves the sectioning of soft materials. Even metallic materials, however, like aluminum, copper, magnesium, titanium, and steel, have been successfully sectioned by ultramicrotomy. The key to achieving artifact-free successful sectioning lies in the experience of the experimentalist rather than the instrumentation used. It is crucial to master the optimal specimen preparation and sectioning technique while understanding the materials to be cut. The general procedure for specimen preparation by ultramicrotomy has been described in detail in the literature [50, 51]. Here, the technical topics for the sectioning of surfaces and interfaces in metallic and polymeric samples are reviewed.

Figure 6a shows the appearance of an ultramicrotome apparatus and Fig. 6b shows the inside of the ultramicrotome where a sample holder (left part) and the diamond knife (right part) are fixed. The diamond knife is supplied with a trough to be filled with water. The sample holder approaches the knife at a given distance while repeating vertical movement. During the downward motion of the sample holder, a section is produced and simultaneously floats on the water filled in the knife's trough. After sectioning the sample, the sample holder moves backward and then rises to the position where the next sectioning starts. Before the sectioning with an ultramicrotome, the sample must be trimmed to serve a cutting surface with an appropriate area and shape. Before the sectioning with an ultramicrotome, the specimen is trimmed to create a square plane of 0.3 mm or less on the tip of the pyramidal specimen, as shown in Fig. 6c. Figure 7 is a video demonstrating the sectioning procedure. The section is connected to the one cut during the previous cutting cycle, and several sections are connected and lined up. The sections can be picked up easily onto a copper grid on the water surface in the trough. The surface must be trimmed smoothly on all sides with a fresh glass knife on an ultramicrotome to obtain serially thin sections in a desired thickness, as shown in the video. The size and shape of the trimmed surface should be optimized by watching the cutting behavior.

Sections cut in a uniform thickness exhibit interference color reflecting the thickness of the sections as shown in Fig. 8. The thickness can be estimated from the interference color of the section floating on the water surface as shown in the table (right panel in Fig. 8). Suitable sections for TEM/STEM are silver- or gray-colored sections.

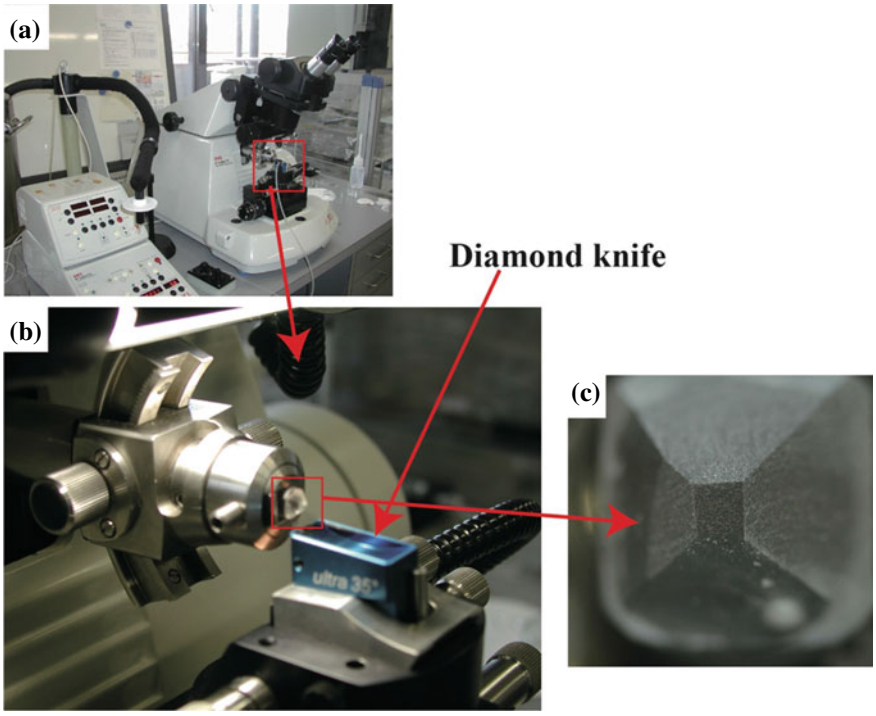

Fig. 6 Appearance of the ultramicrotome apparatus (**a**) used in this work, the specimen holder, and the diamond knife fixed in the ultramicrotome (**b**). **c** A cutting face created in a square plane of 0.3 mm on the tip of the pyramidal specimen

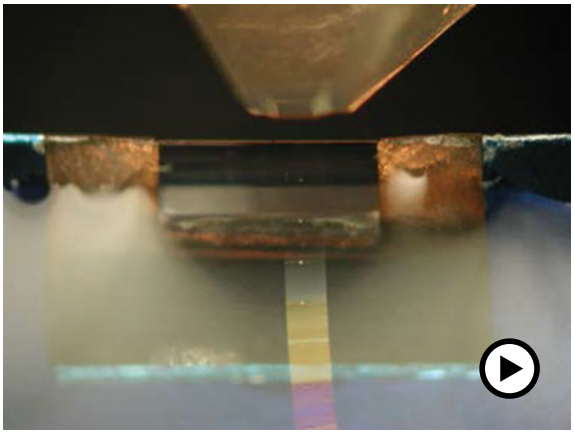

Fig. 7 Video demonstrating the sectioning procedure by ultramicrotomy. The width of the diamond knife is 1.5 mm (► https://doi.org/10.1007/000-aye)

Interference color	Section Thickness (nm)
Gray	<60
Silver	60~90
Gold	90~150
Purple	150~190
Blue	190~240
Green	240~280
Yellow	280~320

Fig. 8 Serial thin sections floating on water with different thicknesses prepared by ultramicrotomy (*left*) and the relationship between section thickness and interference color (*right*)

To observe a cross section of a substrate's surface thin skin layer or the interfacial region in a laminate, the samples are commonly cut where the angle between a cutting face and a surface/interface plane is adjusted at 90°. When specimens are cut like this, the two-dimensional (2D) image projection cannot observe the interface detail due to the overlapping of three-dimensional (3D) structures within the regions. To resolve this problem, specimens are prepared by oblique cutting of the surface/interfacial plane, resulting in the regions' oblique projections. Figure 9 shows a typical example of the sample setup and the preparation of a cutting surface for the oblique sectioning of the aluminum surface oxide layer with a defined angle. An aluminum plate is a preliminary cut into a roof-like shape. It is fixed on a cylindrical plastic base that has been obliquely cut at an angle of 60° or more, with the aluminum surface facing up. The cutting face is then created by trimming the tip of the roof horizontally. Figure 10 is a video demonstrating the oblique sectioning of aluminum 6061 alloy surface where thin serial sections are floating on the water filled in diamond knife's trough. Figure 11 shows STEM-HAADF (high angle annular dark field) images, indicating the comparison between the cross section and the oblique section of the interface between aluminum and adhesive [48]. As depicted in the insets, the projection of the interface in the oblique section shows a thinner aluminum surface region, allowing us to see the structural details regarding the roughness and porous nature of the aluminum skin layer.

Cryoultramicrotomy is required when the sample is too soft, like a rubber material, or when the sectioning at room temperature causes severe deformation of structural

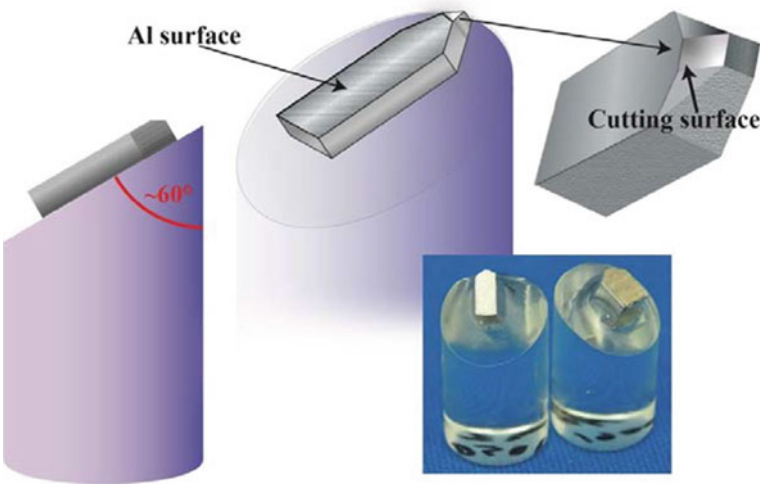

Fig. 9 Schematic illustration and the actual samples showing the process for the oblique sectioning of an aluminum surface by ultramicrotomy

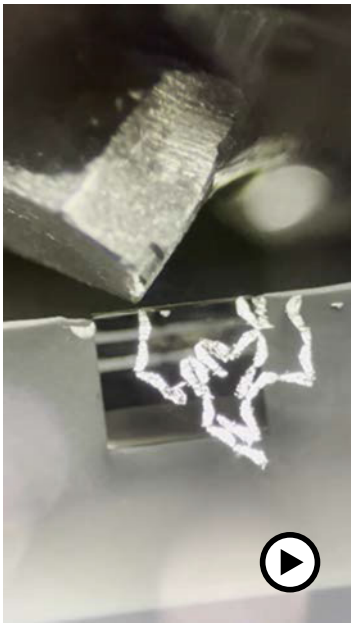

Fig. 10 Video presenting the oblique sectioning of aluminum 6061 alloy surface where thin sections float on the water filled in diamond knife's trough (► https://doi.org/10.1007/000-ayc)

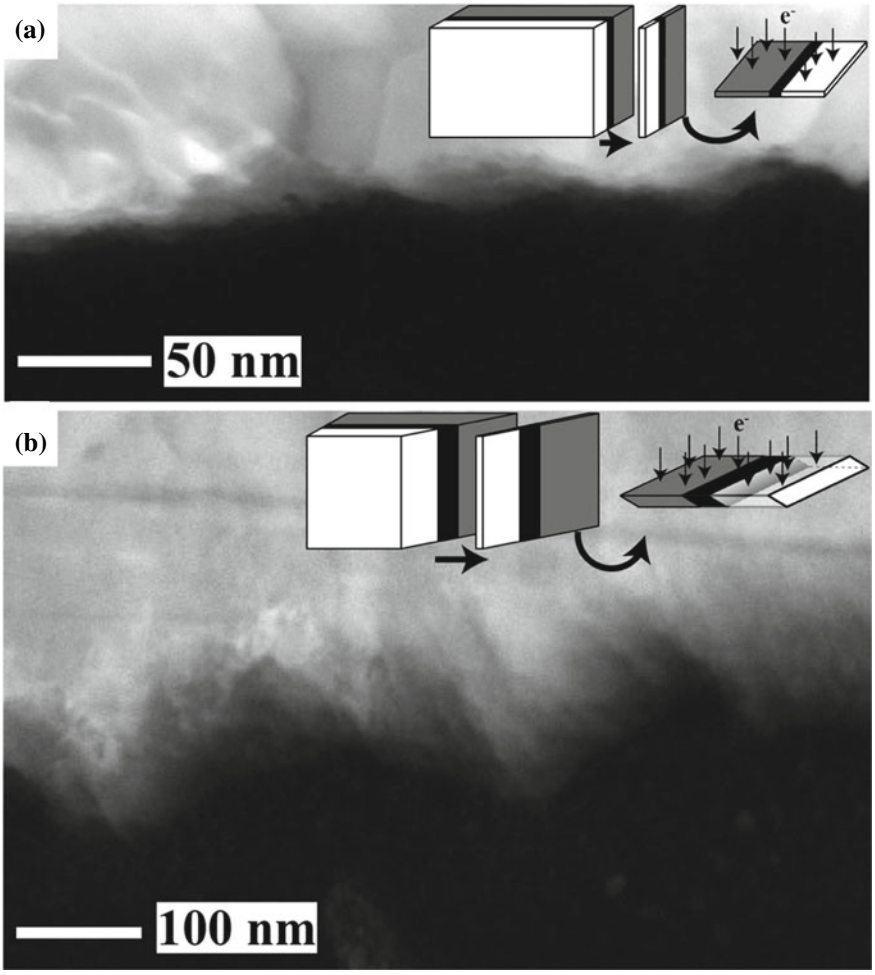

Fig. 11 STEM-HAADF images of a cross (**a**) and an oblique (**b**) sections of aluminum adhesive interface. The insets depict the planes of sections obtained by cross and oblique sectioning. Reprinted with permission from Ref. [48]. Copyright 2022, Elsevier. All Rights Reserved

details. The cryo-chamber is attached to the ultramicrotome as shown in Fig. 12, which is cooled by liquid nitrogen at a controlled temperature down to −185 °C. The sectioning under a cryogenic temperature is carried out with a diamond knife, and the collection of sections is performed either in the presence of a floating liquid (wet sectioning) or on the surface of the knife (dry sectioning). For wet sectioning, ethanol can be used down to −100 °C, while in the dry sectioning, the sections are transferred directly onto a grid.

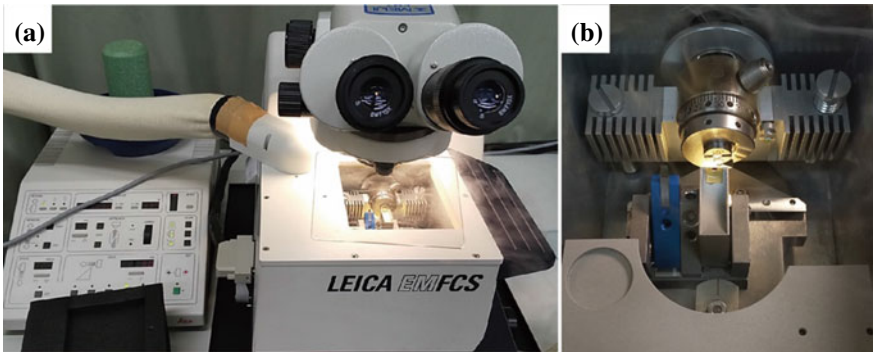

Fig. 12 The appearance of the cryo-ultramicrotome equipment (**a**) and the interior of the cryo-compartment (**b**) with two diamond knives for trimming (*left*) and wet sectioning (*right*)

3.2 Staining

Image contrast acquired in the conventional TEM (CTEM) results from variations in electron density in the structures present. Most polymers are composed of low atomic number elements, and thus they exhibit slight variations in electron density. The morphological observation of polymeric samples by CTEM requires appropriate staining to introduce a heavy atom into specific structures in a specimen. In addition to enhancing contrast with staining, staining serves the important function of fixing and hardening polymeric materials. This effect of staining enables the sectioning of soft materials by ultramicrotomy with the preservation of structural details. Staining can also increase specimen stability against electron beam irradiation to maintain the structural dimensions of the specimens. Two staining agents have been widely used for polymer staining: osmium tetroxide (OsO_4) and ruthenium tetroxide (RuO_4) [52]. Different procedures have been known for selective staining, either on the bulk materials before sectioning, called "block staining" or on the thin sections after cutting, called "section staining". Several TEM and STEM images taken with different sectioning and staining procedures are presented as examples. We can see in these images the interfacial regions in heterogeneous polymer systems such as polymer blends, block copolymers, and semicrystalline polymers.

OsO_4 reacts to the carbon–carbon double bonds in unsaturated rubber phases, which cross-links the polymer chains as indicated in Scheme 1. OsO_4 can enhance the contrast in TEM by the increased electron scattering of the heavy atom in the rubber phase compared with the unstained matrix. It also enhances the hardness and stiffness of the rubber phase. It thus allows the sectioning of the samples at room temperature by ultramicrotomy without the loss of the rubber phase.

Scheme 1 The chemical reaction between OsO_4 and unsaturated rubber polymers

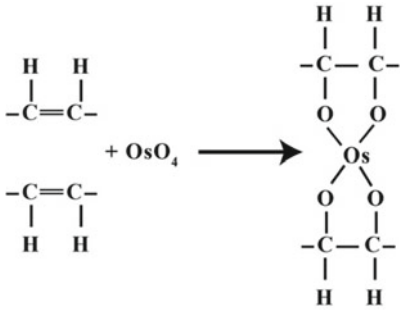

3.2.1 Observation of an Interface Between ABS and Copper-Plated Film by OsO_4 Staining

For the fixation and staining of a polymer sample containing a rubber phase, the sample is stained with OsO_4 by the block staining. The sample is preliminarily trimmed to create the cutting face for ultramicrotomy, as shown in Fig. 6c. The trimmed blocks are placed in a glass container with a small amount of OsO_4, sealed well, and stained with the OsO_4 vapor for a specific time and temperature. The vaporized OsO_4 penetrated the sample surface and the region below the surface with a depth of several microns to several tens of microns can be stained. Therefore, one must carefully approach the diamond knife to the cutting face to avoid cutting off the stained part before collecting the thin sections in ultramicrotomy. Figure 13 is a STEM bright-field (BF) image showing a cross section of acrylonitrile–butadiene–styrene (ABS) with a copper foil deposited by electroless plating. ABS is a multi-component polymer containing the polybutadiene (PB) domains distributed in the acrylonitrile-styrene (AS) random copolymer matrix. The sample was stained with OsO_4 after trimming at 60 °C overnight and was cut into a thin section with about 70 nm thickness by ultramicrotomy at room temperature. The sectioning direction is horizontal in the image, which the shallow knife marks on the copper side can identify. The knife marks are produced in the section due to the diamond knife's edge damage. When this is the case, ridges on the surface of the section are created along the sectioning direction. In the ABS part (top in the micrograph), the stained PB domains with the occluded unstained AS particulates are distributed in the AS matrix. The sectioning seems to be carried out successfully because no deformation of the PB domains along the cutting direction was recognized. For electroless plating on the ABS plate, the PB domains on the surface were etched with chromic acid to create holes on the surface filled with copper. As shown in the inset, it can be confirmed that Pd nanoparticles, which act as a catalyst for electroless plating, are adsorbed on the entire ABS surface at high density. As a result, copper plating starts evenly from the ABS surface, which fills the holes on the ABS surface, and excellent adhesion was achieved due to an anchoring effect.

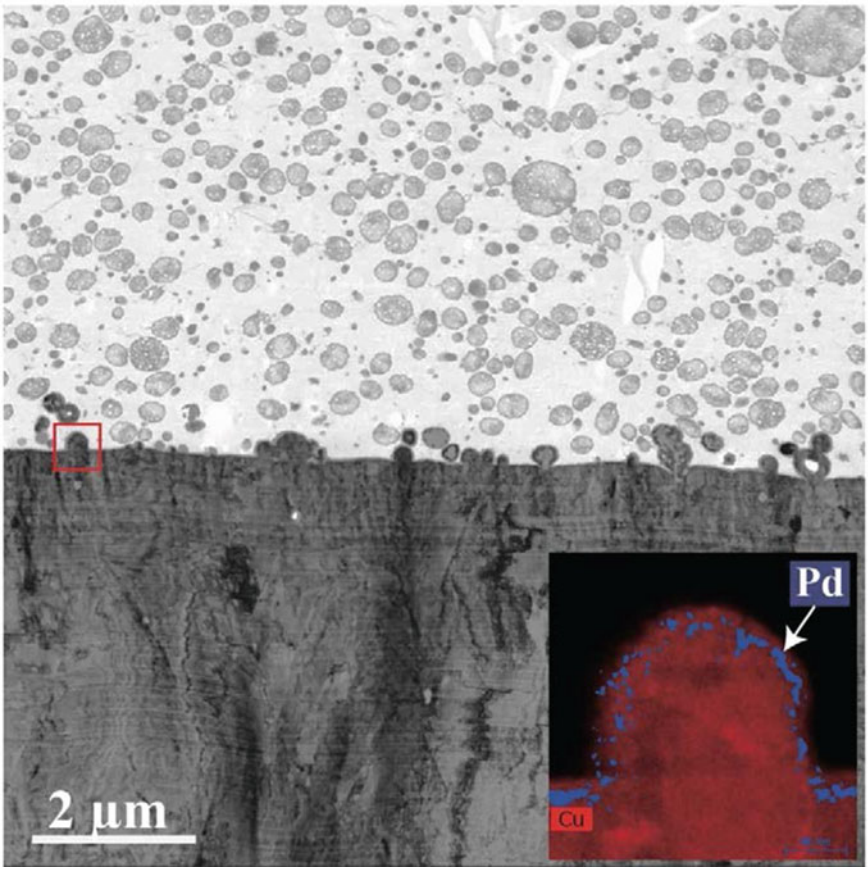

Fig. 13 STEM-BF image showing the OsO_4-stained polybutadiene domains dispersed in ABS polymer (*upper part*) and the copper foil deposited by electroless plating on a chromate-etched ABS plate (*lower part*). The inset shows the STEM-EDX elemental map showing the distribution of copper (red) and palladium (blue) in the interfacial region indicated as a red box

3.2.2 Observation of Lamellar Structures in Semicrystalline Polymers by RuO_4 Block Staining

RuO_4 is a stronger oxidizing agent than OsO_4 [53]. The staining mechanism of RuO_4 is different from that of OsO_4. RuO_4 does not react directly to polymers as OsO_4 can crosslink the C=C double bonds in unsaturated polymers, while it forms ruthenium-containing clusters instead. RuO_4 can stain both saturated and unsaturated polymers that contain in their unit structure ether, alcohol, aromatic, or amide moieties. Most polymers, therefore, can be stained with RuO_4, except poly(methyl methacrylate) (PMMA), poly(vinyl chloride) (PVC), poly(vinylidene fluoride) (PCDF), and poly-acrylonitrile (PAN). As shown in the following three examples, RuO_4 can stain most polymers, but the degree of the staining varies depending on the structures of the

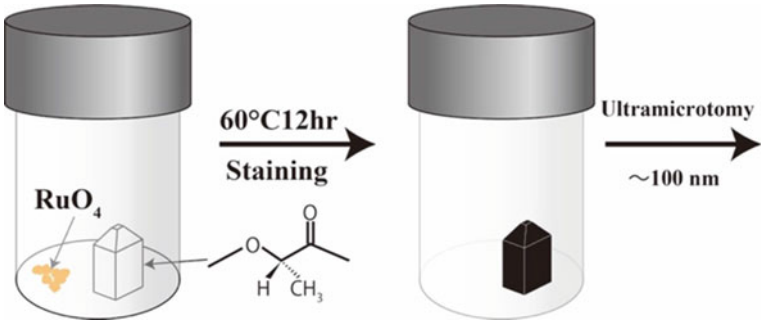

Fig. 14 Schematic illustration for the block staining of a trimmed polymer sample (L-PLA)

polymers investigated. Polyolefin with no functional groups such as polyethylene (PE) and polypropylene (PP) can be stained, where RuO_4 diffuses preferentially into the amorphous regions and stains them in semicrystalline structures, whereas the crystalline regions remain unstained. Therefore, the lamellae in semicrystalline polymers can be visualized by the RuO_4 staining.

The samples were stained by RuO_4 vapor at 60 °C overnight before ultramicrotomy and were then cut into about 70 nm thick sections, as illustrated in Fig. 14. The RuO_4 vapor may diffuse into the amorphous part preferentially, allowing the sectioning at room temperature without losing structural details. Figures 15 and 16 show TEM micrographs showing typical lamellar structures of semicrystalline polymers observed in interfacial regions by the selective RuO_4 staining. Figure 15a, b shows the spherulitic texture and the lamellae in a spherulite of L-polylactic acid (L-PLA), respectively. PLA is inherently slow to crystallize. If the annealing time inside the mold in injection molding is limited, the growth of spherulites terminates in the middle of the crystallization from the melt. As a result, the amorphous phase remains between nearby spherulites. As a result, the sample exhibits a morphology in which spherulites with several tens of microns diameters are dispersed in the amorphous phase, as shown in Fig. 15a. Spherulite is a typical crystal form of semicrystalline polymers, which is usually formed under the quiescent condition as organized lamellae growing in the radial direction from the spherulite's center. When the lamellae grow outward from the center, they twist around the radius with helical configurations. The texture of the spherulites shown in the TEM micrograph may represent such a lamellar arrangement in a spherulite. Figure 15b is a high-magnification image showing the border between a spherulite and the amorphous phase. The selective staining of the L-PLA allows the lamellae to be visible as loosely packed thin filaments, which represent the transformation of the polymer chains from random coils to crystalline lamellae at the forefront of the growing spherulite toward the amorphous region.

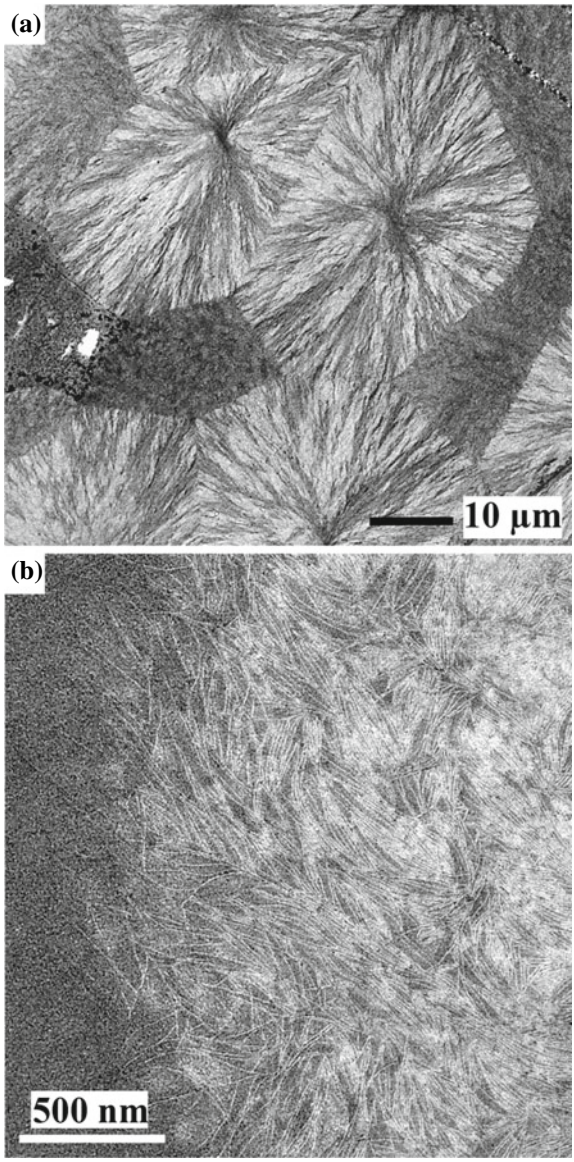

Fig. 15 TEM micrographs of L-PLA: **a** spherulites formed in the crystallization from the melt; **b** lamellae grown at the forefront of the spherulite's growth

Figure 16 is an STEM-BF image showing the lamellae of isotactic PP (*i*PP) in the interfacial region, where an epoxy adhesive bonds to the *i*PP surface. As shown in the inset, the interlamellar amorphous region exists between the stacked lamellae in which the folded segments in a polymer chain are arranged parallel to the neighboring segments. These amorphous layers can be selectively stained, making the lamellae visible as the unstained region. Since the characteristics of the lamellae in contact with

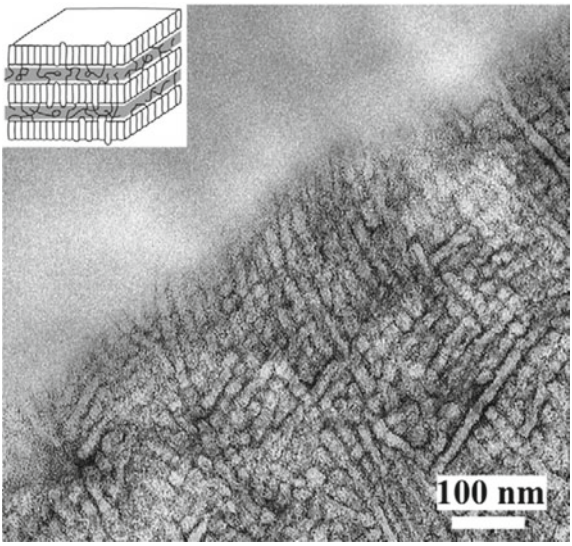

Fig. 16 STEM-BF image showing the interfacial lamellar structure of *i*PP bonded to an epoxy adhesive. The inset illustrates the selective staining with RuO_4 of the interlamellar amorphous regions between the stacked lamellae

the adhesive are believed to affect the bonding properties greatly, we are concerned with the interfacial lamellar structures of *i*PP in terms of the orientation, length, width, and disordering to clarify the bonding mechanism, which will be described in Sects. 4 and 5 of "Interfacial Phenomena in Adhesion and Adhesive Bonding Investigated by Electron Microscopy" chapter.

3.2.3 Observation of Multi-phase Structures of a Polymer Blend by RuO_4 Section Staining

As an alternative to "block staining", one can also directly stain sections of the samples. Ultrathin sections are stained using vapor of OsO_4 or RuO_4. The staining of thin polymer sections occurs quite rapidly compared to "block staining". This method sometimes gives better results for polymer samples with complex phase-separated structures with multiple polymer components. Interfaces existing in the phase-separated structures of multi-component polymer materials are the issues to be highly concern for studying structure–property relationships of polymeric materials. Direct observation and analysis of interfaces localized in multi-phase polymer materials by TEM or STEM would be the promising approach for investigating the mechanism of outstanding properties that cannot be obtained in single-component materials. Melt blending of polyamide 6 (PA6), poly-(2,6-dimethyl-1,4-phenylene oxide) (PPO), and SEBS has complicated multi-phase morphologies. SEBS is an ABA triblock copolymer comprising of the polystyrene (PS) end blocks and the ethylene-butylene (PEB) mid-block as shown in Scheme 2 (top part), which has been used for a thermoplastic elastomer. SEBS can be functionalized by grafting maleic anhydride (MA) to the PEB mid-block (middle part in Scheme 2), which can

react to the $–NH_2$ terminal group of PA6 during the melt blending. The in situ chemical reaction between PA6 and SEBSgMA with 10–20 wt% SEBSgMA contents causes a remarkable reduction of the SEBS domain size, resulting in an impact strength approximately 20 times higher than PA6 [54]. PA6 and PPO, on the other hand, are incompatible and the simple blending of those two polymers results in poor mechanical properties due to the poor dispersion of the minor component and the poor interfacial strength between the matrix and the domains. The addition of SEBSgMA to the PA6/PPO (75/25 wt/wt) incompatible blend causes the localization of the SEBS elastomer phase at the PA6/PPO interface, as shown in Scheme 2 (bottom). This is because the combination of PS and PPO is a rare pair thermodynamically miscible in all compositions and temperatures. When the three polymers are melt-blended simultaneously, PA6 and SEBSgMA react to form a graft copolymer through imidization, while the PS block of SEBS penetrates the PPO phase. As a result, SEBS molecules are localized to the PA6/PPO interface and reinforce the interfaces.

The ternary PA6/SEBSgMA/PPO blend has a complicated heterogeneous multiphase structure. Sectioning by ultramicrotomy for TEM investigation may cause distortion to the shape of the dispersed domains and the interfaces involved in the

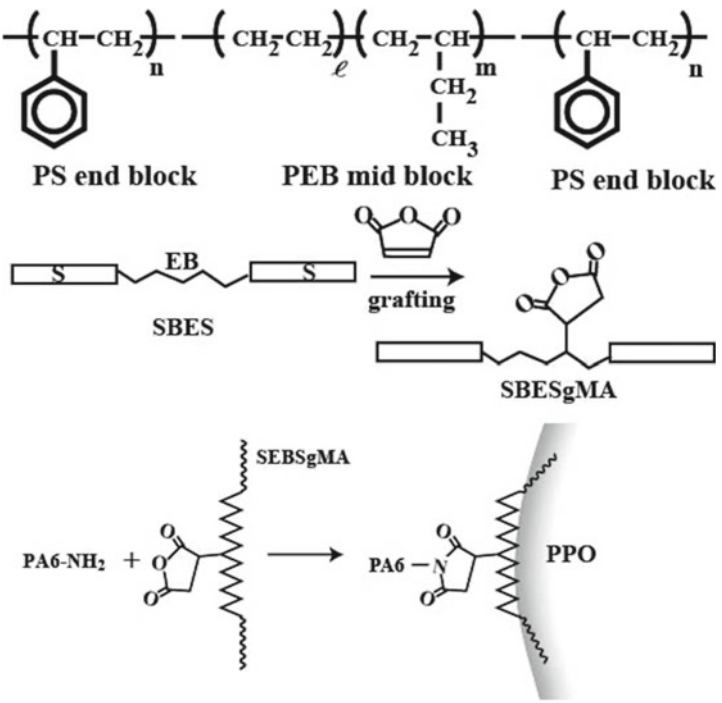

Scheme 2 Chemical structure of SEBS (*top*), graft of MA onto the EB mid-block in SEBS (*middle*) and reaction between PA6 and SEBS*g*MA, and the localization of the PA6-SEBS*g*MA graft copolymer at PA6/PPO interface (*bottom*)

blend, so great care must be taken when preparing thin sections to preserve the original morphological features. For this purpose, sectioning by cryo-ultramicrotome followed by "section staining" is the best way to achieve reliable results. The wet sectioning with ethanol obtained the thin sections about 100 nm thick under a cryogenic condition at −100 °C. Then the sections were stained with the RuO_4 vapor for 15 min. Figure 17 presents TEM micrographs showing the morphological structures. The staining was successfully employed to show the three phases with different contrast, as shown in Fig. 17: The PS domain of SEBS is the most intensely stained, and the PPO domain is the second most intensely stained. The PA6 matrix phase is less intensely stained, but the selective staining of the amorphous phase makes the lamellae visible, as shown in Fig. 17b. Figure 17b is a high-magnification image focusing on the interfacial region: A large number of SEBS domains are dispersed in the PA6 matrix, representing the nanodomain structure of a block copolymer where the stained PS domains and the PEB phases are arranged periodically with the distance of about 10 nm, and also the SEBS phase surrounds the PPO domains with the 10-nm-thick thin layer. It can also be found that a small number of SEBS domains are distributed in the PPO domains; this is caused by the micellization of the SEBS in the PPO domains. During the melt blending, a certain amount of SEBS*g*MA escapes from the interface toward the PPO domains instead of the reaction to PA6 due to the high miscibility of the PS and PPO. It can be confirmed that the dispersion of the SEBS domains in the PA6 matrix may enhance the impact resistivity of the PA6 matrix. At the same time, forming the SEBS thin layer at the PA6/PPO interface can improve the toughness of the interface. SEBSgMA acts as a compatibilization for the PA6/PPO blends.

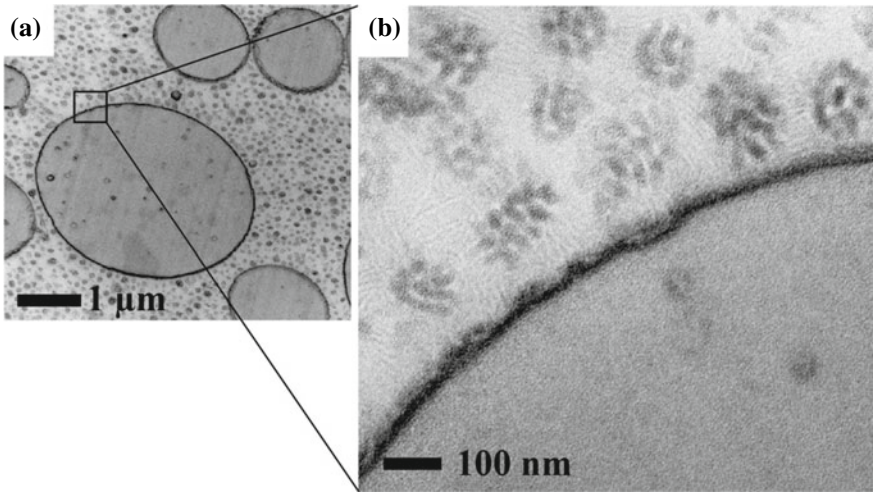

Fig. 17 TEM micrographs showing the multi-phase structure of PA6/PPO/SEBS*g*MA ternary blend stained with RuO_4. **b** Is the magnified image of **a**. The images were taken as zero-loss images by EFTEM

3.3 Focused Ion Beam Fabrication (FIB)

Focused ion beam (FIB) is one of the methods of sampling a thin specimen from specific regions of a bulk sample for TEM and STEM imaging and microanalysis [55]. Unlike SEM, FIB systems use a focused beam of ions, usually Ga ions, to mill specific regions on the surface. The FIB/SEM system combines the two methods: SEM for high-resolution electron imaging and FIB for in situ milling of specific areas while monitoring the process with SEM. FIB specimen preparation can be applied to almost any material, hard or soft, or a combination of both.

Figure 18 demonstrates the micro-sampling process, consisting of several FIB steps, for sampling a thin specimen of a polymer composite coated with a thin copper film deposited by electroless plating: (1) surface protection; (2) peripheral milling; (3) bottom cutting; (4) precise probing processes of fixing the probe, micro-bridge cutting, picking up a micro-sample; (5) fixing the micro-sample to the TEM's specimen carrier and probe cutting; and (6) final thinning to create a thin window for electrons. Before cutting, a protective tungsten (W) layer is deposited onto the region of interest using electron beam-induced deposition. The rough-milling process creates trenches and extracts a thin chunk (a sample piece) from the bulk material, which is then welded to a nanomanipulator probe. The bridge of the chunk is cut, and the chunk is picked up and transferred to a TEM grid, where the final-milling process is employed. In the final-milling process, the chunk is thinned and polished down to around 100 nm in thickness. The process involves gradually reducing the FIB voltage and applying additional polishing to eliminate damaged layers on both sides of the specimen. Specifically, the FIB voltage is reduced from its initial value of 30–5 kV when the specimen thickness reaches approximately 200 nm. Subsequently, polishing is performed at voltages ranging from 0.6 to 1 kV to remove the damaged layers on both sides of the specimen. Finally, the electron-transparent window for TEM is prepared at the center of the lamella.

Thinning complex structures comprising various materials, including highly filled composites and layered materials, into electron-transparent lamellae suitable for TEM analysis can be accomplished using FIB. Such materials can be challenging to section by ultramicrotomy, resulting in cutting artifacts at the interface between the components. Another advantage is that FIB enables micro-sampling that can select specific regions accurately for the sampling using the SEM function coupled with an FIB system, making it a useful tool for microanalysis.

However, the drawbacks to FIB sample preparation are the ion implantation into the specimen and severe material damage caused by the ion collision. Moreover, the FIB process is time-consuming as compared to ultramicrotomy. The area of the electron-transparent window fabricated by FIB is usually limited to several ten microns, while the size of ultrathin sections prepared by ultramicrotomy is several hundred microns. Polymer samples are affected by the bombardment of the high-energy ion beam, which mainly produces noticeable effects on the chemical analysis by EELS. FIB has, therefore, limited applicability to polymers because many of them are sensitive to beam damage. Carbon fiber-reinforced plastic (CFRP) is a material

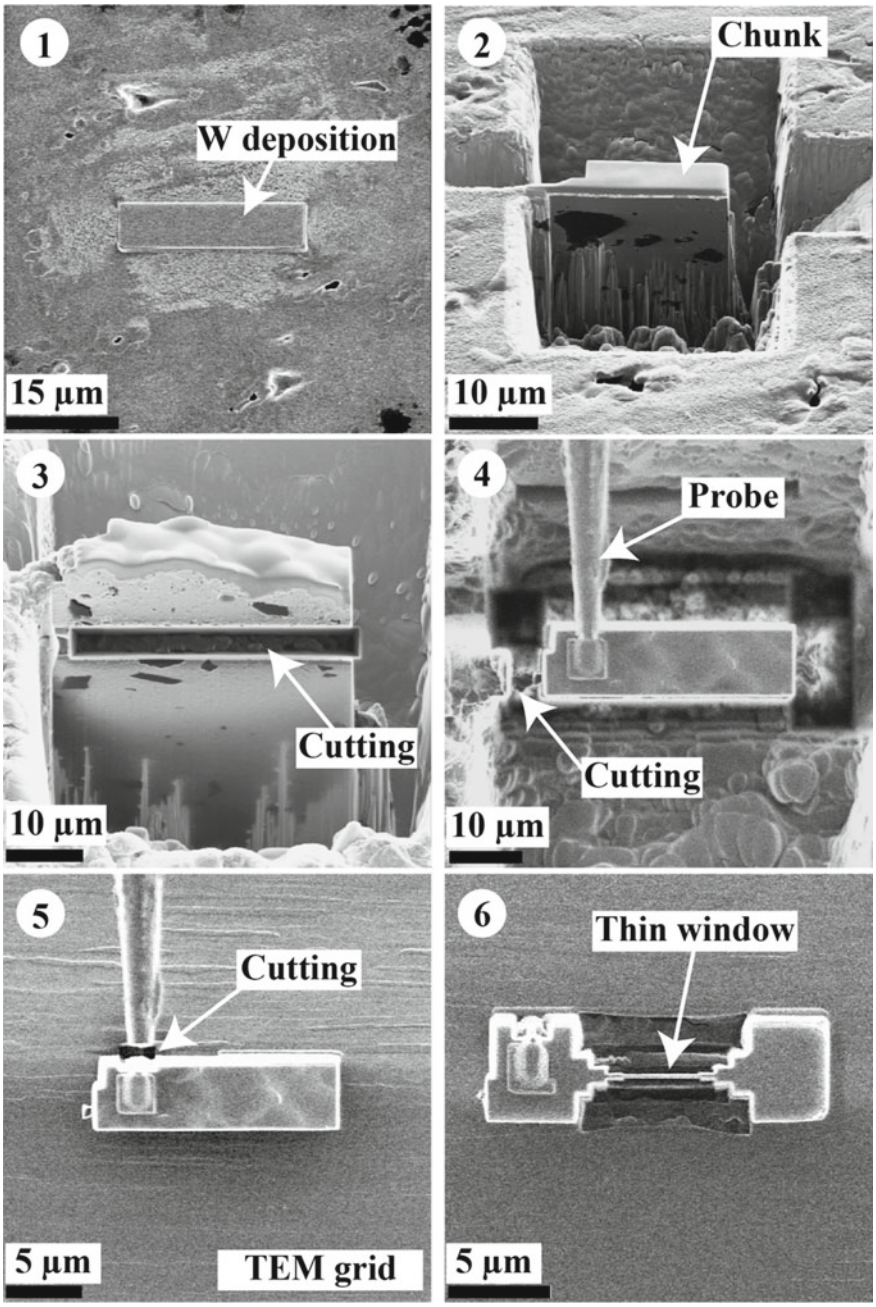

Fig. 18 SEM micrographs showing the stages of preparing a TEM specimen by FIB. 1: tungsten (W) coating; 2: rough-milling to prepare a chunk in bulk; 3: cutting off the bottom part to separate the chunk from the bulk; 4: in situ manipulator is fixed on the chunk; 5: the chunk is transferred and fixed on a TEM grid, and the FIB cuts the tip of the manipulator to release the sample; 6: the final thinning process to create a thin window for a final TEM specimen

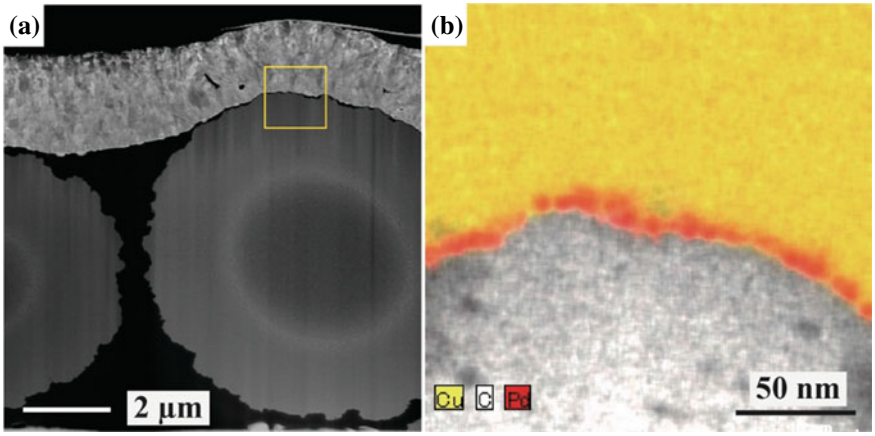

Fig. 19 Cross section of CFRP coated with electroless plated copper foil: **a** STEM-HAADF image; **b** STEM-EDX elemental map presenting Cu, C, and Pd distributions in the square area indicated in **a**

that is difficult to cut into a thin section for the TEM investigation by ultramicrotomy. At the same time, FIB allows to create a thin cross section with a smooth surface, as shown in Fig. 19. Figure 19a is an STEM-HAADF image showing the cross section of a CFRP coated with the copper film deposited by electroless plating. Cross sections of carbon fiber, matrix plastic, and copper films were successfully fabricated into a thin lamella of uniform thickness. Cross sections of carbon fiber, matrix plastic, and copper films were successfully fabricated into a thin lamella of uniform thickness. A slight gap between the electroless copper plating film and the carbon fiber can be confirmed to be filled with matrix resin. The CFRP surface is fully covered with the resin, and the copper plating film adheres to the matrix resin via the Pd nanoparticles. The STEM-EDX elemental mapping was performed, where the Pd nanoparticles act as the catalyst for the electroless plating of copper and are densely packed at the interface between the copper and CFRP.

3.4 Surface Replica

The method of replication involves the creation of a copy of a surface's topography through the use of casting or pressing techniques. This technique is commonly used when other methods of duplication are not feasible. One prevalent application of this technique is in metal replica-based electron microscopy, which allows for a high-resolution examination of the topography of biological structures. Another example of this method's use in biology is the freeze-fracture technique. A frozen biological sample is physically broken apart, and platinum–carbon is vacuum-deposited to produce a replica film that can be examined using TEM.

When investigating polymer surfaces that display structural changes after etching or fracture, SEM or atomic force microscopy (AFM) is typically used. However, the replica technique with TEM is employed when these surfaces are inaccessible using other techniques. A thin metal film evaporates onto the surface to produce a replica, and shadowing is carried out using heavy metal to enhance structure contrast. The metal is evaporated at an oblique angle to the surface, resulting in a lighter coating on the back of protrusions, creating the illusion of surface topography.

Figure 20 depicts the step-by-step process for creating surface replicas. A freeze-fracture device is used to vacuum deposit a mixture of platinum and carbon onto the sample surface (Fig. 20a). To preserve the original surface morphology during the deposition process, the specimen is fastened onto the cryo-stage at a temperature of −144 °C. A 7-nm-thick layer of Pt is sputtered from a low angle of 25°, and then a 25-nm-thick carbon layer is deposited from another source at a 90° angle to reinforce the Pt film. The thickness of these films is monitored using a quartz crystal-thickness monitor. The specimen is rotated horizontally during deposition to achieve a semi-stereoscopic effect and to spread the deposit into the surface structures' finer spaces. After deposition, the coated specimen is transferred to room temperature in an atmosphere. A 30 wt% gelatin aqueous solution is poured onto the replica surface overnight to solidify. The gelatin layer is then peeled off from the replica films and floated on a 10 wt% aqueous potassium thiocyanate (KSCN) solution. After the gelatin layer dissolves entirely, the Pt-C replica film is washed with dilute H_2SO_4 and water and transferred onto a copper grid coated with collodion. The sample's surface topography can be precisely replicated, and the films can be examined using STEM in the HAADF mode. This technique is commonly utilized in examining biological materials [57] and has also been used in studying the tribological properties of polymer surfaces [58].

An example demonstrating the replica-STEM technique's effectiveness in examining semicrystalline polymer surface structures is presented in Fig. 21. The Pt-carbon replicas are produced from various locations on the backside of a plastic bottle screw cap made of iPP through injection molding. The STEM-HAADF images display two different lamellar morphologies: one exhibits randomly oriented and curved or spiral lamellae (top image). In contrast, the other part shows linear lamellae aligned in the same direction (bottom image). Additionally, the former lamellae are slightly thicker than the latter. This variation in the crystalline lamellae's morphology concerning the site may be due to the injection molding-induced orientation and the thermal histories during solidification in the mold. This technique allows for a clear view of the original specimen's surface features or topography without being concerned about electron beam irradiation-induced damage. Furthermore, combining the replica technique with STEM tomography allows for the development of three-dimensional surface structures, facilitating high-resolution fractography studies as outlined in Sects. 4 and 5 in "Interfacial Phenomena in Adhesion and Adhesive Bonding Investigated by Electron Microscopy" chapter [59].

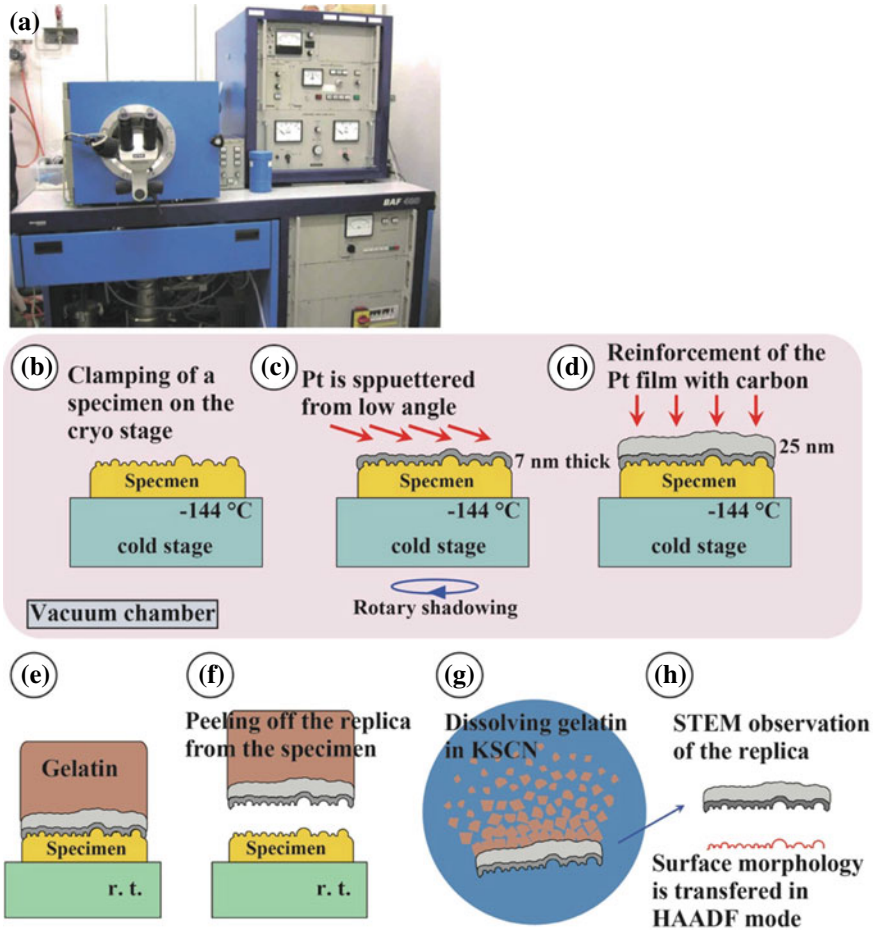

Fig. 20 Preparation procedure of replicated film of fracture or etched surfaces using a freeze-fracture apparatus: **a** appearance of a freeze replica apparatus (Balzers, BAF400D); **b** clamping of a specimen on the cryo-stage; **c** sputtering of Pt from low angle; **d** reinforcement of the Pt film with carbon; **e** drop of 30 wt% gelatin onto the replica; **f** peeling off the replica from the specimen; **g** dissolving gelatin in KSCN solution; **h** STEM-HAADF observation

4 EFTEM

4.1 Electron Spectroscopic Imaging (ESI) and Parallel EELS

Only electrons with large scattering angles contribute to contrast generation in CTEM, as they are selected for imaging solely through the objective aperture. The energy of the electrons and their energy differences are not considered, even though the chromatic aberration of the objective lens has a significant impact on contrast and

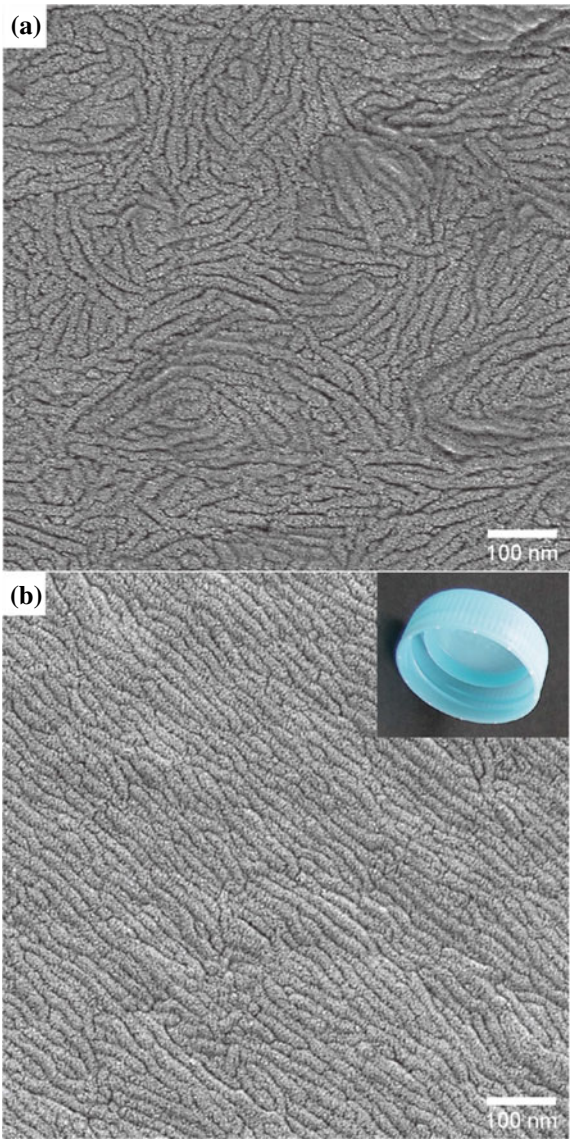

Fig. 21 STEM-HAADF images of Pt-carbon replica taken from the screw cap of a plastic bottle. **a**, **b** show location-dependence lamellar structures of the injection-molded article of *i*PP. Dr. Takayuki Uchida and Dr. Kazunori Kawasaki, AIST provide the data

resolution. As in CTEM, the image in EFTEM is produced by electron scattering in the specimen. However, EFTEM utilizes other interactions that need to be considered in CTEM. Figure 22 shows the electron beam path schematic diagram in an in-column-type EFTEM (LEO922 OMEGA, Carl Zeiss) [43]. In EFTEM, the transmitted electrons are not only selected according to their angle but also to their energy. An energy filter (Ω filter) disperses the inelastically scattered electrons according to their energy. Insertion of an energy-selecting slit in the energy-dispersive plane

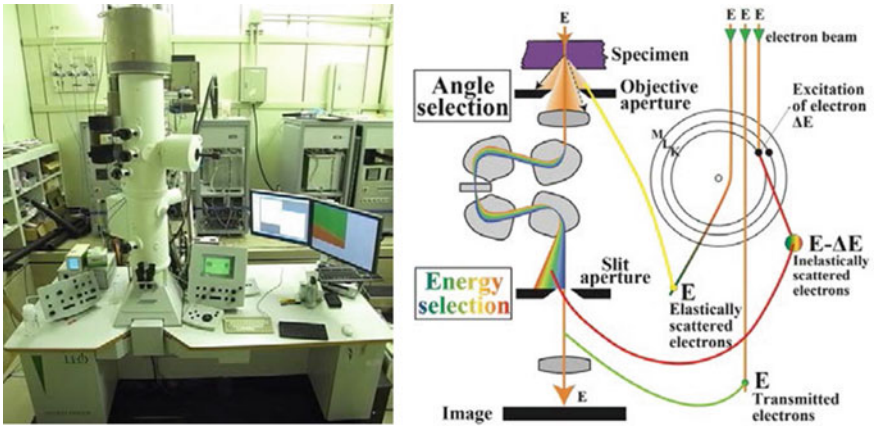

Fig. 22 Appearance of an in-column EFTEM, LEO922 OMEGA (Carl Zeiss) (*left*) and the schematic diagram of the selection of the electrons according to the scattering angles and the energy losses (*right*)

and subsequent projection of the corresponding image plane onto a screen allows energy-filtered imaging. Only electrons of a particular energy loss are transmitted, forming an energy-filtered image. This is most commonly known as electron spectroscopic imaging (ESI). Alternatively, when focusing the projector lens system on the energy-dispersive plane, an EEL spectrum can be seen on the screen, which permits EEL spectroscopy. This spectral acquisition method is named "parallel EELS" [60]. A spectrum can be obtained simultaneously in several ranges of 100 eV, which is imaged using a high-resolution CCD camera. An image analysis system measures the intensity and converts it into an energy-loss spectrum.

Dual electron selection by EFTEM results in considerably enhanced contrast. New information can be obtained with the structure-, thickness-, and element-specific contrast. In addition, ESI is capable of elemental mapping with rapid acquisition and high lateral resolution.

Figure 23 shows the three imaging modes available in EFTEM:

- **Global image**—The spectrometer disperses the electrons according to their energy (green with, red without energy loss), but the slit is not in the beam path. The second projective system combines all electrons into joint imaging. The results correspond to the quality of CTEM images, where the advantages of the filter are not utilized (left).
- **Zero-loss image**—The slit is in the beam path. High voltage is set to rated voltage, e.g., 200 kV. The slit allows only electrons without energy loss to pass. All electrons which have lost energy due to inelastic scattering are filtered out. This mode enhances the contrast for all imaging modes, such as bright field, dark field, and diffraction (center).
- **Energy loss image**—The slit is in the beam path. High voltage is increased by the required energy ΔE. The slit position and the spectrometer current remain

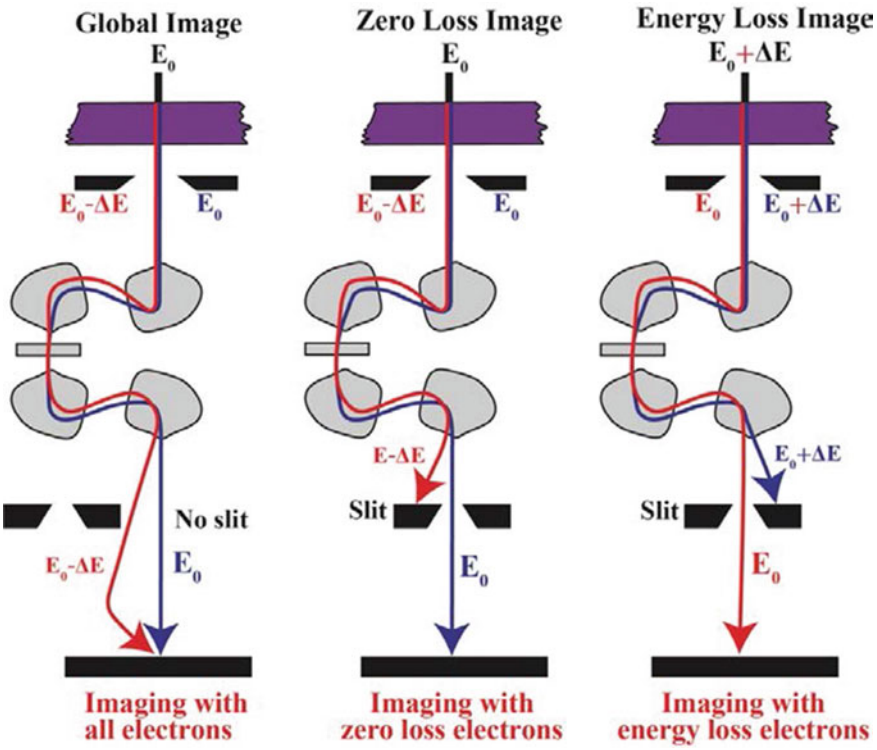

Fig. 23 Three imaging modes available in EFTEM

constant. The slit allows only electrons to pass that have lost the ΔE energy and are, therefore, back to the rated voltage. This mode is used for imaging with selective contrast on thin and thick specimens (right).

Different modes of ESI can be obtained by using energy-filtered images that are obtained by selecting electrons with a narrow energy width from different regions of an EELs spectrum. For the ESI of polymeric materials, energy windows ranging from 10 to 30 eV have commonly been used. The zero-loss imaging, as shown in Fig. 17, is a technique utilized to enhance the quality of bright-field images, although it does not provide element-specific information. The purpose of zero-loss imaging is to exclude all electrons that have been inelastically scattered, allowing only the elastically scattered and unscattered electrons that pass through the objective aperture to contribute to the image. Zero-loss imaging can improve resolution and increase contrast by minimizing chromatic aberration.

Energy loss imaging involves selecting electrons with a narrow energy width from the EEL spectrum. An energy window close to but not reaching the carbon K-edge (i.e., between approximately 150 and 280 eV) can be used to achieve structure-sensitive imaging. This window minimizes the scattering due to carbon atoms and

enhances the sensitivity and resolution of dark-field-like images, which are superior to elemental mapping. By selecting different energy-loss levels, the contrast in thicker specimens can be adjusted, and mass thickness effects such as cutting artifacts can be reduced or eliminated. The resulting contrast can be structure sensitive, phase sensitive, or element sensitive. Element-specific contrast allows for rapid visualization of element location by continuously varying the energy-loss values, causing areas containing a specific element to appear brighter in the image when the energy-loss value reaches the range where the element has its absorption edge.

4.2 Elemental Mapping and Image-EELS

In addition to element-sensitive imaging, elemental mapping representing the quantitative elemental distributions can be obtained. Elemental mapping is a very useful mode of EFTEM for identifying phases in heterogeneous materials. In conventional EDX mapping, the time required for recording an image of high-information content is very long because serial procedures are very time-consuming. With EFTEM, element distribution images are taken parallel, very fast, and with high local resolution. Elemental mapping is based on the fact that each core-loss edge of an EELS spectrum occurs at the energy characteristic of a specific element. A core-loss edge is superimposed on a strong decay as a background (BG) due to the plural scattering and extracting elemental information for mapping necessitates their separation from the BG contribution. Element-specific images (core-loss images) contain not only elemental information but also background information. They are, therefore, not taken directly but in several stages. First, an element-specific image is taken, then the background image below the ionization edges is calculated. Next, the background is subtracted from the element-specific image to obtain an element distribution image. As shown in Fig. 24a, several algorithms are available for background computation [61].

The two-window and three-window methods are employed for the calculation of the BG. In the two-window method, a single pre-edge image (at the energy loss of E_2) is scaled and then subtracted from the corresponding post-edge image (at the energy loss of $E_{\max}$) as expressed by Eq. (1) for an element of interest until there is zero net intensity in areas where that element is known to be absent.

$$\mathrm{S}(E) = \mathrm{S}(E_{\mathrm{MAX}}) - c \cdot \mathrm{S}(E_2) \quad c < 1 \tag{1}$$

In the three-window method, the BG curve is estimated using the two-energy windows (E_1 and E_2) assuming power law (2) or exponential law (3) dependences as follows, where the factors A and r are calculated pixel by pixel from the signals $\mathrm{S}(E_1)$ and $\mathrm{S}(E_2)$.

$$\mathrm{S}(E) = A \cdot E^{-r} \tag{2}$$

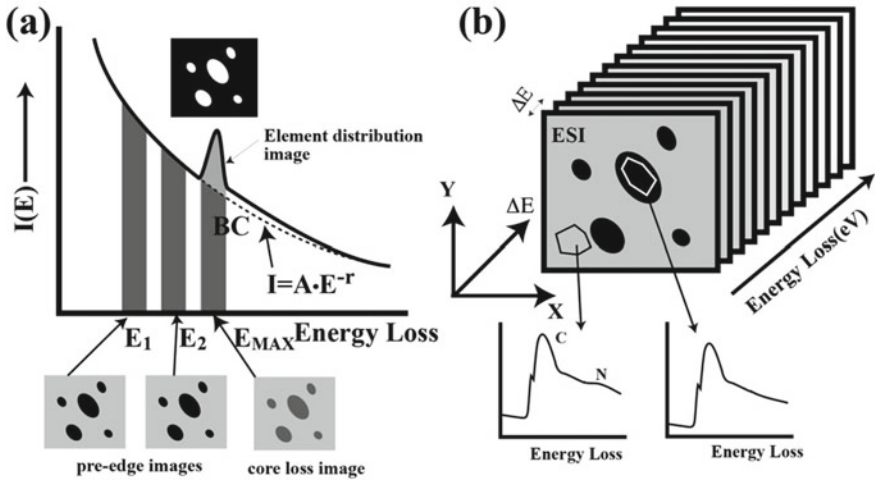

Fig. 24 Schematic illustration of the analytical modes available in EFTEM: **a** Elemental mapping; **b** Image-EELS

$$S(E) = A \cdot \exp(-r \cdot E) \tag{3}$$

A jump ratio image is generated by acquiring one pre-edge image and one post-edge image, which is then used to compute the ratio of the two. This produces a qualitative elemental distribution image related to the mass thickness of the element present. Jump ratio mapping is beneficial when there is a small amount of a substance in a relatively homogeneous matrix, and it reduces diffraction contrast created by metallic materials [62].

Image-EELS allows us to obtain EELS spectra from small and irregularly shaped objects chosen arbitrarily in an image [63–67]. As illustrated in Fig. 24b, tens of energy-loss images are captured sequentially over a broad range of energy loss to create a three-dimensional dataset containing spatial information ($I(x,y)$), obtained simultaneously, and spectral information ($I(E)$), obtained serially. EELS spectra from arbitrarily selected regions in an image can be synthesized by calculating the average gray values of the same pixels in each energy-loss image across the entire acquired image series. The image analysis system extracts the intensities at the same pixels in each image throughout the series. It constructs an EEL spectrum by plotting the intensities against the corresponding energy-loss values. To correct specimen drift, the individual images must be shifted pixel by pixel across the acquired image. A spectrum can be produced by summing neighboring pixels to improve the signal-to-noise ratio. This method is particularly suitable for analyzing minimal element concentrations on structures of any shape, and it can produce element distribution images from the image stack.

4.2.1 Elemental Mapping of Block Copolymer Nanodomain Structures

The successful application of the elemental mapping and the structure-sensitive imaging of a polymer sample is shown in Fig. 25. The specimen is an unstained thin cross section of an embedded film of a semi-rod–coil diblock copolymer of styrene (PS) and an isoprene with oligothiophene-modified side chains (POTI), namely, PS_{400}-*b*-$POTI_{25}$ (the subscripts indicate the number of repeating monomer units) as shown in Fig. 25a [68]. The experiments were carried out in an LEO 922 EFTEM with an integrated Ω-filter at an acceleration voltage of 200 kV. Figure 25b is an EELS spectrum taken by the parallel EELS, exhibiting the sulfur L_{23}-edge (S L_{23}-edge) at 160 eV energy losses after the BG subtraction. Although the as-taken spectrum seems to be a monotonical slope, the BG fitting using the energy range before the edge reveals the existence of the core-loss contribution. After subtracting the BG contribution, the core-loss peak of the S $L_{2,3}$-ionization edge can be seen, even though it is a noisy spectrum. The upper two images in Fig. 25c are the pre-edge and the post-edge (core-loss) images taken at the energy losses of 150 ± 10 and 200 ± 10 eV, respectively. The core-loss image clearly shows the well-ordered domains in the film, and thus it corresponds to the element-sensitive image of the sample. The elemental distribution images were then created by the BG subtraction in accordance with the two methods: the bottom left is created by the two-window method, while the bottom right is by the three-window method.

The map generated using the two-window method produces a clearer image with a higher signal-to-noise ratio (SNR) than the one generated using the three-window method. Inelastic scattering has a low cross section and is typically 10^2 to 10^6 times weaker than elastic scattering, resulting in inelastically scattered images with higher statistical fluctuations than elastically scattered images. Therefore, the three-window method is more susceptible to statistical errors associated with background extrapolation as two images are used for fitting. However, the map generated using the two-window method still displays some small objects in the film, indicated by arrows, which are removed from the map generated using the three-window method. This suggests the presence of some particles in the film. The contrast of these particles remains unchanged when the energy-loss position shifts from the pre-edge position to the post-edge position, suggesting that they may be inorganic contaminations. The inaccuracy in the map generated using the two-window method can be attributed to the polymer and the inorganic particles giving background curves with different slopes. The two-window method does not consider changes in background shape from one region of the specimen to another. Therefore, the two-window method cannot provide accurate elemental maps if the image involves components with different background features. On the other hand, the three-window method calculates the background curves pixel by pixel, enabling accurate subtraction of background intensities from the core-loss image for all pixels. This demonstration highlights the background subtraction process's influence on elemental mapping results. The three-window method should be used for performing quantitative elemental mapping.

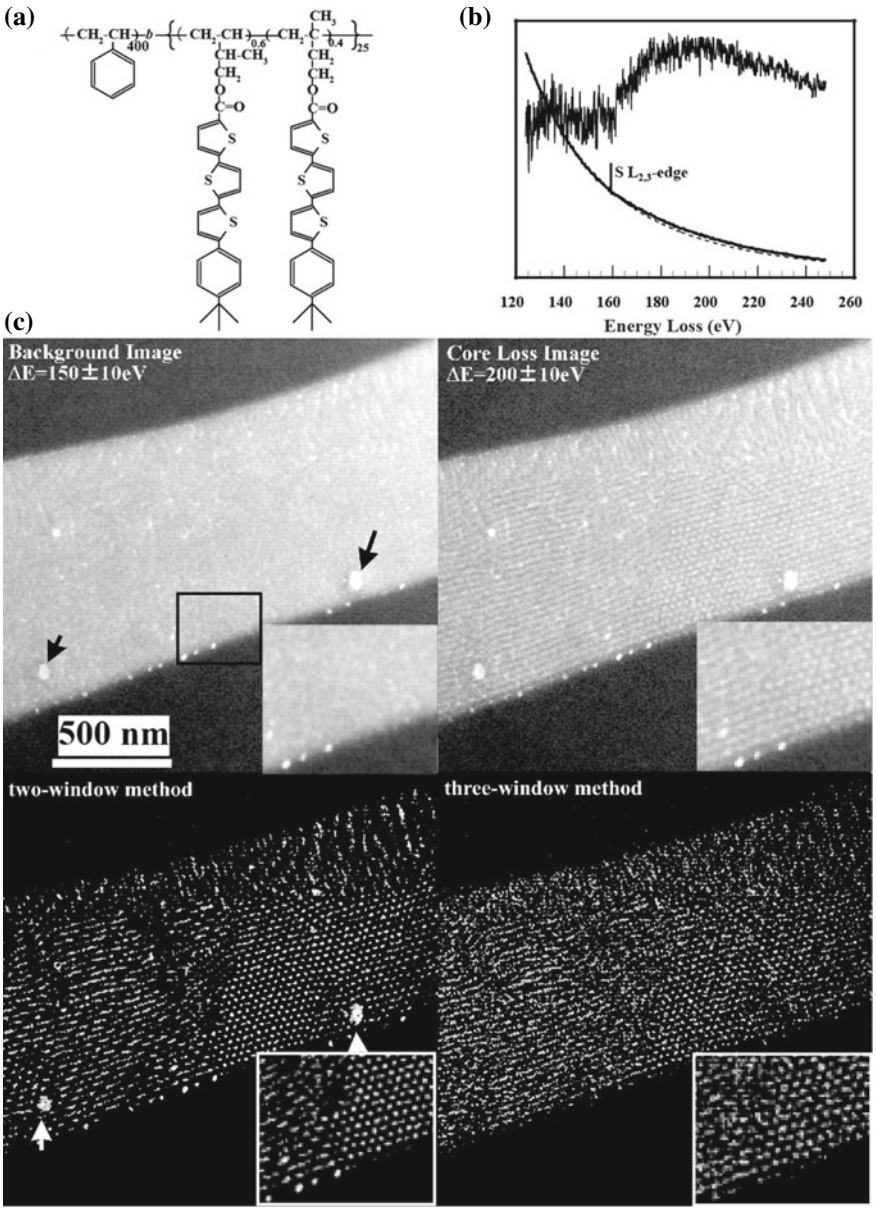

Fig. 25 Characterization of the phase-separated morphology of a diblock copolymer by elemental mapping: **a** chemical structure of a semi-rod–coil diblock copolymer of PS and an isoprene with oligothiophene-modified side chains (POTI); **b** parallel EELS spectrum in the energy-loss region involving the sulfur $L_{2,3}$-ionization and the core-loss edge appeared after the BG subtraction; **c** pre-edge and post-edge images of the cross section of the diblock copolymer film, and the sulfur distribution images calculated by the two-window and the three-window methods

4.2.2 Analysis of Rubber/Filler Interfaces by Image-EELS

Image-EELS was employed in the following study to investigate the interfaces between an inorganic filler and rubber in vulcanized rubber materials. Vulcanization, a crucial industrial process for cross-linking rubber molecules, involves accelerators and activators such as ZnO combined with stearic acid to accelerate the vulcanization reaction and enhance rubber properties. EFTEM was employed to examine the interactions between the rubber matrix and ZnO filler particles added as an activator in the accelerated vulcanization process [69]. The interactions between the rubber matrix and ZnO filler particles in the accelerated vulcanization process were investigated by EFTEM [70, 71].

Thin sections of the vulcanized styrene-butadiene-rubber (SBR) with 100 nm thickness were prepared by cryo-ultramicrotome at −60 °C after the vulcanization at 170 °C for 10 min. Figure 26 presents the typical ZnO particles found in the vulcanized SBR. The upper row shows the zero-loss images, while the bottom row shows the corresponding structure-sensitive images at 250 ± 10 eV, revealing the presence of a phase surrounding the ZnO particles. The Image-EELS was used to characterize the product around the ZnO particles. The energy width and the energy increment for sulfur and oxygen were set at 5 and 3 eV, respectively. The energy width and increment of zinc were set at 10 and 5 eV, respectively. The Image-EELS enables the acquisition of EELS spectra from regions of interest in any shape in an image [70–72].

Figure 27a through d displays the energy-filtered image at 250 ± 10 eV and the corresponding elemental distribution images of S, Zn, and O, respectively. The corresponding Image-EELS spectra obtained from the regions indicated in Fig. 27a are shown in the bottom row. The elemental mapping indicates that the phase formed around the ZnO particle contains S and Zn but not O. EELS spectra, including the core-loss edges of each element, are extracted from the region indicated in Fig. 27a, as shown below the corresponding images. The corresponding Image-EELS spectra allow semi-quantitative elemental analysis in the maps. The S $L_{2,3}$-edges suggest that sulfur is distributed around the ZnO particles (regions 2 and 3) and the SBR matrix (region 4). The Zn $L_{2,3}$-edges indicate that Zn is localized in the limited area around the ZnO particle and is not detected in the rubber matrix. Oxygen is distributed almost evenly in the SBR matrix, which may be attributed to stearic acid.

Therefore, the S- and Zn-rich phases around zinc oxide particles are not due to the fine dispersion of ZnO itself but are by-products formed due to the accelerated vulcanization reaction. In the complex accelerated vulcanization reaction mechanism, Zn^{2+} ions generated from zinc oxide by the addition of stearic acid are known to increase the efficiency of the cross-linking reaction of rubber through coordination with vulcanization accelerators. As a result, ZnS is produced as a by-product, and the EFTEM analysis clarifies its existence. The fact that ZnS is present surrounding the ZnO particles during accelerated vulcanization suggests that the reaction proceeds in the vicinity of the ZnO particles and that the crosslink density of the rubber is relatively higher around the ZnO particles. This result indirectly suggests the heterogeneity of the rubber network structures.

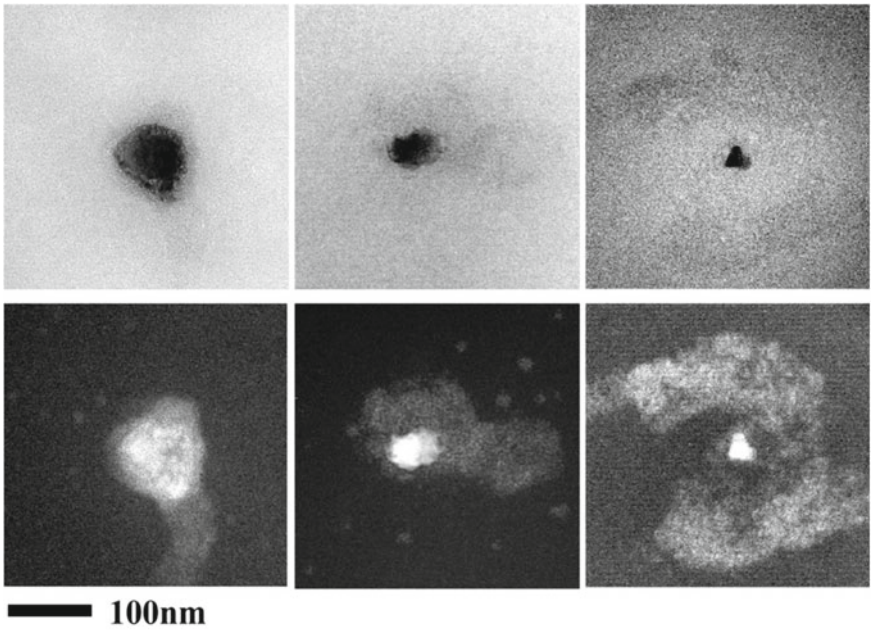

Fig. 26 Typical ZnO particles distribute in the SBR matrix after the vulcanization. The upper row shows the zero-loss images and the bottom row shows the corresponding structure-sensitive images at 250 ± 10 eV. Reprinted with permission from Ref. [70]. Copyright 2006, American Chemical Society. All Rights Reserved

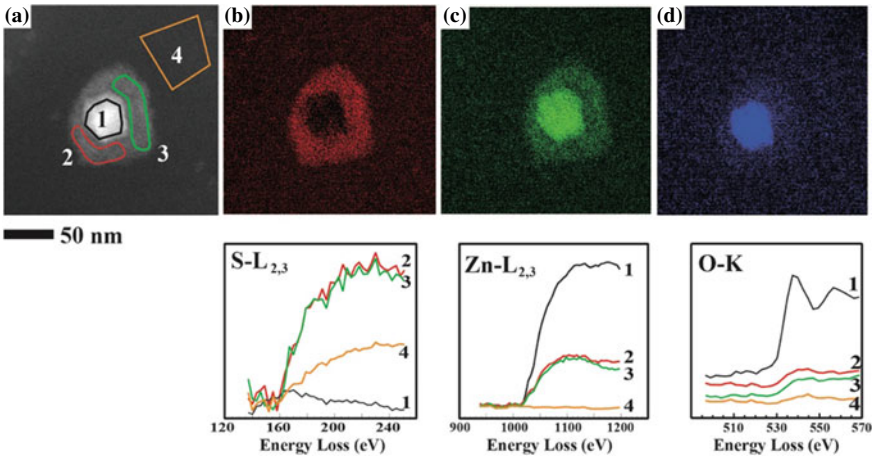

Fig. 27 Elemental maps and Image-EELS spectra obtained from the interface between a ZnO particle and SBR matrix: **a** Structure-sensitive image at 250 ± 10 eV; **b–d** Elemental distribution images of S, Zn, and O. The regions indicated in **a** are subjected to the Image-EELS analysis and the core-loss edges after the BG subtraction are shown below the corresponding images. Reprinted with permission from Ref. [70]. Copyright 2006, American Chemical Society. All Rights Reserved

4.2.3 Image-EELS Analysis of Reaction-Induced Phase Decomposition in Thermoset/Thermoplastic Polymer Blends

One of the processes involved in developing morphology in multi-component polymer systems is known as reaction-induced phase decomposition. During the polymerization of a monomer, a blend of a polymer and a monomer undergoes phase separation with an increase in molecular weight [73–83]. Utilizing a thermoset resin as a "reactive solvent" can be more environmentally friendly and efficient than common organic solvents since solvent removal is not required [84, 85]. As the curing reaction progresses, phase decomposition occurs in thermoset and thermoplastic (or rubber) blends, leading to unique multi-phase structures that can be used in high-performance composites and adhesives.

In this study, the samples analyzed are blends of poly(2,6-dimethyl-1,4-phenylene ether) (PPE) and 1,2-bis(vinyl phenyl)ethane (BVPE). PPE is a material that is attractive in the electronics industry due to its low dielectric constant (2.45), low dissipation factor (0.0007), and high glass transition temperature (T_g) of 210 °C. BVPE, on the other hand, is a styrene-type crosslinker with good thermal durability and dielectric properties and can be cured at relatively low temperatures without a curing agent [86]. The morphology development of PPE/BVPE blends through BVPE crosslinking was analyzed using Image-EELS [87]. The chemical structures of BVPE and PPE are similar, but only PPE contains oxygen, as shown in Fig. 28. The influences of composition and curing time on phase decomposition behavior were investigated by examining the intensity ratios of the O K-edges extracted from the two phases. Blending these two components is expected to yield materials with excellent dielectric properties, overcoming the drawbacks of the individual components. That is, the brittle nature of the cured product of BVPE could be improved by blending it with PPE, while the poor processability of PPE due to its high viscosity could be solved. In addition, the effect of the reaction between the two components on phase decomposition behavior was investigated by introducing a reactive allyl unit onto PPE. The blends had compositions of 25/75, 50/50, and 75/25 (PPE/BVPE) by weight, denoted as N25, N50, and N75 for the blends with non-reactive PPE and as R25, R50, and R75 for the blends with reactive allyl-PPE.

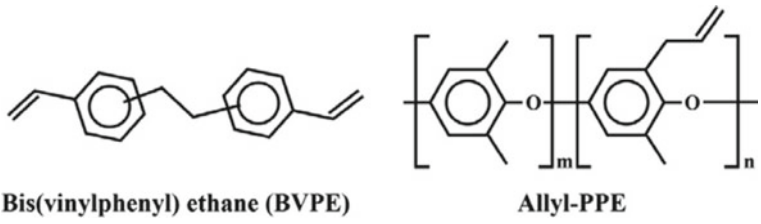

Fig. 28 Chemical structures of bis(vinyl phenyl) ethane (BVPE) and poly(2-allyl-6-methylphenol-*co*-2,6-dimethylphenol), (allyl-PPE). Reprinted with permission from Ref. [87]. Copyright 2007, Elsevier. All Rights Reserved

To prepare the samples for observation, ultramicrotomy was used to create thin sections with a thickness of approximately 60 nm at room temperature. Gold nanoparticles with 10 nm in diameter were then dropped onto the specimens to serve as markers for focus adjustment and drift correction during observation. High-resolution elemental mapping and quantitative EELS analysis were performed using Image-EELS. The energy-loss range was set to 450–600 eV, with a 5 eV energy width for each image and a 3 eV energy increment between neighboring images. Oxygen elemental maps were created by the "two-window jump ratio" method, which involved selecting two recorded images from those acquired by Image-EELS and dividing the energy-filtered image beyond the oxygen ionization edge at approximately 535 eV (post-edge image) by the energy-filtered image below the ionization edge (pre-edge image).

Figure 29a–d depicts the zero-loss image, the pre-edge image at 525 ± 2.5 eV, the post-edge image at 550 ± 2.5 eV, and the calculated oxygen elemental map, respectively, of N50 (a blend of PPE/BVPE with a weight ratio of 50/50) that was cured for 60 min. The oxygen elemental map reveals the phase-separated morphology due to the difference in the oxygen concentrations between the two phases, characterized as oxygen-rich (PPE-rich) and oxygen-poor (BVPE-rich) phases. Although the pre- and post-edge images exhibit no differences in the image contrast (Fig. 29b, c), the calculated oxygen elemental map presents the phase-separated morphology, which can identify the slight differences in the compositions between the two phases.

In Fig. 30, the phase decomposition of blends during curing is studied. The changes in oxygen distribution images are analyzed as the curing time increased for N25 (which is a BVPE-rich blend shown in Fig. 30a), N50 (shown in Fig. 30b), and R25 (shown in Fig. 30c), where R25 contained 10 mol% of the reactive unit in allyl-PPE. The samples were annealed at 230 °C for specific periods and then dipped into liquid nitrogen to freeze the developed phase-separated morphologies. All observations were conducted at room temperature. The oxygen maps for N25 show that oxygen-poor domains (BVPE-rich phase) are formed in the PPE-rich matrix during the early stages of curing and are coarsened as the curing time increases. However, the domain sizes of N50 remain unchanged during the curing process and are smaller than those in the BVPE-rich blend (N25). The growth of BVPE-rich domains during the curing of

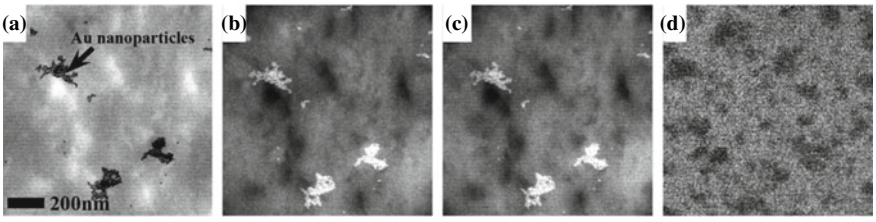

Fig. 29 A series of images of N50 showing zero-loss image (**a**), O K pre-edge image (**b**), O K core-loss image (**c**), and oxygen map (**d**) calculated by "two-window jump ratio" method in the same specimen region. Reprinted with permission from Ref. [87]. Copyright 2007, Elsevier. All Rights Reserved

R25 appears to be restrained compared to N25, suggesting that the reaction between the two components suppresses the phase decomposition.

To quantitatively estimate the differences in oxygen concentrations between the two phases, a method illustrated in Fig. 31 was employed. Firstly, the borders between the two phases in the oxygen map were identified precisely, as shown in Fig. 31a. Subsequently, the O K-edges were extracted from the two regions, as shown in Fig. 31b. Next, the background contributions were removed from the spectra using the power law function, and the oxygen core-loss peaks were obtained, as demonstrated in Fig. 31c. Finally, the integrated ratios of the two core-loss peaks, with an energy width of 60 eV, were calculated to determine the relative oxygen atomic ratios of the two phases.

The phase decomposition of the blends is characterized using two parameters: oxygen elemental ratios and the area fractions of the two phases. Figure 31d displays the plot of the oxygen atomic ratio as a function of curing time. The N25 blend exhibits

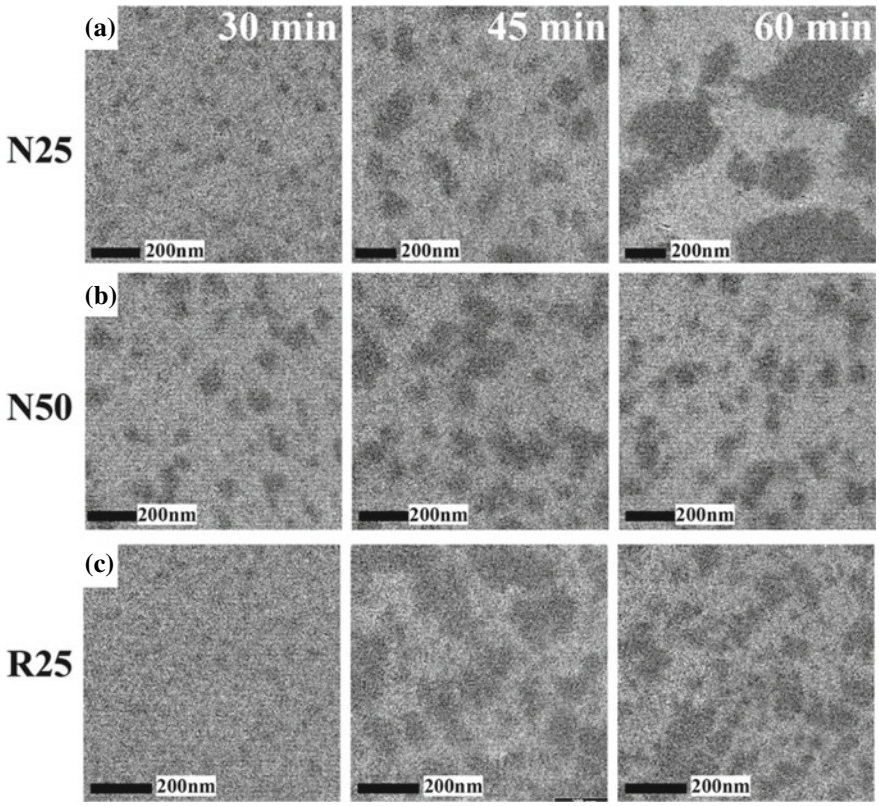

Fig. 30 Phase decomposition development of BVPE/Allyl-PPE blends: **a** oxygen distribution images of N25; **b** N50; **c** R25. Curing times are 30, 45, and 60 min for left, middle, and right columns, respectively. Reprinted with permission from Ref. [87]. Copyright 2007, Elsevier. All Rights Reserved

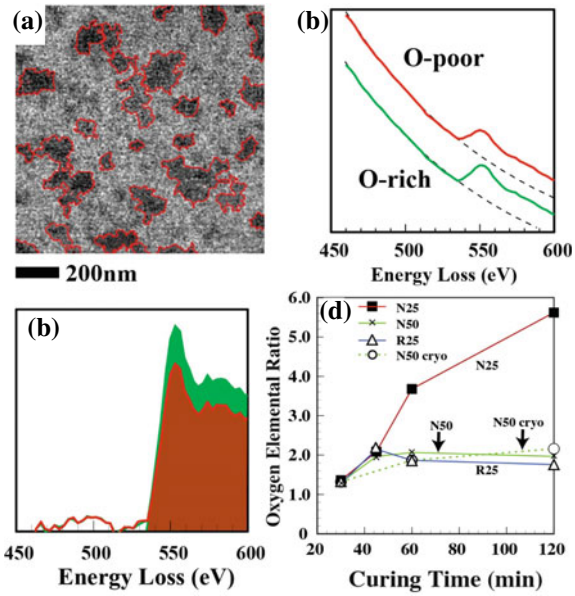

Fig. 31 Scheme for quantitative EELS analysis of the phase decomposition of PPE/BVPE blends: **a** an oxygen map classified accurately into the oxygen-rich and oxygen-poor regions; **b** EELS spectra extracted from the two regions (green and red spectra are acquired from the oxygen-rich and the oxygen-poor phases, respectively); **c** the integrated areas under the oxygen core-loss peaks calculated after the background subtraction; **d** oxygen elemental ratios between the two phases (ratio of PPE-rich phase to BVPE-rich phase) plotted against the curing time. Reprinted with permission from Ref. [87]. Copyright 2007, Elsevier. All Rights Reserved

a considerable increase in the oxygen atomic ratios between the two phases with increased curing time, while the other blends showed only a slight increase. The ratios of the compositions of the two phases are maintained at similar levels, approximately 2, except for N25, which suggests that the phase separation mechanism of N25 differs from those of the other blends.

The impact of radiation damage on the specimens during the Image-EELS data acquisition must be considered to ensure the results' reliability. It is inevitable to avoid damage to polymer specimens by the electron beam, which causes chain scission and mass loss. Therefore, observation under cryogenic conditions is recommended to minimize radiation damage. The results obtained under a cryogenic condition at − 160 °C for N50 are also plotted in Fig. 31d, demonstrating that no significant differences were observed between the two observation conditions. Hence, even though the electron beam irradiation during TEM observation may change the chemical structures of the polymers, the elemental compositions may not be altered significantly. This allows us to perform quantitative EELS analysis of the phase decomposition processes at room temperature.

5 STEM

5.1 Spectrum Imaging (SI) with Simultaneous EELS and EDX

In STEM, the electron beam is focused into a spot with a spot size of less than 1 nm, and by rastering the beam across the sample, STEM can be used for techniques such as Z-contrast annular dark-field imaging, EDX and EELS [88]. The ray path in STEM is identical to that in TEM if the direction of the beam path in STEM is reversed. Despite this reciprocity principle, there are crucial differences between the image formation in both microscopes. In contrast to TEM, STEM does not need post-specimen lenses to magnify the image, as the transmitted electrons only need to be collected by a detector. Therefore, the image quality in STEM is unaffected by the chromatic aberration as it is in TEM. EELS and EDX, coupled with STEM, are powerful techniques that allow us to perform local elemental and chemical analysis in materials [48, 89–91]. Simultaneous acquisition of imaging and spectroscopy signals enables direct correlation between images and spectroscopic data. In EELS, an electron spectrometer attached at the bottom part of the column, as shown in Fig. 2b, measures the energy loss of the electrons in the beam through the interaction with the electrons in a specimen. STEM-EDX has been frequently employed for a quick overview of present elements. At the same time, EELS can be used for chemical analysis of elements of interest because the energy resolution in EELS is sufficient to allow the fine structure of ionization edges to be discussed. Especially, ELNES in EELS can offer chemical bonding information [89, 92]. It is expected to be a powerful approach to detecting chemical interaction at interfaces. EFTEM enables EELS to be performed in TEM mode, which involves irradiating a wide specimen area with the electron beam. In TEM mode, the energy density of the electron probe is significantly lower than in STEM mode, resulting in reduced radiation damage to the specimen. However, the spatial resolution of EELS analysis is restricted.

EDX and EELS can be worked together with the electron probe scanned pixel by pixel in the STEM mode. Spectral Imaging (SI) mode allows EDX/EELS simultaneous spectral acquisition with the annular dark-field imaging, significantly improving data-collection efficiency. Figure 32 shows an STEM instrument and the schematic illustration of the SI mode. Spectra are acquired in a spatially serial manner: EDX and EEL spectra are recorded for each position at the same time with a small probe scanned over two-dimensional (2D) regions in a specimen. Then, we can obtain a three-dimensional (3D) data cube consisting of 2D spatial position coordinates (x and y) and energy loss (ΔE) of the probe [49]. The Dual EELS system acquires the spectra, which allows recording both the low-loss and core-loss spectra nearly simultaneously at the same position before moving on to the next [93–95]. The low-loss region is captured in microseconds with a short dwell time to address the significant signal intensity disparity in the two energy-loss regions. In contrast, the core-loss regions are recorded in several seconds without modifying the beam conditions. Correcting the zero-loss peak's (ZLP) drift enables accurate energy-loss position

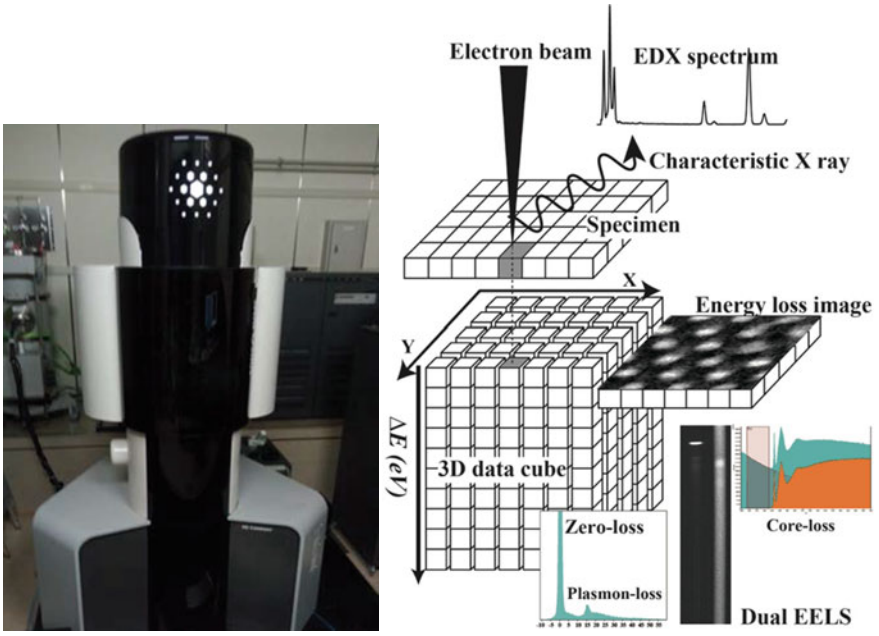

Fig. 32 An STEM instrument (TECNAI Osiris, FEI) used in this work and a schematic illustration of spectrum imaging (SI) data acquisition and processing scheme with dual EELS system

correction of the core-loss spectra. Fourier logarithmic deconvolution, employing the low-loss spectra shapes, can eliminate the influence of plural scattering in the core-loss region.

The 3D data cube can also be constructed by the TEM mode using the Image-EELS technique in EFTEM, but its scheme is different. In STEM-SI mode, the data cube is generated column by column, and the electron probe is scanned in a rectangular pixel array over the specimen. At the same time, the spectrum is collected in parallel. In EFTEM-Image-EELS mode, on the other hand, energy-loss images are collected successively in parallel across a wide range of energy loss with defined energy intervals. Those images are stacked in the data cube as depicted in Fig. 24b. Each approach has advantages and disadvantages: SI in STEM gives the highest spatial resolution and sensitivity. However, the image size is limited by the need to read the spectrum at each pixel. Image-EELS in the EFTEM provides a larger number of image pixels. Still, the spectral information is limited because the energy resolution of EEL spectra depends on the energy step in acquiring a series of energy-loss images.

5.1.1 STEM-EELS/EDX Simultaneous Analysis of Surface Oxide Layer of Aluminum Alloy

STEM measurements were conducted on a TECNAI Osiris microscope (FEI Company) equipped with an EELS spectrometer (Enfinium SE model 976, Gatan Inc.) and four windowless silicon-drift EDX detectors (FEI Super X). The measurements were performed at an accelerating voltage of 200 kV. To enhance the EDX detection efficiency and quickly detect low-Z elements in polymer materials, the four quadrant EDX detectors were symmetrically mounted above the specimen area along the optical axis [93, 95].

Figure 33 exemplifies how the STEM-SI mode provides elemental and chemical information with high spatial resolution. An oblique section of the surface of an Al6061 plate was obtained by ultramicrotomy and subjected to STEM analysis in SI mode. Three spectral information can be obtained: EELS low-loss, EELS core-loss, and EDX spectra. (a) The EELS low-loss spectrum contains a zero-loss peak at 0 eV energy loss and a plasmon-loss peak in 10–30 eV. Metallic Al gives a characteristic sharp peak at 16 eV [96]. The distribution of metallic Al can be created using the energy window at 16 ± 1 eV after the BG subtraction, as indicated by the red curve. (b) The EELS high-loss spectrum includes the O K-edge at 535 eV. An oxygen elemental map can be created using the 537–543 eV energy window and the BG subtraction as indicated by the red curve. The effects of plural scattering in the core-loss region are removed by Fourier logarithmic deconvolution using the shapes of the low-loss spectra and shown as a deconvoluted spectrum. A narrower energy window and choosing the energy-loss position permit a chemical map that can distinguish oxygen-containing Al compounds, as stated in Sect. 6 of "Interfacial Phenomena in Adhesion and Adhesive Bonding Investigated by Electron Microscopy" chapter. (c) According to the EDX spectrometry data, the aluminum surface region contains a small quantity of Mg, Si, P, and Cr, part of the aluminum alloy. The data also showed a minor amount of carbon, believed to be from atmospheric contamination during sample transportation in ambient air. Elemental maps created using EDX spectrometry reveal the Si, P, and Cr localization in the Al surface region, whereas Mg is localized in the metallic portion.

5.1.2 Mechanism of the Reactive Compatibilization of a Polymer Blend Investigated by STEM-EELS/EDX Analysis

Multi-component polymer systems can benefit from adding a small amount of a compatibilizer, which can interact with the polymer components physically or chemically to improve the strength of interfaces and the dispersion of phases [97, 98]. However, the challenge lies in locating the compatibilizer in the blends owing to its low concentration, typically less than a few weight percent. To address this issue, STEM-EDX/EELS analysis is demonstrated to evaluate the localization of the compatibilizer at the interfaces in immiscible polymer blends. As depicted in the top column in Fig. 34, this study uses a polyhedral oligomeric silsesquioxane

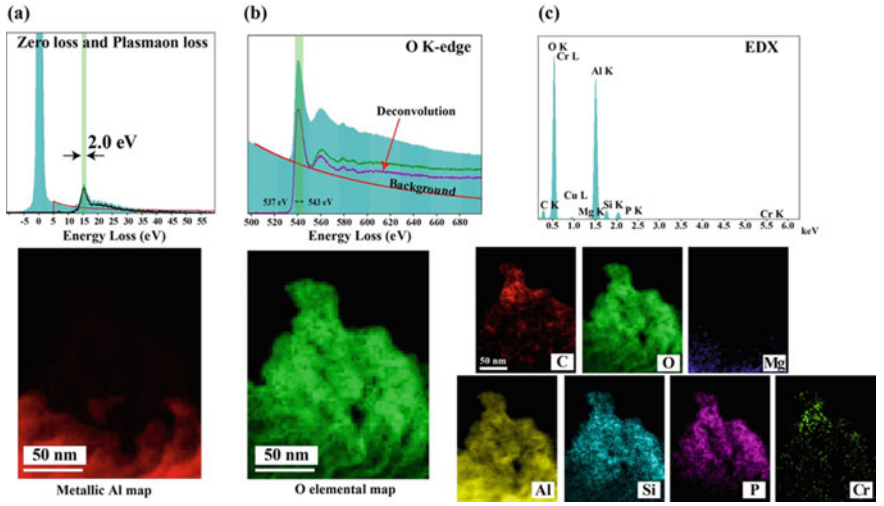

Fig. 33 STEM-EDX/EELS simultaneous analysis of the surface region of an Al6062 plate: **a** EELS low-loss region and metallic Al map; **b** EELS O K-edge and Al oxide map; **c** EDX spectrum and elemental maps. Reprinted with permission from Ref. [48]. Copyright 2022, Elsevier. All Rights Reserved

(POSS)-based compound as a compatibilizer in a PLLA/PVDF blend. The POSS molecule consists of eight silicon atoms, five connected to the epoxy groups. In contrast, the remaining three are connected to the PMMA chains, where the epoxide groups in the POSS derivatives react with the carboxyl end groups of PLLA. At the same time, the grafted PMMA unit is expected to be localized in the PVDF phase due to the thermodynamical miscibility of PMMA and PVDF as depicted in the middle column in Fig. 34 [99]. Therefore, the compatibilizer used in this study is labeled POSS(epoxy)$_5$-*g*-PMMA$_3$. The well-compatibilized PLLA/PVDF blends show a remarkable enhancement in elongation at break without decreasing the tensile modulus and strength [100]. Two-step mixing is used to obtain optimized properties (bottom in Fig. 34), where the POSS-compatibilizer is mixed with PLLA in the first step. Then the pre-mixed PLLA/compatibilizer is blended with PVDF, indicating that the location of the compatibilizer is significantly affected by the mixing sequence. STEM-EELS/EDX analysis is suitable for the PLLA/PVDF/POSS-compatibilizer multi-component polymer system because each component contains key elements for identifying their locations. That is, fluorine is for PVDF, oxygen is for PLLA, and silicon is for POSS. Also, oxygen is involved in the different chemical bonds in the polymers and the compatibilizer. In this study, the localization behaviors of the POSS-compatibilizers at the PLLA/PVDF interfaces, which are believed to be influenced by melt-blend conditions, are characterized by STEM-EELS/EDX analysis.

Figure 35 shows the STEM-BF images of the phase-separated morphologies of the PLLA/PVDF (50/50) blends. The blend films were firstly embedded in a light curable resin, LCR-D800 (Toagosei Corp.), and were cut by ultramicrotomy

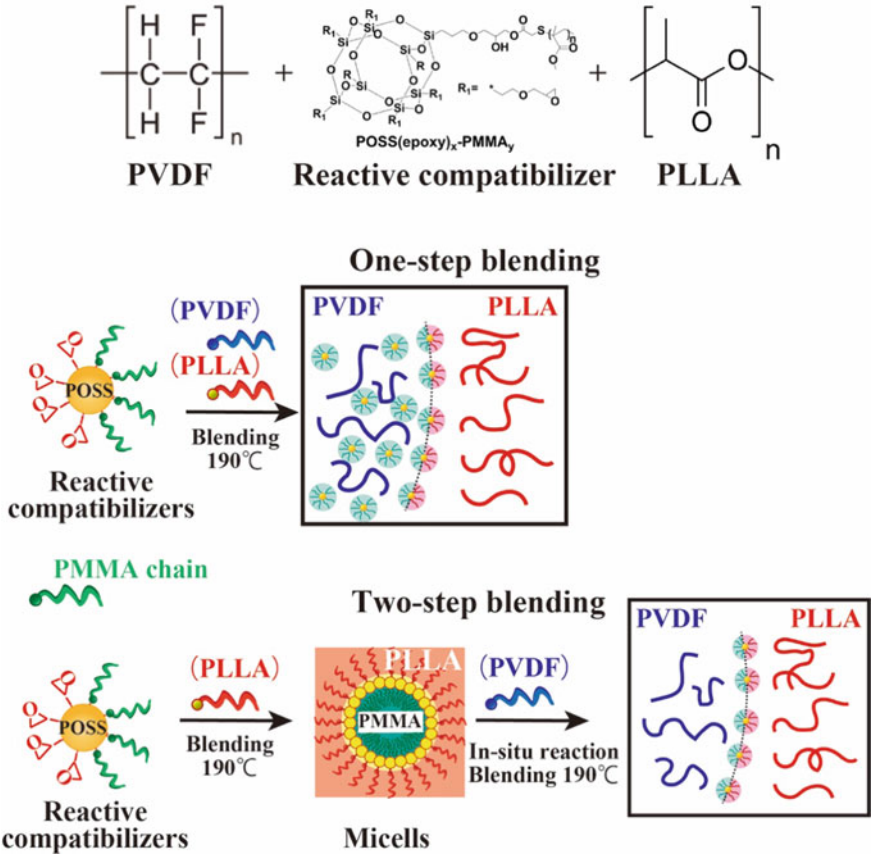

Fig. 34 Chemical structures of PVDF, POSS-compatibilizer, and PLLA (*top column*). One-step (*middle column*) and two-step (*bottom column*) blend sequences for PVDF/PLLA blends compatibilized with the POSS-compatibilizer

to obtain sections with a thickness of about 50 nm. The sections were collected on copper meshes covered with lacy carbon. The uncompatibilized PLLA/PVDF binary blend (Fig. 35a) shows the poor dispersion of the PVDF domains. In contrast, the blends with POSS(epoxy)$_5$-*g*-PMMA$_3$ prepared by one step (Fig. 35b) and two step (Fig. 35c) show remarkable improvements in the dispersion of the PVDF domains. The dispersity of the PVDF domains was quantitatively evaluated by the digital image analysis, which revealed that the average diameters and the standard deviations of the dispersed domains in one-step and two-step blends were 3.0 ± 0.13 and 2.2 ± 0.05 μm, respectively. The average diameters of those two blends are not significantly different, but the two-step blend shows uniform and fine dispersion of the domains, as was represented by the standard deviation.

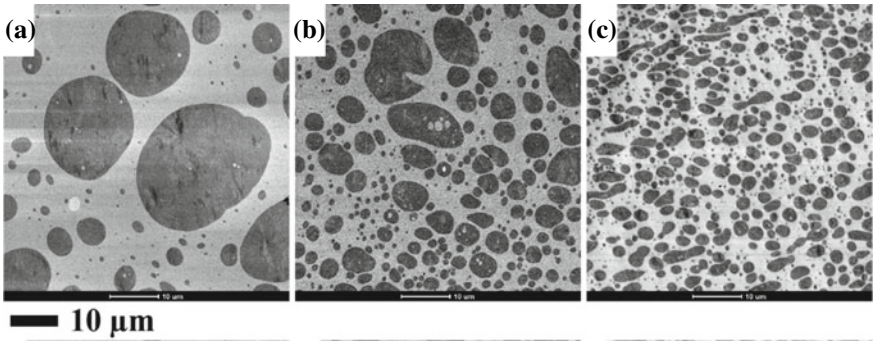

Fig. 35 STEM-BF images of PLLA/PVDF binary blend (**a**), one-step PLLA/PVDF blend with POSS-compatibilizer (**b**), and two-step PLLA/PVDF blend with POSS-compatibilizer (**c**). Reprinted with permission from Ref. [89]. Copyright 2019, American Chemical Society. All Rights Reserved

The PLLA/PVDF phase separation can be easily observed in all blends without heavy metal staining. The dark domains are found to be dispersed throughout the bright matrix. To confirm the assignment of the domains to the PVDF phase, EDX measurements were conducted, which revealed the presence of the fluorine (F)-Kα peak at 0.68 keV. Additionally, the EDX measurement results indicate that the signal counts obtained from the PLLA phase are significantly lower than those obtained from the PVDF phase. This suggests that the PLLA underwent faster degradation by the electron beam, causing the chemical bonds of PLLA to be cleaved through either backbone main-chain scission or hydrogen abstraction, producing low-molar compounds that evaporated away from the specimen. This loss of mass of the PLLA phase results in high contrast between PLLA and PVDF in the STEM-BF images.

STEM-EDX analysis was employed to investigate the distribution of the POSS-compatibilizer in the blends. The STEM-HAADF images in Fig. 36 depict the bright phase as the PVDF phase, and the elemental maps of F, Si, and O in the PLLA/PVDF interfacial regions in the blends containing POSS are presented. In the one-step blend, the distribution of the POSS-compatibilizer is concentrated at the PLLA/PVDF boundaries, as shown in Fig. 36a–d. However, the small aggregates appear unevenly distributed along the interfacial region. Meanwhile, the two-step blend exhibits a more uniform distribution with the enriched compatibilizer along the PLLA/PVDF boundary (Fig. 36g). The POSS-compatibilizer is also found in the PVDF domains in the one-step blend (Fig. 36c), while it appears to be evenly distributed in both phases in the two-step blend (Fig. 36g). The thickness of the localized compatibilizer in the one-step blend is estimated to be about 30 nm, while it is about 100 nm in the two-step blend. It should be noted that the elemental maps are projections of the cross sections of spherical domains. Thus, the estimated interfacial thicknesses are larger than the actual values. Nevertheless, the results demonstrate differences in the interfacial structures regarding the POSS aggregation formed at the PDVF/PLLA boundary in one-step and two-step blends. The oxygen maps shown here primarily

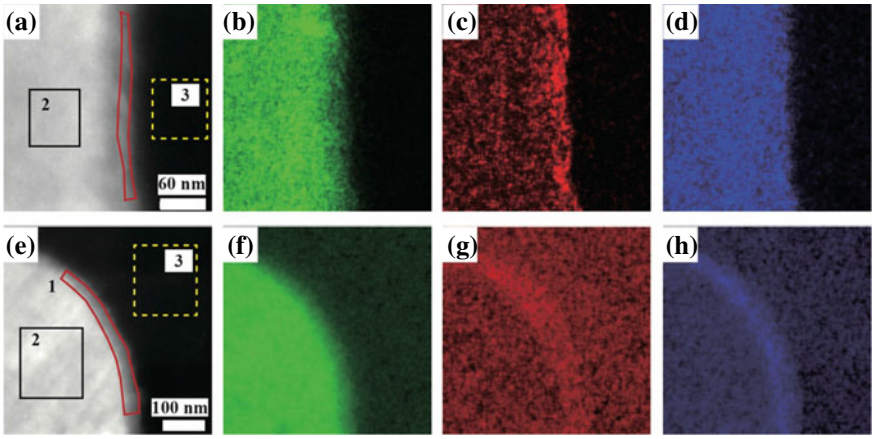

Fig. 36 STEM-HAADF images and STEM-EDX elemental maps of PLLA/PVDF/POSS(epoxy)$_5$-*g*-PMMA$_3$ blends: **a**–**d** one-step blend; **e**–**h** two-step blend. **a**, **e** STEM-HAADF images; **b**–**d** and **f**–**g** elemental distributions of F, Si, and O presenting green, red, and blue, respectively. Regions assigned by serial numbers in **a** and **e** are for acquiring EDX spectra in Fig. 37. Reprinted with permission from Ref. [89]. Copyright 2019, American Chemical Society. All Rights Reserved

represent the distribution of the POSS-compatibilizers, not that of PLLA. Due to the degradation of PLLA, the contribution from PLLA to the O elemental maps is small compared to that from POSS.

Figure 37 illustrates the overall EDX spectra and the quantified Si-Kα peaks extracted from selected regions highlighted in Fig. 36. The compatibilizer distributions are compared between the one-step and two-step blends. The Si-Kα peak intensities shown in Fig. 37a, b indicate that the two blends have different compatibilizer distributions. In the one-step blend, the Si-Kα peak intensities detected from three regions (interfacial, PVDF, and PLLA phases) differ, with the interfacial region exhibiting the highest intensity and the PLLA phase the lowest. On the contrary, in the two-step blend, the Si-Kα peak intensity obtained from the interfacial region is the highest. In contrast, the other two regions show almost equal lower intensities. The EDX mapping and spectrometry confirm that the PMMA-grafted POSS-compatibilizer can be effectively localized at the interfacial regions in both blends, but the blend sequence significantly influences the distribution of the compatibilizer.

The localization of POSS-compatibilizers at the PLLA/PVDF boundary region can be effectively visualized and quantitatively analyzed using Si elemental mapping and EDX spectral analysis. However, detecting oxygen with high signal intensity is challenging in the EDX analysis due to the radiation damage of PLLA. STEM-EELS was conducted in SI mode to carry out a detailed chemical analysis of the phase-separated structures. To obtain the oxygen ionization K-edge of PLLA with a high signal-to-noise ratio, spectra were obtained from a 500 × 500 nm area with a 50 nm interval and an acquisition time of 3 s. Therefore, the obtained spectra represent the average of 100 spectra. The beam condition was optimized with a beam size of

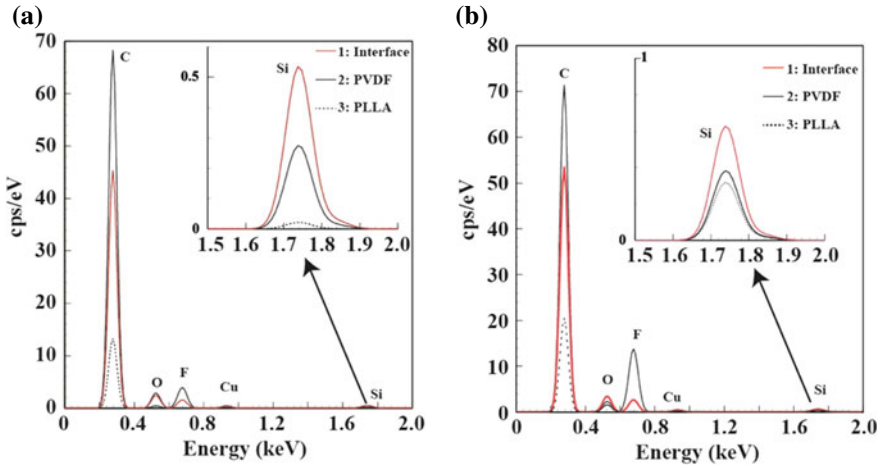

Fig. 37 STEM-EDX spectra extracted from the regions indicated in the STEM-HAADF images of Fig. 36. **a** One-step and **b** two-step blends of PLLA/PVDF blends with the reactive POSS-compatibilizer. The insets display the Si-Kα peaks that appeared in the quantified EDX spectra. Reprinted with permission from Ref. [89]. Copyright 2019, American Chemical Society. All Rights Reserved

0.74 nm and 0.293 nA beam current to get the highest jumping ratio of O K-edges. However, reducing the probe size to 0.66 nm resulted in a noisy spectrum with no core-loss signals. The EELS spectra acquisition was conducted at an accelerating voltage of 200 kV and at 110 K using a cryo-specimen holder to minimize the radiation damage to the specimens.

Figure 38 displays the O K-edge spectra obtained from the PLLA phase in the one-step and two-step blends. The O K-edge of the one-step blend shows two peaks at 533 and 543 eV, while the two-step blend reveals an additional peak at 537 eV. The O K-edge obtained from a POSS powder sample is also compared, demonstrating a shift of the edge to a higher energy-loss position and a sharp peak at 540 eV followed by a broad peak at 560 eV. The POSS powder sample's edge shape differs from those obtained in the two blend samples. Although the ester bonds of PLLA contribute to the O K-edges, they exhibit different ELNES features from each other. To investigate the cause of these differences, the impact of beam irradiation on the ELNES of the O K-edges of various oxygen-containing polymers was studied.

Different electron probe conditions were used to acquire the O K-edges of PLLA, PMMA, PET, and PPO, as presented in Fig. 39. The peak at 537 eV is highly sensitive to the beam condition. As the beam size and current increase, the peak gradually weakens and is ultimately eliminated in PLLA, PMMA, and PET. Notably, the intensity of the second peak in PLLA decreased much faster than in the other polymers, indicating poor stability of PLLA against the electron beam. Even after irradiation with a large probe, the peak in PET remains. All the investigated polymers, except for PPO, contain an ester bond, while PPO contains only an ether bond. Figure 39c

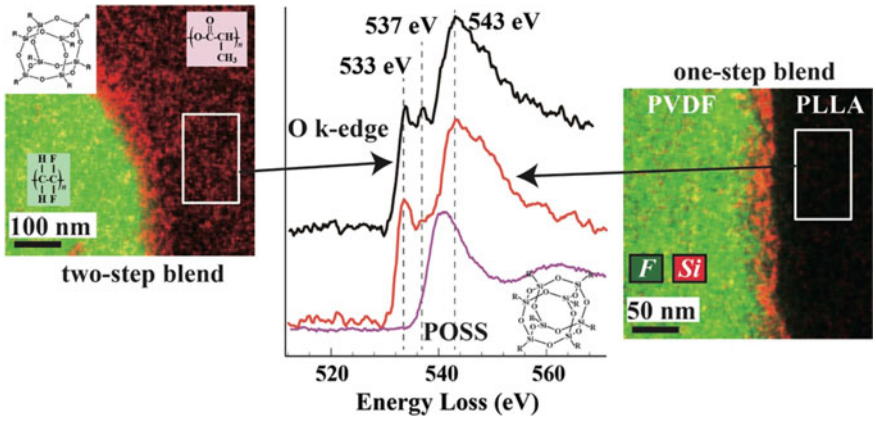

Fig. 38 STEM-EELS O K-edge spectra obtained from the PLLA phase in the one-step (*right*), two-step (*left*) PLLA/PVDF/POSS(epoxy)$_5$-*g*-PMMA$_3$ blends and from POSS. The images are STEM-EDX mixed maps, with green and red pixels corresponding to F and Si elemental distributions. Reprinted with permission from Ref. [89]. Copyright 2019, American Chemical Society. All Rights Reserved

shows a small peak at 537 eV for PPO, even with the smallest probe, indicating that the carbonyl group's oxygen mainly contributes to the beam-sensitive peak at 537 eV in the ester bond. The electron beam can easily cause chain scissions of the carbonyl group in the ester bond of the polymers, which can generate products like carbon oxide that evaporate away from the specimen.

The different O K-edge ELNES features obtained in the PLLA phases in the two blends shown in Fig. 38 are caused by the difference in the degradation behavior of PLLA. The small amount of the POSS-compatibilizer dissolved in the PLLA phase in the two-step blend can suppress the cleavage of the ester bonds, and thus the beam-sensitive peak in the O K-edge remains in the spectrum.

In Fig. 36, the Si elemental maps demonstrate that the POSS-compatibilizer selectively localizes at the interfaces of PLLA/PVDF in two different blends prepared using distinct mixing sequences. As previously mentioned, the interfacial layer formed by the compatibilizer in the two-step blend appears to be more uniform and thicker than that of the one-step blend. Moreover, the compatibilizer is mainly found in the PLLA side in the two-step blend, while it exists primarily in the PVDF phase in the one-step blend. However, analyzing oxygen by STEM-EDX is limited as PLLA and PMMA tend to degrade under STEM probe. To obtain sufficient signal gains in the EDX spectrum, scanning for an extended time with a relatively high-current probe is required. Conversely, STEM-EELS analysis using the low-current small probe permits the detection of the oxygen originating from PLLA and PMMA, as presented in Fig. 38. The results indicate that the compatibilizer is exclusively distributed in the PVDF phase in the one-step blend.

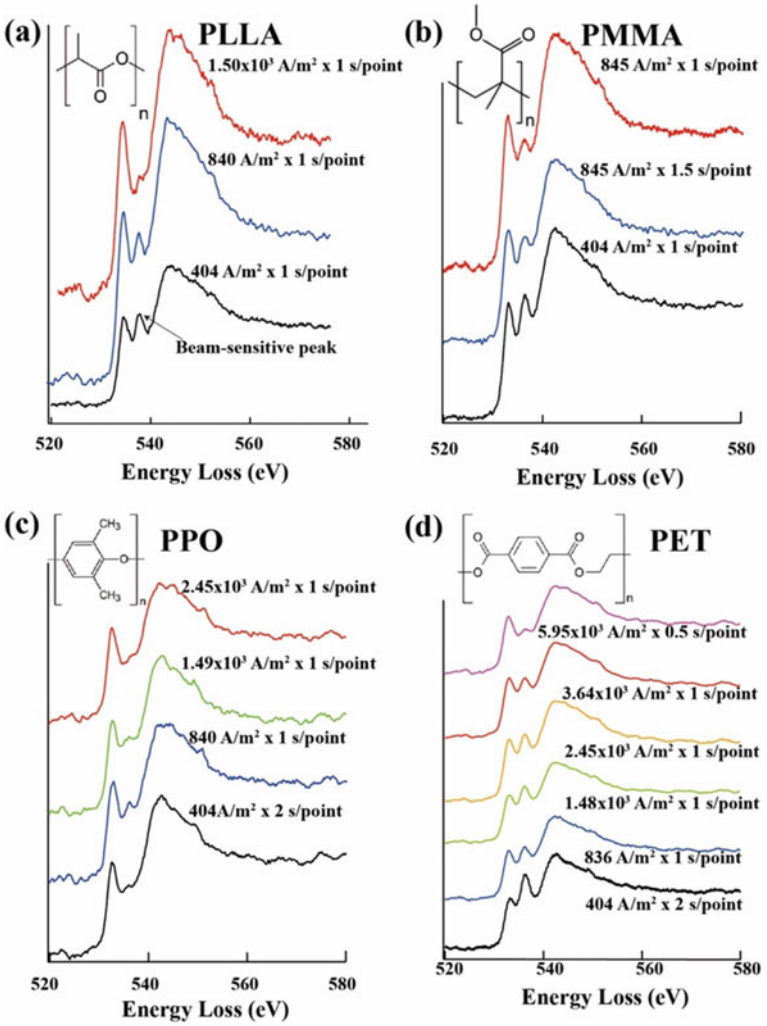

Fig. 39 O K-edge ELNES features of polymers taken with different electron probe conditions: **a** PLLA; **b** PMMA; **c** PET; **d** PPO. From the lower to upper spectrum, beam size and current are increased. The intensities of the spectra are normalized with the peak at 533 eV. Reprinted with permission from Ref. [89]. Copyright 2019, American Chemical Society. All Rights Reserved

Figure 40 illustrates the mechanism of the reactive compatibilization in blends with different mixing sequences, based on the findings. In the one-step blend (Fig. 40a), the compatibilizer tends to distribute in the PVDF phase due to the thermodynamic miscibility of PMMA and PVDF. However, when melt blending occurs, most of the compatibilizers close to the PLLA/PVDF boundary do not react with PLLA and, thus, are distributed in the PVDF phase, which does not enhance the PVDF phase dispersion in the PLLA matrix and the interfacial strength. In contrast,

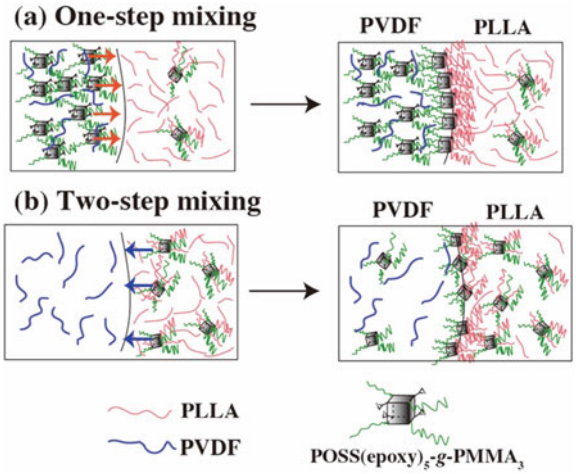

Fig. 40 Illustration depicting the processes involved in the reactive compatibilization of PLLA/PVDF blends with POSS(epoxy)$_3$-*g*-PMMA$_5$: **a** one-step blend; **b** two-step blend. Reprinted with permission from Ref. [89]. Copyright 2019, American Chemical Society. All Rights Reserved

some compatibilizers may have reacted and become occluded in the PVDF phase. Figure 40b represents the two-step blending process, where PLLA and the compatibilizer are pre-mixed to retain significant compatibilizers in the PLLA phase. When the pre-mixed PLLA/compatibilizer is blended with PVDF, the compatibilizer moves toward the PVDF phase due to the thermodynamic affinity of the PMMA chains linked to POSS with the PVDF phase. However, the reaction between PLLA and the compatibilizer prevents the complete dissolution of the compatibilizer into the PVDF phase, and it can surround the PVDF domains in a thick and uniform layer. Unreacted compatibilizers from the first step may be distributed in the PVDF phase during the second step. The reactive compatibilizer creates an interfacial layer that improves the dispersion and interfacial strength by impeding the coalescence of the PVDF domains during melt mixing [101].

5.2 ELNES Phase Mapping

Chemical state identification can be achieved through EELS by analyzing the delicate modulations that appear in the higher energy-loss region, spanning an energy width of 50–100 eV, from the ionization edge. These modulations, called electron energy-loss near-edge structure (ELNES), provide high-resolution chemical information on the excited atom beyond simple elemental composition information obtained from integrated core-loss signals. ELNES can generate maps of different material phases based on differences in their spectra. Mapping phases composed of different chemical compounds can be achieved by multiple linear least-square (MLLS) fitting of the STEM-EELS SI dataset using multiple standard spectra. Standard spectra for the MLLS fitting can be obtained from known reference samples or extracted from the dataset being analyzed. ELNES phase mapping allows for separating and

quantifying different material phases using multiple reference spectra for the same ionization edge [102]. The Fourier-log deconvolution function can be applied to the entire STEM-EELS SI datasets, extracting the single-scattering distribution (SSD) at each pixel. MLLS fitting with reference SSD spectra provides superior quantification and accurate maps for specimens with thickness variations across the data.

Figure 41 is a typical result showing the successful separation of the thin surface layer in Al6061 alloy into three aluminum compounds. An oblique section was performed with an ultramicrotome to obtain a thin section with a broader surface thin layer. EEL spectra were acquired in the STEM-SI mode with 1 s per pixel exposure time with a point-to-point distance of 5 nm. The shapes of the O K-edge ELNES of the three oxygen-containing aluminum compounds are unique and characteristic, as shown in Fig. 5c. Using those three spectra as the standards (Fig. 41a–c), the MLLS fitting was applied to the individual spectrum in the whole SI data cube acquired from the region indicated in the STEM-HAADF image (Fig. 41d). The result clearly shows that the surface layer can be divided into three phases: Boehmite is the main compound (Fig. 41f), while small amounts of $Al(OH)_3$ (Fig. 41e) and γ-alumina (Fig. 41g) are distributed. Typical fitting results of the two regions indicated in the phase maps are presented in Fig. 41h, i, which shows the core-loss edges with a 30 eV energy range, and can be well fitted with the standard spectra without noticeable errors. Thus, the compositional heterogeneity in the natural oxide layer of Al alloy can be characterized quantitatively.

As mentioned in Sect. 1.2 of "Analysis of Molecular Surface/Interfacial Layer by Sum-Frequency Generation (SFG) Spectroscopy" chapter, O K-edges of polymers exhibit ELNES features associated with the ester and the ether bonds in polymers.

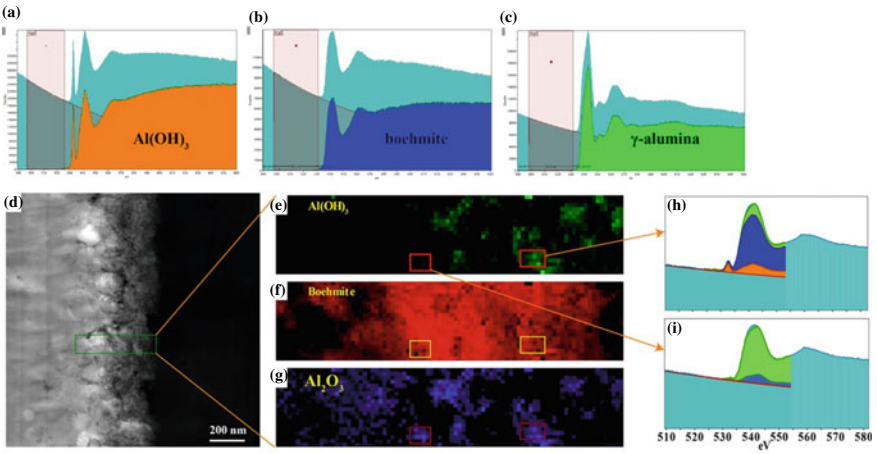

Fig. 41 ELNES phase mapping of Al6061 surface oxide layer: **a–c** standard spectra representing $Al(OH)_3$, boehmite, and γ-alumina, respectively; **d** STEM-HAADF image showing the Al6061 surface region; **e–g** phase maps of ROI indicated in **d** representing the separation of $Al(OH)_3$, boehmite, and γ-alumina phases, respectively; **h**, **i** results of the MLLS fitting of the EEL spectra extracted from the two regions in the phase maps

These represent the resistance of the polymers against the electron beam irradiation derived from their chemical structures, suggesting the possibility of the chemical identification of polymers with a high spatial resolution. The C K-edges of polymers contain ELNES that sensitively reflect chemical structures such as aromatic, carbonyl, ether, and methyl groups. Since carbon is the main element in most polymers, carbon ionization edges with high signal-to-noise ratios can be obtained with a lower electron dose than other elements, such as oxygen and nitrogen. Figure 42 shows typical examples of the C K-edges obtained from poly(ethylene terephthalate) (PET), PC, and PS. These spectra were acquired in the STEM-SI mode with an acquisition time of 100 ms and a point-to-point distance of 50 nm. After the post-acquisition processes of the BG subtraction and the deconvolution, 5 × 5 spectra in the SI data cube were summed into one spectrum. Then the ELNES reflecting the chemical structures of the polymers appeared in the C K-edges. According to the literature [103] and the spectra of other polymers we measured, the peaks can be assigned as shown therein. Careful attention should be paid to the effects of irradiation on ELNES. Upon irradiation with a higher dose, the characteristic features of ELNES may fade, resulting in similar core-loss peaks for all polymer samples. Therefore, standard spectra for the ELNES phase mapping of polymer samples should be prepared under the same condition as the SI data to be analyzed or extracted appropriately from the SI data cube being analyzed.

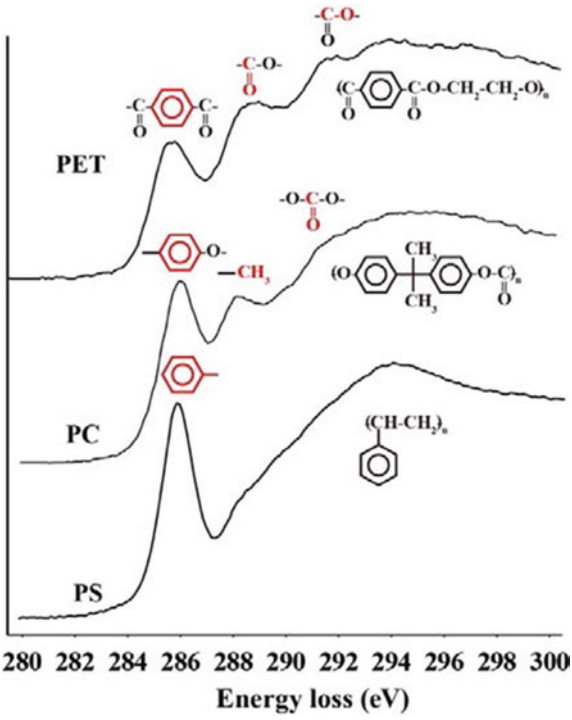

Fig. 42 C K-edge ELNESs of PET, PC, and PS with the assignments of the peaks to the chemical components

Figures 43 and 44 show the application of the ELNES phase mapping to the multi-phase structure of a PC/ABS blend. Figure 43a is an STEM-HAADF image of an unstained 50-nm-thick section, exhibiting the polybutadiene (PB) domains with the acrylonitrile-styrene (AS) copolymer occlusions, which are characteristics of the typical ABS polymer, and the presence of a light-gray phase surrounding the PB domains is confirmed. The spectral data was collected by STEM-SI mode with an acquisition time of 500 ms for one spectrum and a point-to-point distance of 10 nm. Figure 43b shows the standard spectra extracted from the three phases in the obtained SI data. These spectra exhibit distinct ELNES features in the energy-loss range from 284 to 290 eV: AS exhibits only the intense peak corresponding to the π–π^* transition of the aromatic group at 285.5 eV; PC exhibits the peak at around 288 eV corresponding to methyl group added to the peak at 286 eV assigned to the π–π^* transition of the aromatic group; and PB exhibits only the peak at 285.2 eV. Figure 44 shows the resulting maps computed by MLLS fitting using these three standard spectra, showing that the three components are successfully identified as distinct phases. The blend exhibits the multi-phase structure containing the PC phase (Fig. 44b) as the matrix and the AS phase (Fig. 44a) dispersed as the isolated domains and as the domains with the occluded PB domains (Fig. 44c). The result indicates the possibility of ELNES phase mapping with 10 nm resolution for polymer samples.

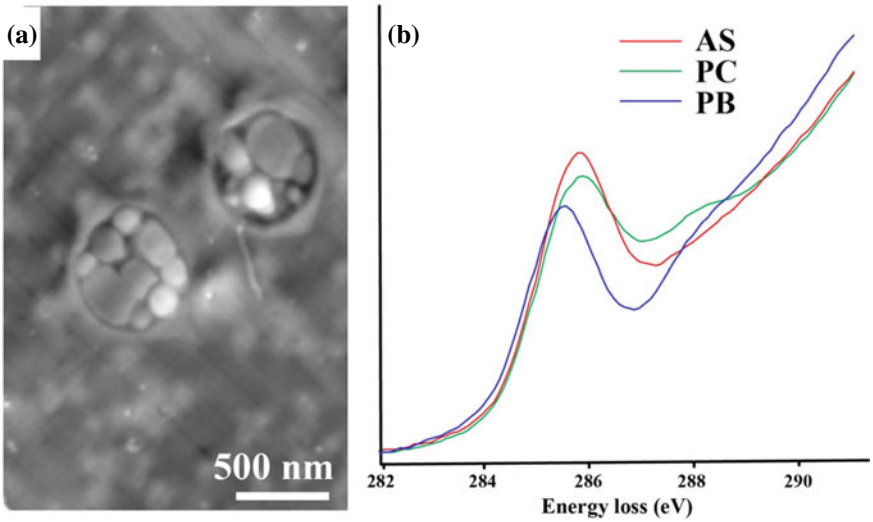

Fig. 43 STEM-HAADF image of ABS/PC blend (**a**) and C-K-edges taken from the three phases used as standard spectra for the MLLS fitting to perform ELNES phase mapping (**b**)

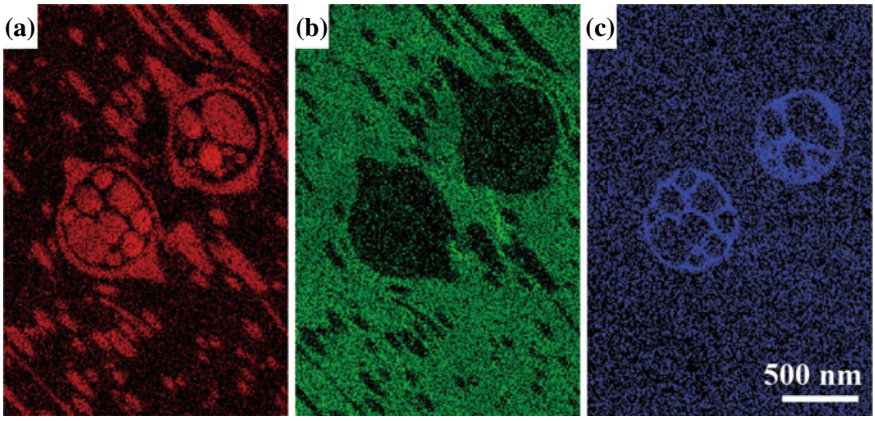

Fig. 44 **a** AS, **b** PC, and **c** PB phases in a PC/ABS blend created by ELNES phase mapping

5.3 Tomography and 3D Elemental Mapping

5.3.1 Advantages of STEM Tomography Over TEM Tomography

TEM is a technique that can be used to investigate structures at the nano-scale. However, this method only generates two-dimensional images of three-dimensional objects, which may lose information on their morphology and composition. Interpreting a three-dimensional structure based solely on two-dimensional projections may be unreliable or incomplete. Electron tomography, on the other hand, is a method that enables the reconstruction of an object's interior from its projections [104]. To perform TEM tomography, a tilt series is obtained by tilting the specimen sequentially about a single axis. Typically, the tilt series is acquired with angular increments of approximately 2° and a tilt range of ±60°. The individual images are then aligned to a common tilt axis to remove residual shifts between them. Cross correlation of the images is used to carry out the alignment of each image. Measuring the projection yields a single central plane of the 3D Fourier transform of the object. By tilting an object, its Fourier transform can be collected into a bundle of planes intersecting each other on a single axis. Inverse Fourier can obtain the original object transform.

TEM tomography has been used to investigate the three-dimensional structures of polymers and composites [105–107] since applying tomographic principles to TEM has facilitated three-dimensional analysis [108, 109]. In electron tomography, the STEM mode has often been utilized for the 3D imaging of materials. STEM tomography provides several advantages over TEM tomography, including the ability to effectively image thick specimens, dynamic focusing, and linear contrast using an annular dark-field mode [110]. Autofocusing relies on detecting contrast differences in a focused series of a small sample area. Dynamic focusing can adjust the focus as a function of specimen tilt and the distance of the scanned probe from the tilt axis, effectively removing focus gradients present in normal images due to specimen

tilt. Figure 45 shows an example of the 3D nanostructure reconstructed by STEM tomography. The sample is a cross section of a triblock copolymer film composed of PS, PMMA, and poly(*ter*-butyl methacrylate) (P*t*BuMA) with the block sequence of PS-*b*-PMMA-*b*-P*t*BuMA. The molecular weights of each block are 100, 298, and 40 $\times$ 10^3, respectively. Figure 45a is an STEM-BF image showing the 2D projection of the stained specimen with RuO_4 vapor for 30 min. PS, P*t*BuMA, and PMMA phases appear dark gray, light gray, and white, respectively. Due to the complex phase-separated structure, the 3D structure is difficult to deduce from the 2D image. STEM tomography was performed in BF mode with an angular increment of 2.5° and a tilt range of ±60°. Acquisitions were performed under cryogenic conditions of 110 K to prevent sample shrinkage due to electron beam irradiation during the tilt-series acquisition. The reconstructed 3D data were divided into three phases based on the brightness of each voxel. A 3D structure was obtained as shown in Fig. 45b, with the PS and P*t*BuMA phases shown in red and green, respectively. The volume fractions of each segment (23, 68, and 9 vol% for PS, PMMA, and P*t*BuMA, respectively) agree with the calculated values based on the molecular weight ratio. The 3D data show that PS forms a continuous phase and the P*t*BuMA phase is located between the PS and PMMA continuous phases. The detailed 3D nanostructure of the triblock copolymer can be seen in the video (Fig. 46), including the whole reconstruction procedure. In "Interfacial Phenomena in Adhesion and Adhesive Bonding Investigated by Electron Microscopy" chapter, the 3D nanostructures of the polymer/metal joint interfaces and the fracture surfaces are investigated by STEM tomography.

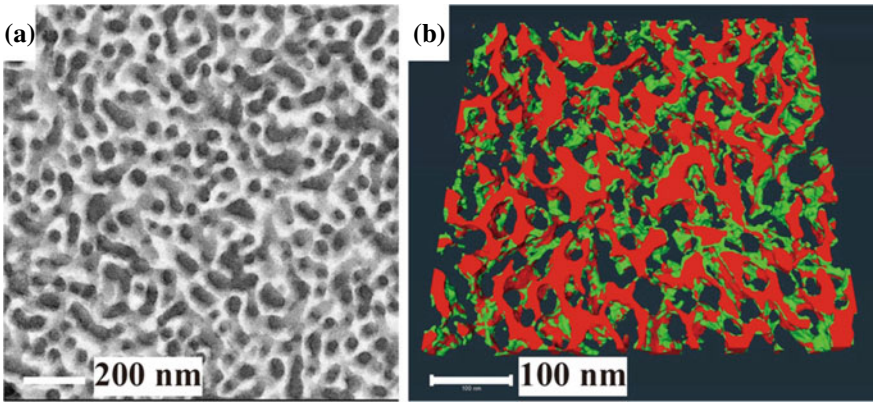

Fig. 45 STEM-BF image (**a**) and 3D reconstructed image (**b**) showing the nanodomain structure of a triblock copolymer of PS-*b*-PMMA-*b*-P*t*BuMA. The thin section was stained with RuO_4 vapor. The red and green phases are PS and P*t*BuMA, respectively

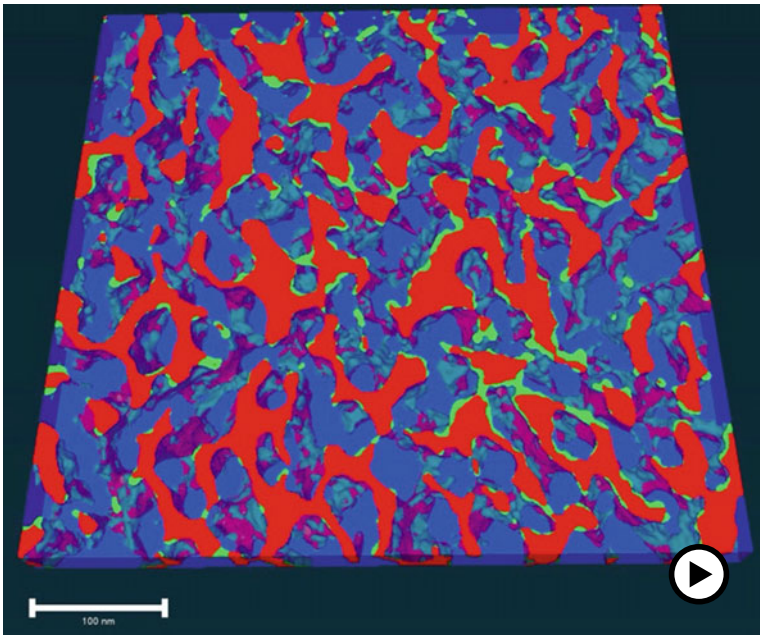

Fig. 46 Video showing the tilt series and the 3D reconstructed structure of PS-*b*-PMMA-*b*-P*t*BuMA triblock copolymer created by STEM tomography (► https://doi.org/10.1007/000-ayd)

5.3.2 3D Elemental Mapping of Rubber/Filler Blend Composites by STEM-EDX Tomography

Complex multi-component polymer systems often require detailed information about the distribution of specific elements, which can be obtained through 3D elemental mapping. This technique allows for locating components that contain specific elements within the structure. Nanoscale elemental mapping is possible using two electron microscopy methods: energy-filtered TEM (EFTEM) and STEM-EDX. As stated in the previous section, EFTEM allows us to perform elemental mapping based on electron energy-loss spectroscopy (EELS). Electron energy-loss spectroscopy (EELS)-based elemental mapping can be performed using EFTEM. However, the thickness of the specimen can strongly affect the EELS spectra, particularly during the acquisition of tilt-series images [111]. The increase in tilt angle results in increased thickness, which leads to changes in the contrast of the energy-loss images and difficulties in reconstructing 3D structures [112, 113]. As a result, EFTEM tomography is only suitable for specific specimen geometries such as cylindrical, spherical, or needle-like shapes.

Another technique used for elemental mapping is STEM-EDX. In conventional systems, X-rays emitted from the specimen are detected by a single detector located diagonally above the specimen. However, this setup can be strongly affected by the specimen tilting, resulting in the incomplete collection of emitted X-rays over the

range of tilt angles [114]. Due to shadowing effects, traditional STEM-EDX systems have difficulty detecting X-rays when the specimen is tilted away from the detector. To address this limitation, a new multidetector EDX system has been developed. This system features four silicon-drift detectors (SDDs) placed symmetrically around the optical axis near the specimen, enabling the acquisition of high-quality elemental maps with equal efficiency across the entire range of tilt angles [115, 116].

In this research, STEM-HAADF and STEM-EDX tomographies were combined to analyze the spatial distribution of silica nanofillers in two-phase immiscible polyisoprene/styrene-butadiene (IR/SBR) rubber blends and to evaluate the influence of silica loading on the phase-separated morphologies of the blends [117]. Different weight ratios of IR, SBR, and silica were melt-mixed, and thin sections (~150 nm) were produced by cryoultramicrotomy at a temperature of −130 °C. The sections were then stained with OsO_4 vapor for 15 h at 50 °C. STEM bright-field (BF) images of the IR/SBR/silica blend composites with IR/SBR weight ratios of 70/30 (Fig. 47a–d) and 30/70 (Fig. 47e–h) are shown in Fig. 47. The blends without silica (Fig. 47a, e) exhibit coarse phase separations with irregularly shaped domains. The SBR phase is stained relatively more strongly, resulting in the gray-colored phase in the STEM-BF images. OsO_4 staining cross-links the polymer chains by staining polymers containing carbon–carbon double bonds. Both rubber phases are stained, but the SBR phase is stained more strongly in the blends without silica. The small IR domains observed in the 30/70 IR/SBR blend (Fig. 47e) are stained much more strongly than the IR matrix, implying that OsO_4 staining depends on the domain size. OsO_4 staining enhances the elastic scattering of electrons and can help make IR/SBR phase separations visible by introducing the heavy atom. Additionally, it can improve the specimen's stability against beam irradiation to prevent shrinkage of the phase structures [52]. The phase separation and image contrast change when silica nanofillers are added at 25, 50, or 70 phr (weight parts per hundred rubber) to the 70/30 IR/SBR blend, as depicted in Fig. 47b–d, respectively. The SBR domains become smaller and appear brighter when silica is present. Identifying the IR/SBR phase separation is challenging when the silica content is 70 phr (Fig. 47d) because the volume fraction of the silica is high (23%). The same trend is observed for the SBR-rich blends (Fig. 47f–h), where the IR phase is stained more strongly than the SBR phase in the presence of silica. This phenomenon may be due to the reduced domain size and silica loading on the rubber phases' staining.

Relying solely on STEM-BF images does not allow for clear visualization of the silica distribution and the IR/SBR phase separations. When unstained, the silica is visible, but the two rubber phases cannot be distinguished. Staining with OsO_4 improves the visibility of the rubber phases, but the contrast between the two rubber phases and silica may be insufficient, making it challenging to identify the silica. Combining STEM-HAADF imaging and STEM-EDX elemental mapping could be the best way to distinguish the silica and the IR/SBR phase-separated morphologies. Figure 48a, b shows an STEM-HAADF image and the corresponding Si elemental map of a 50/50/50 IR/SBR/silica blend composite, respectively. The STEM-HAADF image exhibits a high contrast between the IR and SBR phases, in which the bright and dark phases correspond to the IR and SBR phases, respectively. The STEM-EDX

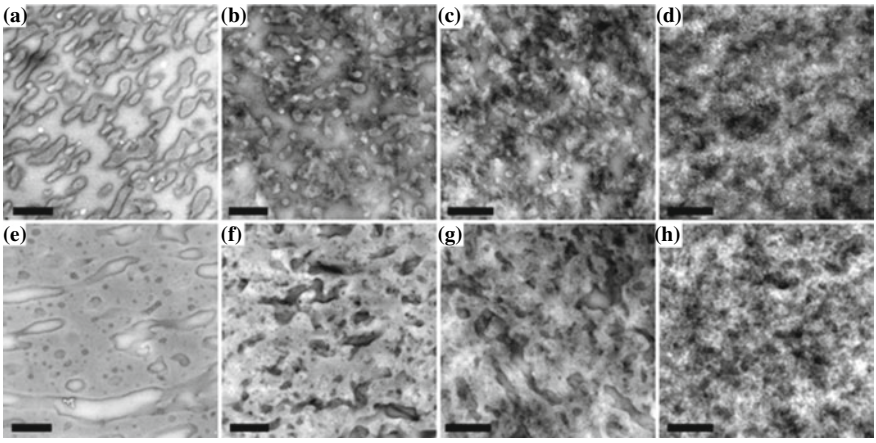

Fig. 47 OsO_4-stained STEM-BF images showing the impact of silica nanofiller loading on the phase-separated morphologies of IR/SBR rubber blends: **a**–**d** 70/30 (wt/wt) IR/SBR ratio; **e**–**h** 30/70 (wt/wt) IR/SBR ratio. The silica contents are 0 (**a**, **b**), 25 (**b**, **f**), 50 (**c**, **g**), and 70 phr (**d**, **h**). Scale bars represent 500 nm. Reprinted with permission from Ref. [117]. Copyright 2021, John Wiley & Sons. All Rights Reserved

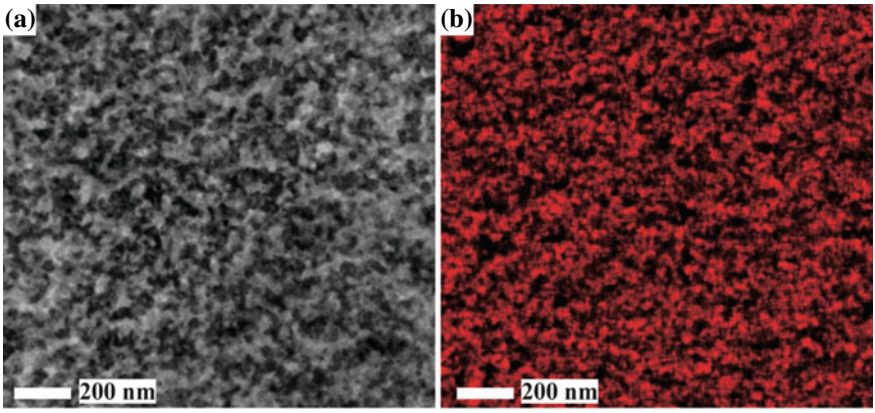

Fig. 48 STEM-HAADF (**a**) and STEM-EDX Si elemental distribution (**b**) images of 50/50/50 IR/SBR/silica blend composite. Reprinted with permission from Ref. [117]. Copyright 2021, John Wiley & Sons. All Rights Reserved

Si elemental map presents only the location of the silica, which cannot be seen in the STEM-HAADF image. The overlap of the Si elemental map onto the STEM-HAADF image could recognize that the silica is mainly distributed into the SBR phase. The combination of STEM-HAADF tomography and STEM-EDX tomography could be promising for quantifying the distribution of the silica in the two rubber phases three dimensionally.

Figure 49a, b displays the EDX spectra obtained at tilt angles of 0° and −55°, respectively. The spectra exhibit energy regions, including the Si, W, Os, and S peaks. The W peak originates from the specimen holder and is more significant at higher tilt angles. The Cliff–Lorimer method is used to separate the overlapping peaks [118]. Figure 50 presents the tilt-angle dependence of the deconvoluted Si Kα peaks intensities for 30/70 IR/SBR blends with 70 phr silica contents. The EDX signals with sufficient intensities were collected symmetrically over the entire range of tilt angles. In contrast, a single detector yielded low EDX signal intensities, even at the highest silica content of 70 phr. The negative tilt angles did not yield any signals when the specimen was tilted to the opposite side of the detector (green data points in Fig. 50). Thus, the multidetector EDX system is essential for performing the 3D elemental mapping.

A video demonstrating the process for combined STEM-HAADF and STEM-EDX tomography is presented in Fig. 51. STEM-EDX tomography was performed using a 0.7 nm electron probe and 0.5 nA current, with a 30 μs/pixel dwell time. The resulting 512 × 512 pixel maps were obtained by scanning for 5 min and integrating the signals. The alignment of the tilt series of STEM-HAADF images and the Si elemental maps was performed in parallel using the same conditions. Then, the two tilt series were separately reconstructed into 3D volumes. The 3D structure reconstructed from the STEM-HAADF images represents the IR/SBR phase-separated morphology, classified into two segments corresponding to the IR and SBR phases. The Si 3D map is binarized to extract the silica part. Finally, these three parts are combined into a single 3D volume. The silica part is divided into two parts: distributed in the IR phase and the SBR phase.

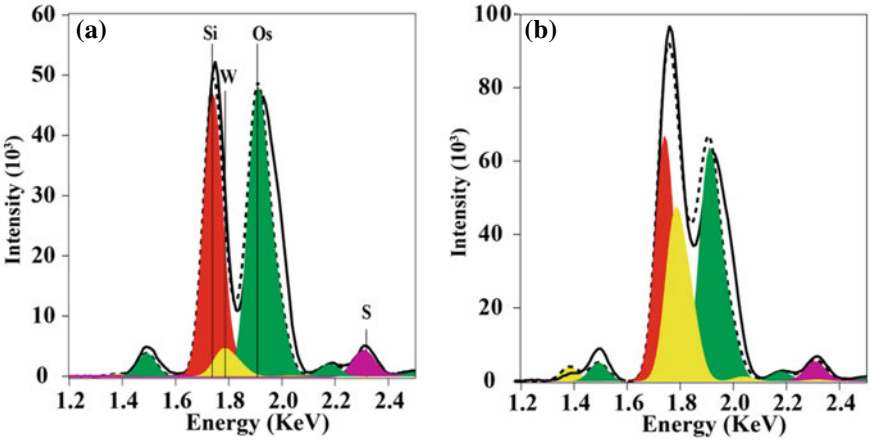

Fig. 49 EDX spectra showing the Si, W, Os, and S peaks of 30/70/50 IR/SBR/silica blend composite at tilt angles of 0° (**a**) and −55° (**b**). The peaks are separated by deconvolution. The solid and dotted lines are as-obtained and the sum of the deconvoluted spectra, respectively. Reprinted with permission from Ref. [117]. Copyright 2021, John Wiley & Sons. All Rights Reserved

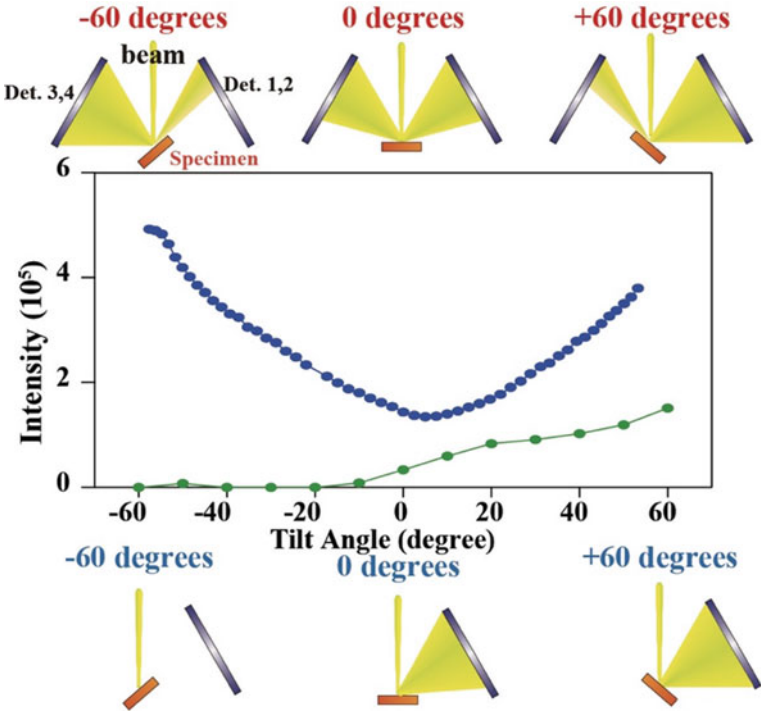

Fig. 50 Tilt-angle dependence of the Si Kα peak intensities for 30/70 IR/SBR blends containing 70 phr silica (blue), and the signal intensities of 60/40/70 IR/SBR/silica obtained with a single detector (green dots). Angle dependence EDX signal detection in the multidetector (upper) and the single-detector (lower) systems are schematically illustrated

Figure 52 shows the distributions of silica and the effects of silica loading on the phase-separated morphologies of 30/70 and 70/30 IR/SBR blends. The dark blue, light blue, red, and yellow parts correspond to the SBR, IR, silica in SBR, and silica in IR, respectively. The figure clearly shows that silica is preferentially distributed in the SBR phase. Still, some silica also escapes into the IR phase when SBR is the minor component of the blend. It also shows that loading silica into the blends improved the dispersion of the minor rubber component.

A combination of STEM-HAADF and STEM-EDX tomography was utilized in this study to examine the 3D distribution of nano-sized silica in binary rubber blends. This approach enables the investigation of silica distribution between the rubber phases in highly silica-filled blends at 70 phr (23 vol%), which is not easily discernible using conventional 2D TEM. The quantification of silica distribution between the rubber phases demonstrates that silica is preferentially located in the SBR phase. Still, it can also be present in the IR phase when the IR fraction in the total rubber components is above 40 wt%. The phase-separated morphologies of IR/SBR blends are significantly impacted by silica loading, resulting in a fine

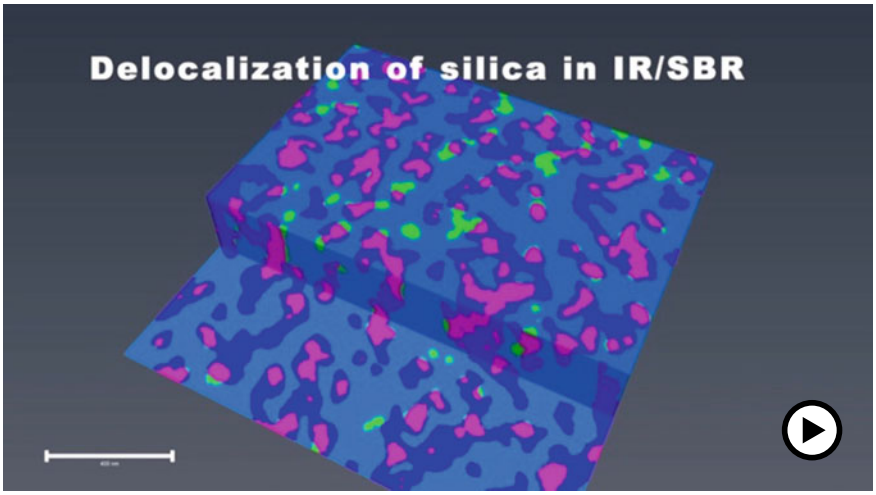

Fig. 51 Video showing the reconstruction procedure and the 3D image of the IR/SBR rubber blend with silica (► https://doi.org/10.1007/000-ayb)

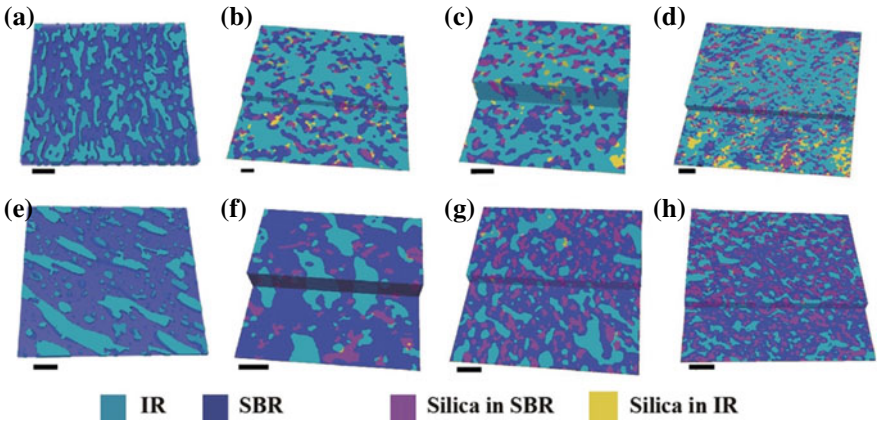

Fig. 52 Silica content dependence of the 3D structures of IR/SBR blends: **a**–**d** 70/30 (wt/wt) IR/SBR blend; **e**–**h** 30/70 (wt/wt) IR/SBR blend. The silica contents are 0 (**a**, **e**), 25 (**b**, **f**), 50 (**c**, **g**), and 70 (**d**, **h**) phr. Scale bars represent 200 nm. Reprinted with permission from Ref. [117]. Copyright 2021, John Wiley & Sons. All Rights Reserved

dispersion with high phase connectivity. This is due to the preferential distribution of silica in the SBR phase, which decreases the matrix/domain viscosity ratio. The manipulation of silica distribution in multi-phase polymer systems can be achieved by surface modification of silica, resulting in the optimization of rubber composite properties. The visualization method utilized in this study provides comprehensive structural information on multi-component polymer composite structures.

5.3.3 Multiple 3D Elemental Mapping by STEM-EDX Tomography of the Laser-Modified Galvanized Steel Surface

The surface modification of metallic substrates by laser irradiation has been recognized as a robust way to achieve adhesive bonding with high strength and durability [119–121]. Laser treatments with different power, wavelength, and scanning processes have constructed various surface topological structures. Galvanized steel sheets have been extensively used for automobiles. The steel sheet is covered with a uniform zinc-plated layer by controlling the amount of zinc coating. The zinc-plated layer itself is chemically treated, which ensures excellent corrosion resistance. Here, a laser-irradiated galvanized steel (Zn–Fe) surface is investigated to study the mechanism of the evolution of the laser-induced surface structures []. A low-magnification SEM micrograph (Fig. 53a) shows a topological surface structure created along the laser scanning direction. Deep trenches are formed by laser scanning, generating wavy threads and spherical objects between adjacent trenches. The spherical objects are created at periodic intervals on the thread. The high-magnification view of the spherical object surface shown in Fig. 53b indicates that the finer topological structure is built on the surface of the globules. FIB cross section along the line shown in Fig. 53b provides evidence that the globules are over 10 μm in height and that additional nanometer-scale topological structures have been created on the globule surface.

STEM-EDX elemental analysis was carried out with a thin specimen prepared by the FIB fabrication. Figure 54 shows the STEM-HAADF image and the 2D elemental distributions of O, Fe, and Zn in the surface layer created by laser irradiation on steel. The iron- and zinc-rich layers are involved in the oxygen-rich layers formed on steel. This layer is thought to be formed by the deposition of iron and zinc oxidation products vaporized by laser irradiation. Elemental distribution images of Fe and Zn suggest that the ZnO layer is first created on the steel substrate. Then the iron oxide layer is deposited on the ZnO layer. After the double-dense layer is formed, a porous layer with a Zn-rich top is formed. The 2D elemental maps, however, have limitations in understanding the true complex surface microstructures. Therefore, STEM tomography was performed to reconstruct the 3D surface structure created by

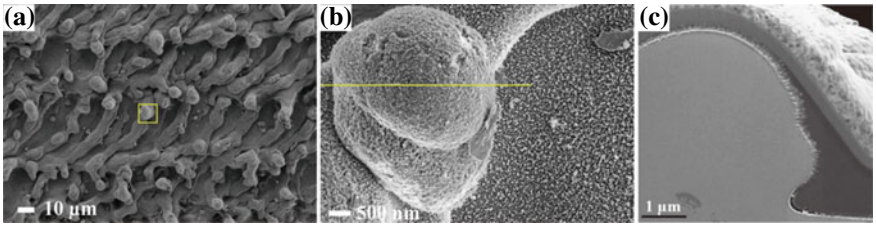

Fig. 53 SEM micrographs showing the surface topographic features of the Zn-coated steel created by laser irradiation. **a** Is a low-magnification image and **b** is the magnified view of the region indicated in **a**. **c** Is a cross section created by FIB along the line shown in **b**. Prof. S. Hartwig and Dr. C. Gndrach, Technische University Braunschweig, provided the sample

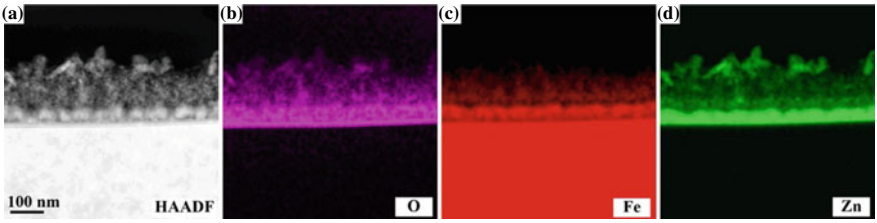

Fig. 54 Cross-sectional images of the laser-irradiated Zn-coated steel surface: **a** STEM-HAADF; **b–d** STEM-EDX elemental maps of O, Fe, and Zn, respectively

the laser irradiation, as shown in Fig. 55. A tilt series of the STEM-HAADF image (Fig. 55a) with the angular increment of 2.5° and the tilt range of ±60° was acquired, allowing the 3D reconstruction as displayed in Fig. 55b, c. The 3D image data makes viewing the structure at any angle, distance, or position possible. Looking at the 3D structure, we can see that the object existing in the upper layer is a thin plate. In the 2D image, the bottom bilayer looks like continuous film, but in the 3D image, we can confirm that these are porous.

Next, to know more about the 3D structure, the chemical structure of the surface layer was investigated by STEM-EDX tomography. STEM-EDX map data was acquired at each tilt angle using an electron probe of 0.7 nm diameter and 0.5 nA current with a 30 μs/pixel dwell time. 512 × 512 pixel EDX elemental map data was obtained by integrating the signals for 5 min scanning at each tilt angle. Figure 56 shows a video demonstrating the STEM-EDX tomography and the 3D viewing of the elemental maps. The Zn and Fe 3D elemental maps were constructed in parallel and then these two were combined into one 3D volume data. Figure 57 shows 3D views of the Fe and the Zn 3D elemental maps separately. The multiple 3D elemental maps are shown in Fig. 57c, where the Fe and Zn distributions are presented as red and green voxels, respectively. The yellow voxels represent the co-existing Fe and Zn elements. Thus, the multiple 3D elemental maps provide detailed structural information on the nano-scale regarding topological and chemical structures. We learned that the laser treatment on the galvanized steel could create a unique surface structure, including the co-continuous porous structure with the ZnO nanoflakes on the outermost part.

The steel surface is initially covered with a thick, uniform Zn-coated layer about 10 μm thick. Laser scanning locally heats the steel surface to a temperature high enough to melt it, creating micrometer-scale anisotropic topological structures due to the mechanical effect of the laser. At the same time, zinc and iron evaporate from the surface of the steel, oxidize in the air, and are deposited onto the molten iron surface. The porous structure is formed during the evaporation–deposition process, and finally the large zinc nanoplatelets are deposited.

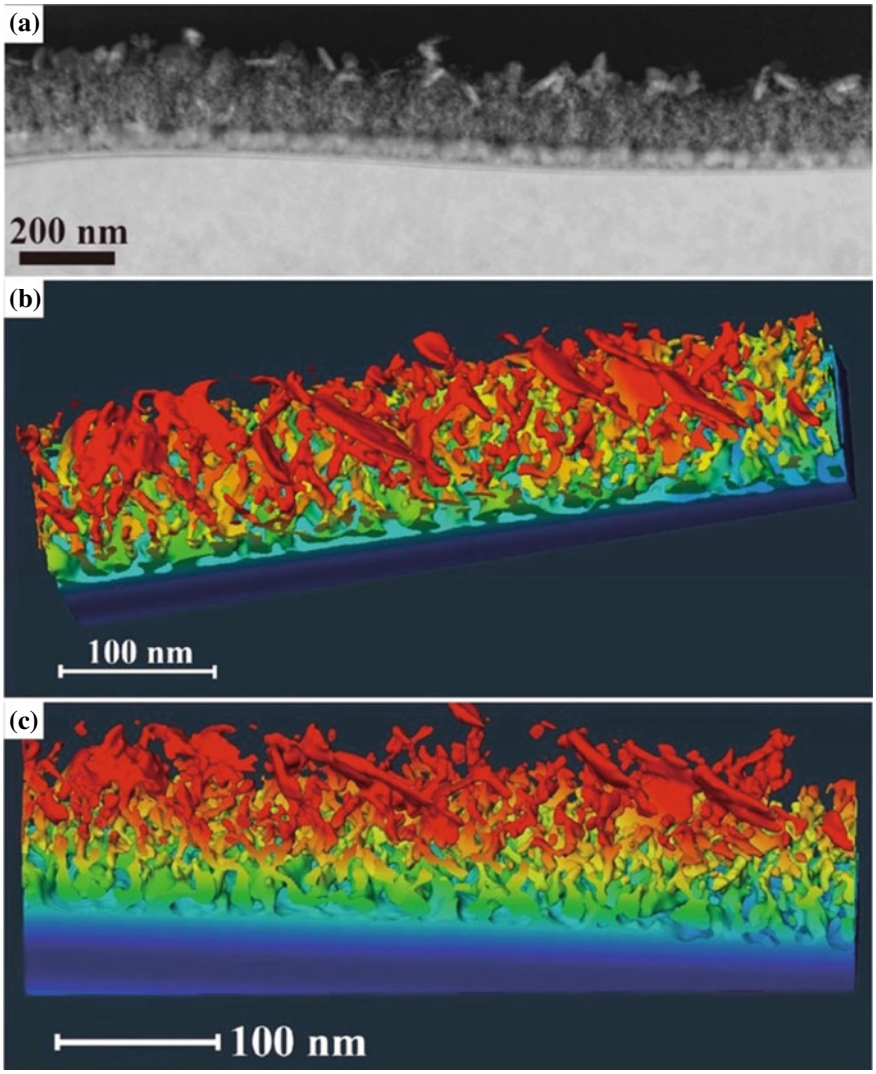

Fig. 55 TEM-HAADF tomography of the laser-irradiated Zn-coated steel surface: **a** STEM-HAADF image at 0° tilt angle; **b**, **c** 3D views obtained from the reconstructed 3D image data. The color represents the distance from the bottom plane

6 SEM

One method for producing a magnified image of a sample is SEM, which works by scanning an electron beam on a specimen surface and detecting the electrons that are emitted from its surface due to the interaction with the beam. As the electron beam scans line by line over the specimen, it generates various types of electrons

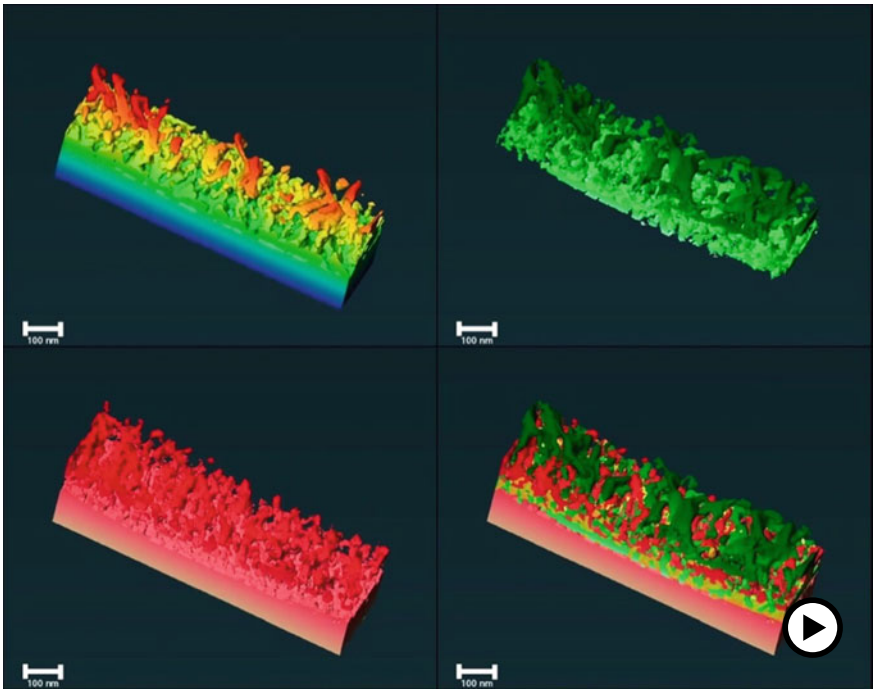

Fig. 56 Video demonstrating the STEM-EDX-tomography and the 3D viewing of the elemental maps of the laser-irradiated Zn-coated steel surface (▶ https://doi.org/10.1007/000-ayf)

that carry unique structural information about the sample, differing in origin, energy, and direction of travel. Several types of electrons are generated as the result of the energetic bombardment of the specimen by the primary beam electrons (PEs) as stated in Sect. 1. SEM imaging employs both secondary electrons (SEs) and back-scattered electrons (BSEs) that are emitted from the surface of the sample to produce contrast in the image. The contrast in BSE mode is primarily determined by the atomic number (material contrast). In contrast, SE mode is mainly based on the local surface inclination relative to the incident beam (topographic contrast). For imaging topographic features of surfaces in polymeric materials, the SE mode is often preferred. The SEs are low-energy electrons (<50 eV) that originate from the sample and play a role in forming the image.

Loosely bound electrons in the valence or conduction band of the sample atoms give rise to SE emission. When PEs interact inelastically with the sample atoms, they generate SEs that escape from the sample into the vacuum. The energy of SEs is very low, around 50 eV, which limits their mean free path in solid matter. As a result, SEs can only escape from the top few nanometers of the sample's surface. The signal from SEs is usually concentrated at the point where the primary electron beam impacts the sample. Two primary types of SEs, SE-I and SE-II, are generated from the sample, as illustrated in Fig. 58a [122]. SE-I originates from the direct interaction

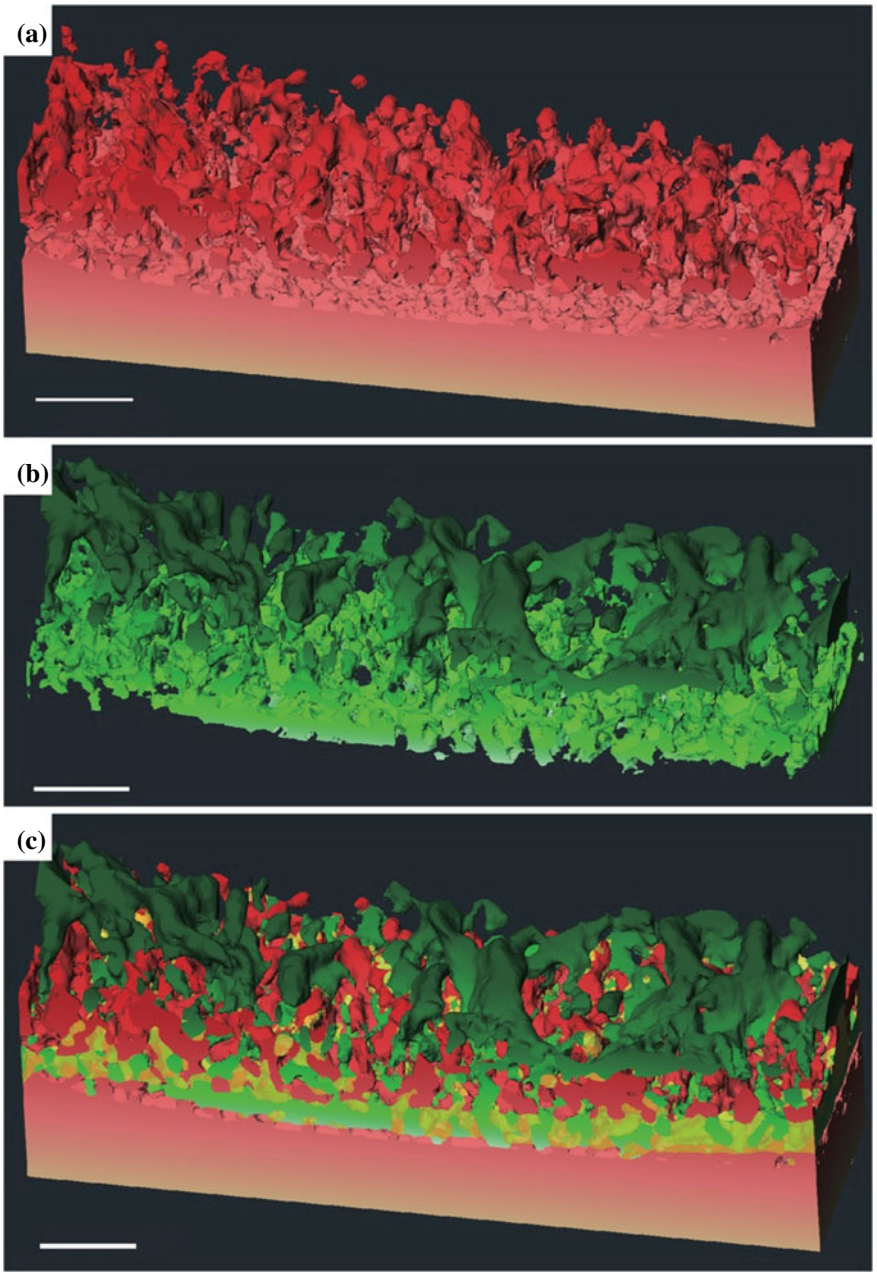

Fig. 57 3D elemental maps of the laser-irradiated Zn-coated steel surface created by STEM-EDX tomography: **a** Fe distribution image; **b** Zn distribution image; **c** mixed map of Fe (red), Zn (green), and Fe/Zn co-existing (yellow) region. Scale bars correspond to 100 nm

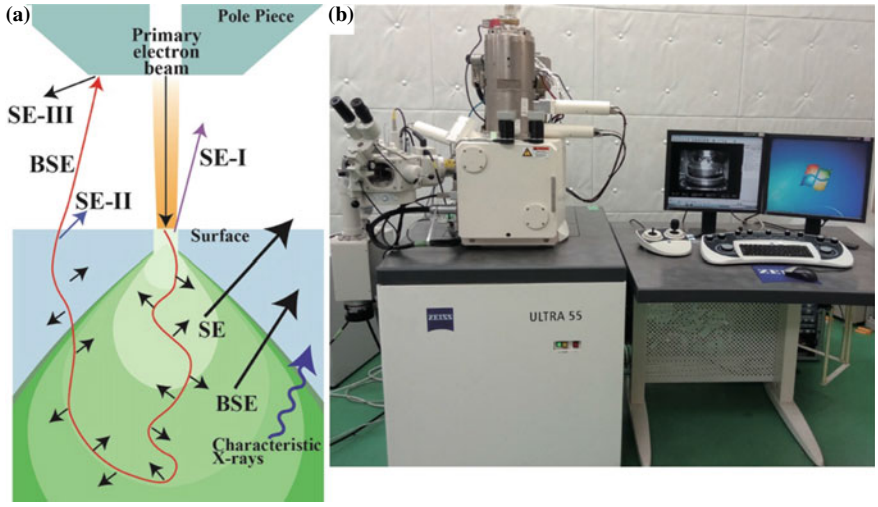

Fig. 58 Schematics of a typical specimen–electron interaction volume (**a**). SE-I is generated from the point of intact, while SE-II is generated by BSEs raveled in the sample. SE-IIIs are generated when high-energy BSEs from the sample strike the objective pole piece or the chamber walls and the appearance of an FE-SEM instrument, Ultra 55 (Carl Zeiss) (**b**)

of the primary electron beam with the sample near the beam impact point, while BSEs produce SE-II. The inelastic mean free path of SEs is relatively short, typically 1–3 nm and is energy dependent. When some PEs penetrate the sample, they lose energy through inelastic collisions before exiting the vacuum. Since BSEs, which create SE-IIs, also travel a certain distance within the sample, SE-IIs are emitted from the sample's surface at locations significantly away from the primary beam impact point.

Apart from SE-I and SE-II, another type of SE, called SE-III, can also be generated. These electrons are produced when high-energy BSEs, which exit the sample, collide with the objective pole piece or the chamber walls, resulting in SEs from these surfaces. This background signal adds unwanted noise to the signal from the sample. SE-I provides high-resolution, surface-specific information about the sample since the spatial resolution depends on the size of the primary electron beam. On the other hand, SE-II is generated from a broader and deeper volume than SE-I and reflects at a lower angle, making it carry inherently lower resolution topographic information.

6.1 Energy-Filtered SE Imaging

As described in Fig. 2c, the column of the SEM instrument used in our study (Fig. 58b) integrates two detector systems for the collection of the SE signals: One is a conventional scintillator-type detector located outside the objective lens and the other is an

annular type positioned above the objective lens "on-axis". Those two detectors are called the "chamber detector" and the "in-lens" detector, respectively. SEs emerging from the sample surface are attracted and accelerated by the positively biased electrode of the beam booster and finally projected onto the in-lens detector [123]. The electrostatic lens formed at the entrance of the objective lens accelerates the SE electrons backward and directs them into the in-lens detector. The in-lens detector mainly collects SE-I secondary electrons, while the chamber detector collects SE-II secondary electrons. Thus, the chamber detector is called the SE2 detector. Figure 59 presents a typical example for comparing the two SE images created by the two detectors at an acceleration voltage of 1.9 kV and a working distance of 3 mm. The specimen is a fracture surface of a welded interface between PS sheets that failed by the double beam cantilever (DCB) test, of which detail is shown in Sect. 3.2 of "Interfacial Phenomena in Adhesion and Adhesive Bonding Investigated by Electron Microscopy" chapter. It shows that the in-lens detector provides a higher resolution image (Fig. 59a) with detailed "nanofibrillar" structures visible clearly than the SE2 detector (Fig. 59b). The SEs collected with the in-lens detector originate from the very surface of the sample. The SE-I signal is commonly used to image surface details at the highest resolution at the expense of compositional information. The SE-II signals, on the other hand, are generated from a deeper and broader volume in the sample, resulting in poor image quality.

An interplay of accelerating voltage, detector selection, and working distance determines the quality of an SE image. The three imaging parameters should be optimized to obtain the best image quality for the samples under study. The influence of the three parameters on the SE image quality was investigated using a thin section of a semicrystalline polymer stained with RuO_4. The image quality discussed here is defined as "containing well discernable crystalline structural information" in an image. As stated in Sect. 3.2.2, the spherulites and the lamellae in PLA could be observed by the RuO_4 staining in the TEM mode. SEM can also provide a global image of the thin section fixed on a copper grid by the SE2 detector, as shown in Fig. 60. Figure 61a, b shows SE images detected by the in-lens detector and the SE2 detector, respectively, of the stained PLA section in the window of the copper grid. In contrast to high-resolution SE images of normal bulk polymer samples (Fig. 59), the two detectors have opposite effects on the resulting image quality. Because the in-lens detector mainly collects SE-I secondary electrons originating from the sample surface, the detector visualizes the electrons adsorbed on the sample surface like clouds due to the charging, which obscures to see the underlying structures. The negatively charged surface reflects many incoming electrons, creating very bright areas in the image. These regions deflect the electron beam, causing a blurring of the image. The SE2 detector, on the other hand, collects SE-II electrons generated from a deeper and wider volume within the sample. Because SE-II electrons have a considerable sample interaction depth, they contain topographical and compositional information. Therefore, the SE2 image represents the structure inside the section containing the compositional information produced by the selective staining.

The SE imaging with the two-detector system allows us to perform energy-filtered surface imaging, which offers the opportunity for high-resolution surface imaging

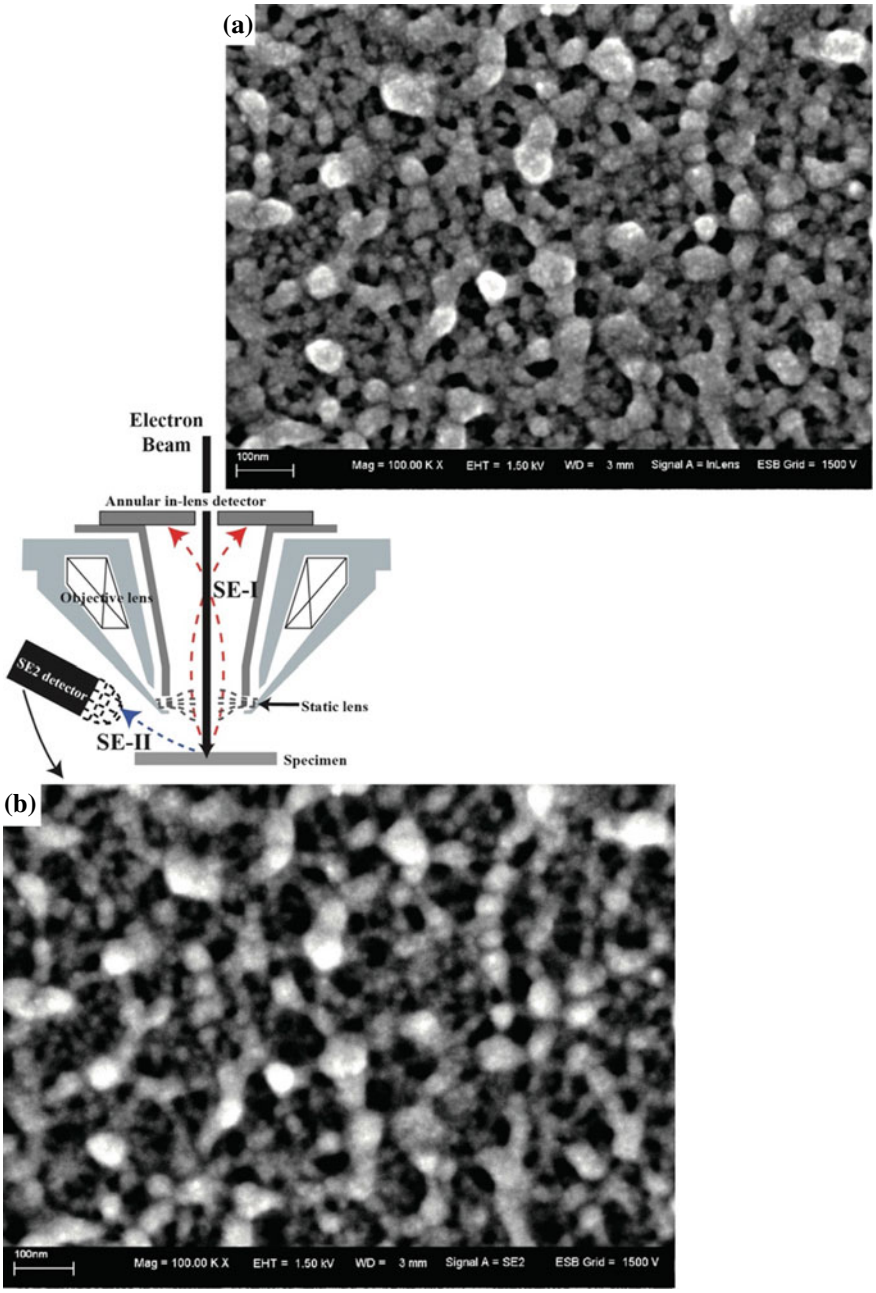

Fig. 59 SEM micrographs of the fracture surface developed in the failure of the welded PS interface in a DCB test: **a** SE image using the in-lens detector; **b** same region obtained using the SE2 detector

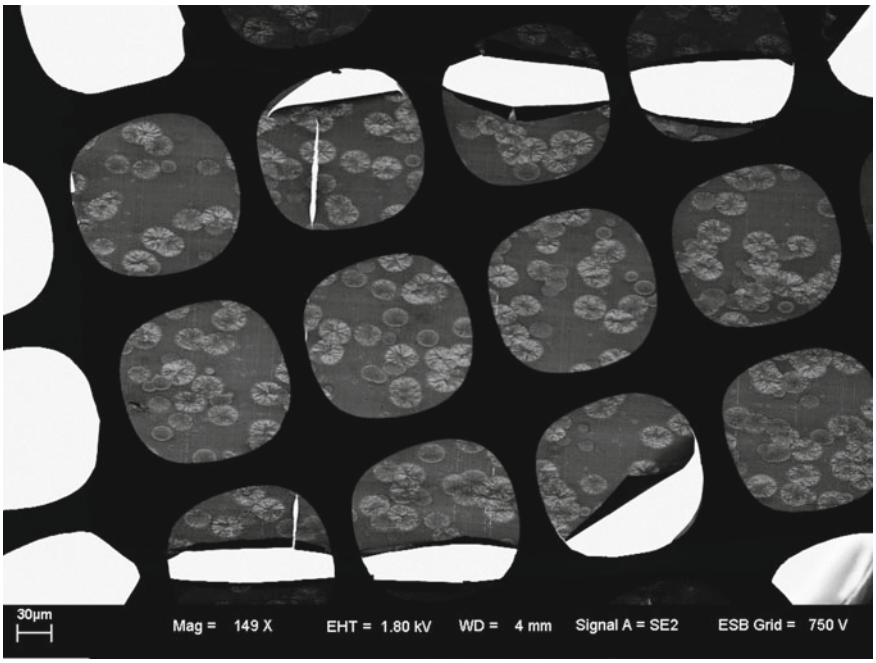

Fig. 60 SEM micrograph taken by the SE2 detector at 1.8 kV acceleration voltage showing a global image of the thin section of PLA stained with RuO_4

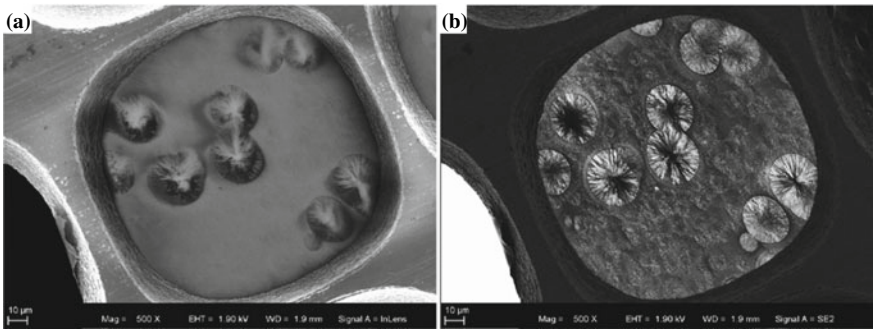

Fig. 61 SEM micrographs showing the spherulites of PLA distributed in the amorphous matrix: **a** SE image detected by the in-lens detector; **b** SE image detected by SE2 (chamber) detector (**b**)

of polymer specimens [124]. As mentioned above, SEs are the electrons that escape from the specimen surface with energies below about 50 eV, while BSEs are the primary electrons that undergo large deflections and leave the specimen surface with high energy similar to that of the primary electrons. The distribution of SEs into the two detectors according to their energy can be controlled by changing the working

distance. Figure 62 displays the series of in-lens (left column) and SE2 (middle column) images with varying working distances from 1.9 to 12.2 mm at the fixed accelerating voltage of 2.2 kV. As shown in Fig. 62i, j, the threshold energy, at which the SEs are divided into the two detectors, shifts from higher to lower when the working distance becomes longer. The in-lens image and the SE2 image at the same working distance vary with the threshold energy as shown by the changes from top to bottom in Fig. 62. With a large fraction of SEs distributed to the in-lens detector (Fig. 62i), the in-lens images represent the charging of the sample (Fig. 62a, b), while the SE2 image shows the underlying structure with good contrast (Fig. 62e, f). As the working distance increases, the in-lens images become darker and eventually, no brightness is gained at the working distance of 12.2 mm as shown in Fig. 62d. A longer working distance results in fewer SEs distributed to the in-lens detector. The SE2 images, on the other hand, become brighter as the working distance increases, and eventually the images become anomalously bright, and fine structures are obscured as shown in Fig. 62h. With a long working distance, most of the generated SEs, including SE-I, will be directed toward the SE2 detector and consequently unable to separate the charging contribution from the SE2 image. The threshold energy that splits the SEs between the two SE detectors can be optimized simply by changing the working distance, removing charging, and optimizing the contrast of the SE2 image.

As described above, the charging problem in the SE image of the PLA thin sections could be resolved by the energy filtering of the SEs. Next, using the same PLA specimen, we evaluated the effect of the accelerating voltage of the PE on the SE2 image. Figure 63 shows the changes in image quality of the SE2 image when the working distance is fixed at 3.9 mm which is determined in the above experiment and the accelerating voltage is varied in the range of 1.5–5.0 kV. A sufficiently bright image cannot be obtained at the experiment's lowest voltage due to the low SE yield. As the voltage is increased, the optimum quality is found to be obtained at 2.2 kV. When the accelerating voltage is further increased, the image brightness is too high to find the structural details in the specimen. To understand the effect of the PE energy on the SE image contrast, Monte Carlo simulations were employed to calculate an interaction volume where entering electrons interact with atoms in a 100-nm-thick carbon film as shown in Fig. 63. It demonstrates how this interaction volume is affected by accelerating voltage, where the blue lines represent the PEs spreading in the sample, and the red lines represent the BSEs generated and escaping from the surface. At the lowest PE energies (1.5 kV), electrons interact with sample atoms to a depth of about 40 nm. The PE pass distribution is pear shaped and spreads into the sample in the lateral direction. Therefore, the PEs cannot reach the bottom of the sample and go outside.

On the other hand, elevating the accelerating voltage increases the depth of penetration of the electrons into the section. When the PE energy is the highest at 5 kV, the PEs pass through the specimen without spreading significantly, suggesting that most PEs transmit the specimen without the interactions. The BSEs spread laterally, and thus the SE-II secondary electrons are generated far from the PE impact point, resulting in the loss of the spatial resolution. Thus the maximal compositional information could be obtained at the accelerating voltage of 2.2 kV. The image taken at

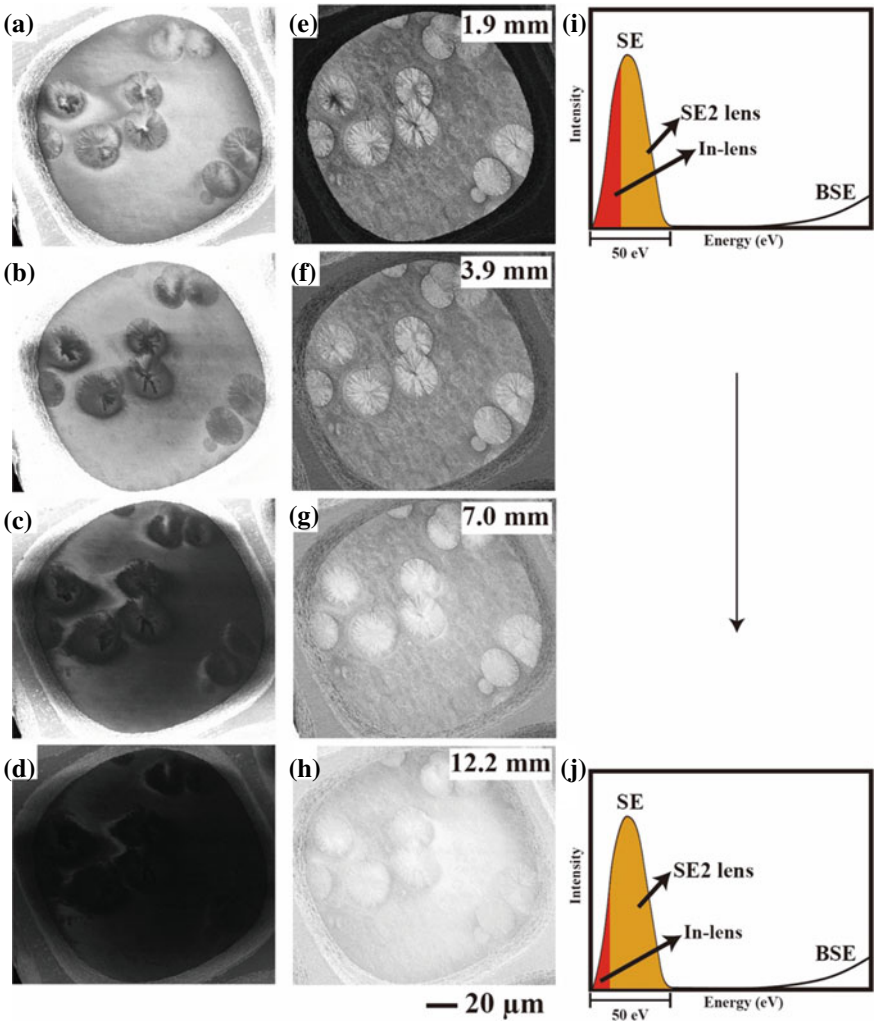

Fig. 62 Energy-filtered SE imaging of a semicrystalline PLA sections stained with RuO_4 with varied working distances: **a**–**d** in-lens images; **e**–**h** SE2 images; **i**, **g** schematic illustration depicting the distribution of SEs into the two detectors when the working distance is 1.9 and 12.2 mm, respectively

2.2 kV (Fig. 63c) resembles the image taken in TEM mode shown in Fig. 15. This means that this SE2 image mainly represents the internal structure of the section based on the difference in atomic composition and not on the surface topological features. The difference in the SE-II yield between RuO_4-stained and unstained areas is reflected in the contrast of the SE2 image shown in Fig. 63.

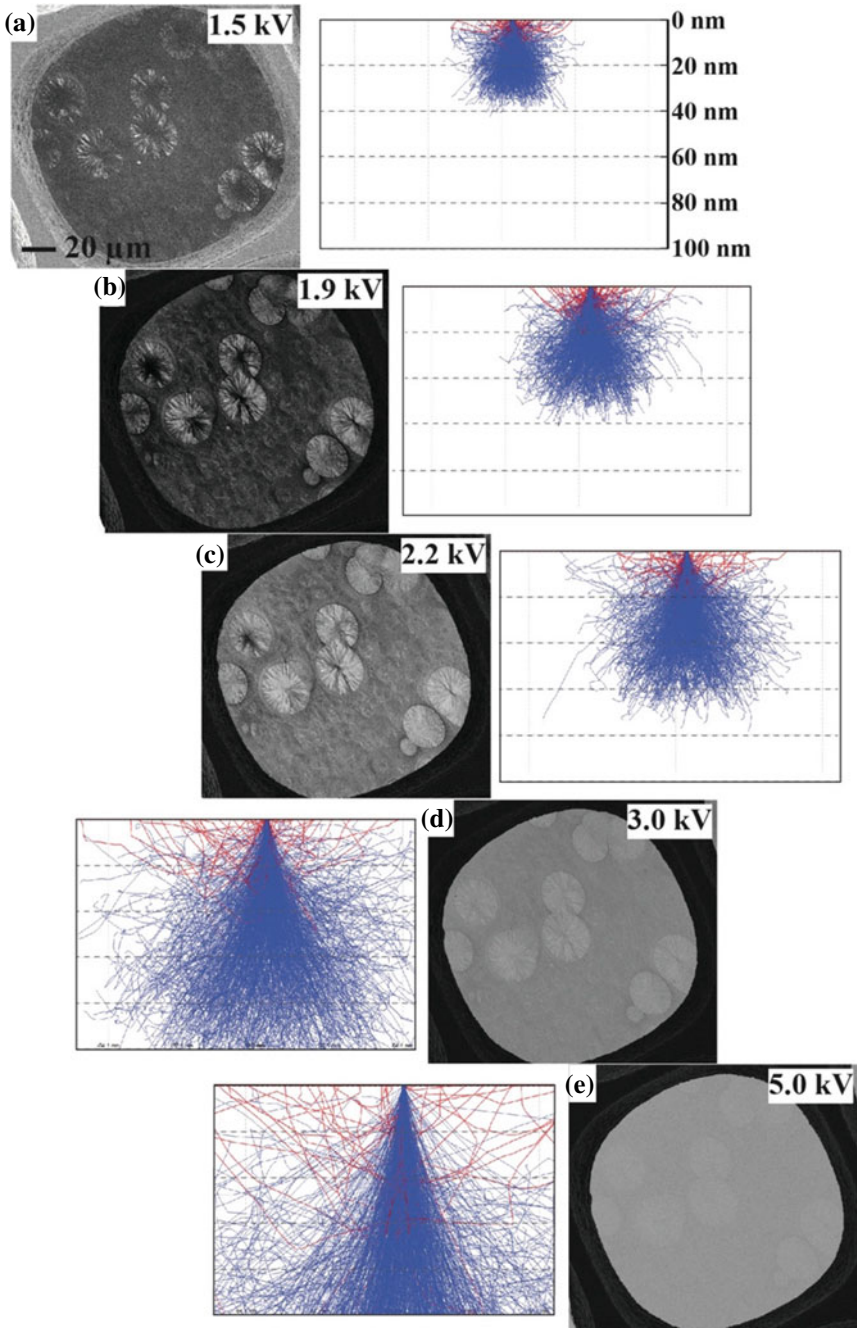

Fig. 63 Acceleration voltage dependence of the contrast in the SE2 images of the PLA thin section. Interaction volumes (blue) and BSEs paths (red) in a 100-nm-thick carbon sample created by Monte Carlo simulation

The conditions optimized for the SE imaging of the polymer thin section allow the acquisition of high-quality images of the structures developed within semicrystalline polymers that differ by as much as three orders of magnitude in structural scale, as shown in Fig. 64. One shows the global distribution of spherulites and their textures (Fig. 64a); the other is a high-resolution lamellar structure grown in the spherulites (Fig. 64b). Figure 64c, d shows the images showing the spherulites taken by the SEM and TEM, respectively. Even though the imaging principles are different, those two are similar. Figure 64a exhibits two types of spherulites with different sizes and appearances: One is large, with the typical spherulite texture found in common semicrystalline polymers, and the other is small, with an obscure but definite spherulite pattern, which is also present surrounding the large spherulites. In the former, lamellae are observed inside as shown in Fig. 64b, but not in the latter. We speculate that these two types of spherulites grow at different stages of the crystallization process. The former grows during annealing at a constant temperature in the mold for a certain period, and the latter produces during cooling to room temperature after removal from the mold. Thus, the latter may not have enough lamellae to be observable.

6.2 Correlative Raman Imaging and SEM

Correlative microscopy involves using multiple light or electron microscopy methods to analyze the same specimen area. One such technique is Correlative Raman Imaging and Scanning Electron (RISE) microscopy, which combines SEM and confocal Raman imaging. This correlative microscopy method links ultra-structural surface properties to molecular information. Confocal Raman imaging is a non-destructive spectroscopic method for analyzing molecular structures in a sample. The Raman effect is exhibited when light interacts with the chemical bonds in a material. This interaction causes a specific energy shift in the back-scattered light, which appears in a unique Raman spectrum that can be detected. By combining Raman spectroscopy with a confocal microscope, the confocal Raman imaging technique can detect and image the spatial distribution of chemical components within a sample. This technique can also analyze additional sample characteristics, such as the relative amount of a specific component, stress and strain states, or crystallinity.

RISE microscopy merges the benefits of two imaging methods into a single instrument. This enables the capture of detailed information about both the high-resolution surface structure and the molecular structures of the sample. The instrument automatically transfers and repositions the sample to alternate between the different measurement techniques. The results obtained from each method can be correlated and overlaid to produce composite images (Fig. 65) [125].

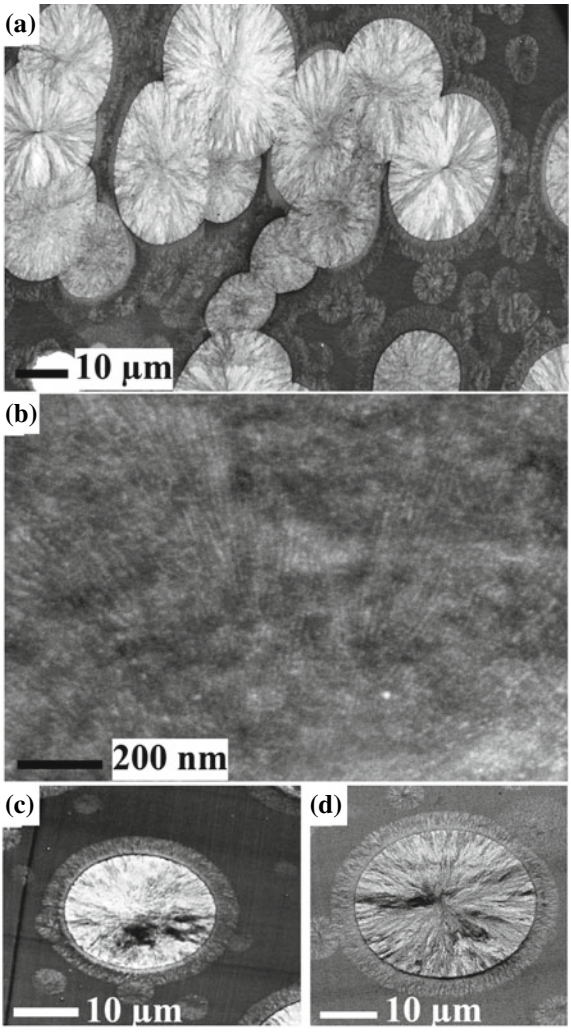

Fig. 64 SE2 image showing global spherulite distribution in the RuO_4-stained PLA thin section (**a**) and in-lens image showing the lamellae in the spherulite (**b**). **c**, **d** Are the spherulites in the PLA thin section taken by SE2 in SEM and by TEM, respectively

RISE microscopy was performed to investigate an interface formed by adhesive bonding of *i*PP and alkylborane (AB)-initiated acrylic adhesive. As described in Sect. 4 in "Interfacial Phenomena in Adhesion and Adhesive Bonding Investigated by Electron Microscopy" chapter, the bonding mechanism of the surface treatments of *i*PP was investigated. The acrylic adhesive using alkylborane as an initiator yields strong bonding to *i*PP through the chemical reaction between the acrylic monomer and the *i*PP, which produces the acrylate polymers grafted onto the *i*PP main chains at the interface. Figure 66a shows an STEM-BF image showing the interfacial region between the AB-initiated acrylic adhesive and *i*PP by the staining with RuO_4. The radical species produced by the oxidation of alkylborane preferentially attacks the

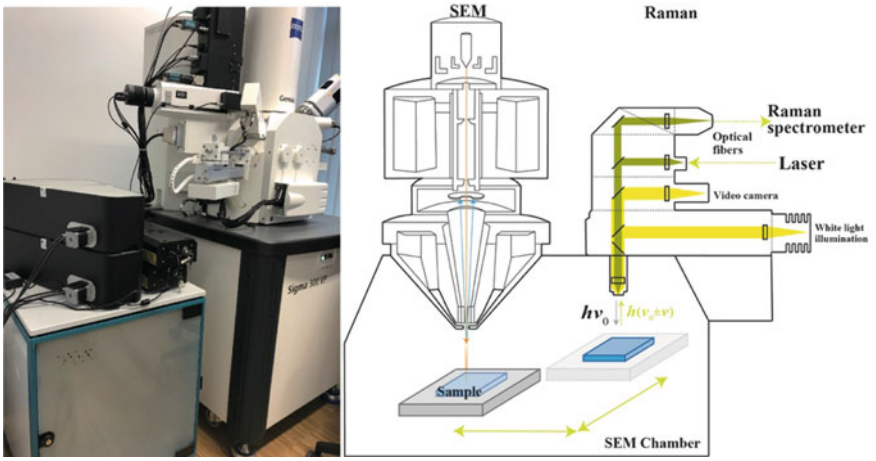

Fig. 65 The appearance of RISE microscope with a combination of SEM (ZEISS Sigma300) and Raman microscope system (WITec) (**a**) and the principle of its operation (**b**)

amorphous phase of alkylborane PP and initiates the polymerization of the acrylic monomers. The acrylate monomers erode the amorphous region of *i*PP and initiate graft polymerization onto the lamellae, disrupting the lamellar structure and etching the *i*PP surface. The micrograph shows the three regions: the left side (I) is the *i*PP substrate containing the dispersed rubber domains, the right side (III) is the adhesive layer including the stained small objects that are presumed to be the *i*PP eroded from the *i*PP surface owing to the highly reactive acrylic radicals, and the central part (II) is unknown to be produced as a result of the chemical reaction between *i*PP and the adhesive.

A smooth cross section was prepared by cryoultramicrotomy for analysis with the SEM-Raman system. The sample is first imaged with the SEM microscope to locate the region to be analyzed by the subsequent Raman imaging, as shown in Fig. 66b, showing the three regions as found by STEM. After the SEM measurement, the sample was automatically transferred and re-positioned for confocal Raman imaging within the vacuum chamber of the electron microscope. Then, 240 × 80 spectra were acquired for an area of 40 × 20 μm with a 532 nm, 14.534 mW laser. The acquisition time for one spectrum is 0.5 s. The spectra extracted from the *i*PP, the adhesive layer, and the rubber domains in the *i*PP are shown in Fig. 66d. Using these three spectra as standard spectra and the MLLS fitting was employed for the acquired individual spectra. By mapping the three components shown in Fig. 66c, region II can be known to be the co-existing layer of *i*PP (red) and adhesive (blue) with no rubber particles (yellow). The dispersed rubber particles of several hundred manometers can be identified only in the *i*PP substrate (Region I).

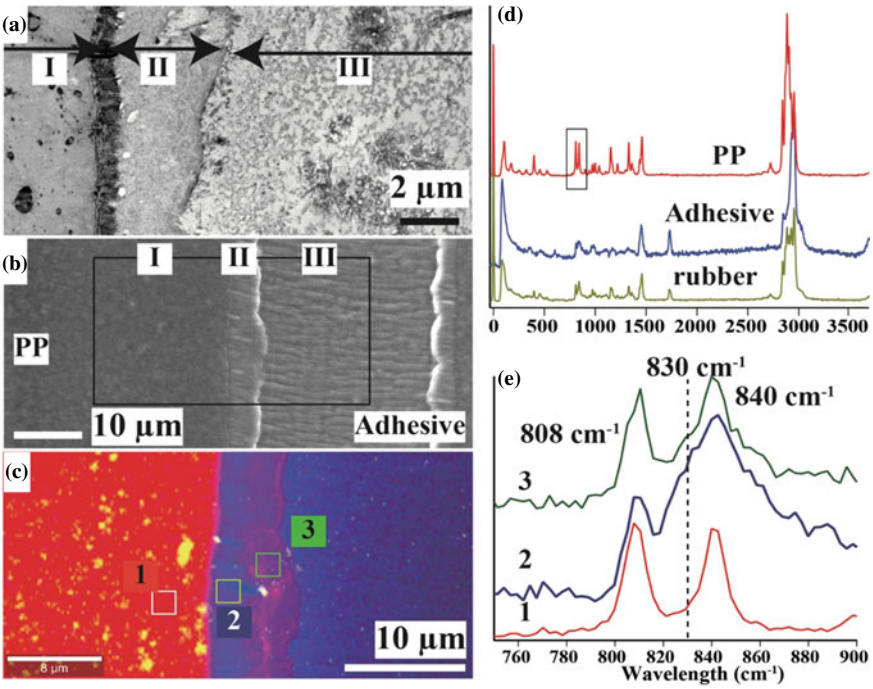

Fig. 66 RISE microscopy analysis of the interfacial region between *i*PP and the alkylborane-initiated acrylic adhesive: **a** STEM-BF image showing the interfacial region by the staining with RuO_4; **b** SEM image of the cross section of the interfacial region; **c** Raman image displaying the chemical maps *i*PP (red), adhesive (blue) and rubber (yellow); **d** The corresponding color-coded Raman spectra of the three components for the map; **e** The peaks in the Raman spectra in the region indicated in **d** representing the local crystallinity of *i*PP extracted from the ROIs shown in **c**. The data acquisition was supported by Dr. Ute Schmidt (WITec) and Dr. Fang Zhou (Carl Zeiss)

It is known that confocal Raman spectroscopy makes it possible to evaluate the local crystallinity of *i*PP using the peaks at 808 and 840 cm^{-1} assigned to helical chains and shorter chains within the crystalline phase, respectively, while the peak at 830 cm^{-1} assigned to non-helical amorphous phase [59, 126]. Figure 66e presents the peaks in the Raman spectra corresponding to the local crystallinity of *i*PP extracted from the ROIs indicated in Fig. 66c. The peak at 830 cm^{-1} can be identified as a shoulder of the peak at 840 cm^{-1} in the spectra extracted from ROI-2 and ROI-3. These results indicate that the interfacial chemical reaction between the acrylic monomer and *i*PP produced a thick interfacial layer, including *i*PP with low crystallinity, of which thickness was estimated to be ~5 µm. Through RISE microscopy, it is possible to link surface morphology with molecular information. This combination enables new possibilities in comprehensive interface characterization.

7 In Situ TEM

Studying bonding mechanisms and evaluating joint performance requires investigating the failure of interfaces. Optical or scanning electron microscopy has been used to speculate on failure behaviors of joint interfaces, but this classical fractography method has limitations in understanding complicated bonding mechanisms and properties [59, 127, 128]. Direct observation of failure behavior under high-resolution electron microscopy can provide information on complicated failure processes in joint interfaces. A new specimen holder has been developed to perform in situ tensile testing under TEM observation, allowing direct observation of interface failures. This microscopy technique has only been applied to observing deformation and microcrack propagation in metallic and ceramic bulk materials [129–131]. The failure of an adhesive interface between an aluminum alloy (Al5052) and an epoxy adhesive was investigated through the in situ tensile test using this new equipment, visualizing the different stages before the macroscopic failure of the interfaces. Figure 67 shows the specimen holder equipped with a device for the in situ tensile experiments manufactured by Mel-Build Corp. (Fukuoka, Japan). The specimen is mounted on an isolated thin metal cartridge (Fig. 67c). A small device for applying a tensile force to the specimen is built into the tip of the sample holder (Fig. 67a), as illustrated in Fig. 67b. Pushing the cartridge by the actuator with 100 nm/s can open the slit fabricated in the cartridge as shown in Fig. 67d, and tensile load can be applied into the specimen fixed on the slit. The sample used for the experiment is the Al bonded with an epoxy adhesive. 2-mm-thick Al5052 plates were preliminarily treated with sodium hydroxide aqueous solution (ph12) at 60 °C for 10 s and then with nitric acid for 10 s. Those two plates were bonded with an epoxy adhesive, comprising bisphenol-A epoxy and triethylenetetramine (TETA), by curing at 100 °C for 30 min. The in situ experiment used a thin section of 200 μm in length and width and 100 nm in thickness, containing a pre-crack at one end in the center of the specimen. The thin section was cut with a diamond knife by ultramicrotomy. Figure 67e shows an STEM-HAADF image of the slit part, where the specimen is fixed on the slit with the interface aligned parallel to the longitudinal direction of the slit with a width of 20 μm. The mounting of the thin sections floating on water onto the slit of the cartridge is demonstrated in Fig. 68.

Figure 69 displays STEM-HAADF images demonstrating failure at the Al/epoxy adhesive interface. Figure 70 provides a schematic illustration depicting the observed failure behavior of the epoxy/Al adhesive interface under an in situ tensile experiment conducted under STEM observation. The initial pre-crack is visible in Fig. 69a, b through d presents high-magnification images of the early stages of crack initiation. Figure 69e–g shows the zoomed images of Fig. 69b–d, respectively. The damaged zone was found to occur before crack generation at the pre-crack tip in the epoxy side near the interface, which then transformed into a crack and grew toward the Al surface, as seen in Fig. 69f. Once the crack reached the Al surface, it propagated along the interface, resulting in failure. A small amount of adhesive remained on the Al surface after failure, as shown in Fig. 69g. Micro-voids ahead of the crack were also

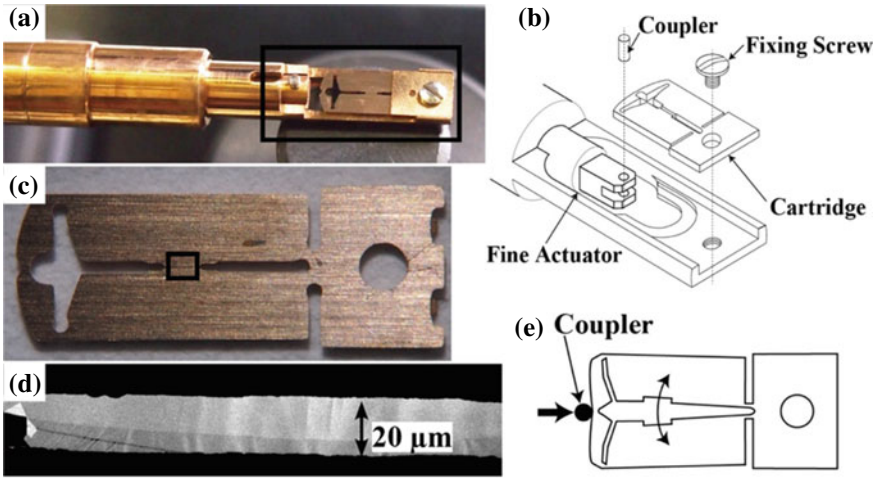

Fig. 67 Nano-order tensile specimen holder for STEM: **a** head part of the specimen holder; **b** illustration of the tensile loading device indicated in **a**; **c** specimen cartridge connected to the fine actuator built in the holder device; **d** illustration representing the deformation of the cartridge to widen the slit by pushing with the coupler; **e** STEM-HAADF image showing the thin section fixed on the slit of the cartridge. Reprinted with permission from Ref. [132]. Copyright 2021, Elsevier. All Rights Reserved

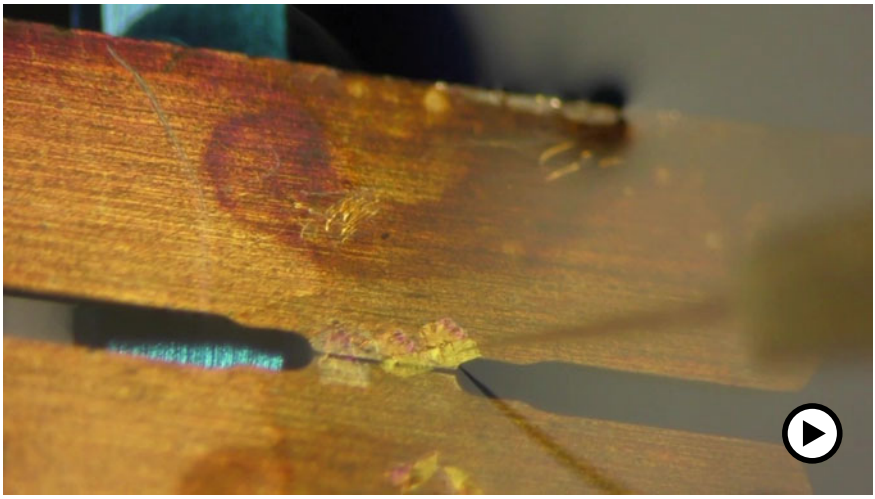

Fig. 68 Video demonstrating the placement of the thin sections on the slit of the cartridge (► https://doi.org/10.1007/000-ayg)

produced before crack propagation, as shown in Fig. 69c. The failure process from crack generation to propagation and the final interface failure is displayed in the video in Fig. 71. In Sect. 7 of "Interfacial Phenomena in Adhesion and Adhesive Bonding Investigated by Electron Microscopy" chapter, it is described that the in situ straining in STEM allowed for the dynamic observation of the failure process, including plastic deformation preceding crack initiation, crazing in polymer, micro-voids ahead of the crack, and crack propagation along interfaces [132].

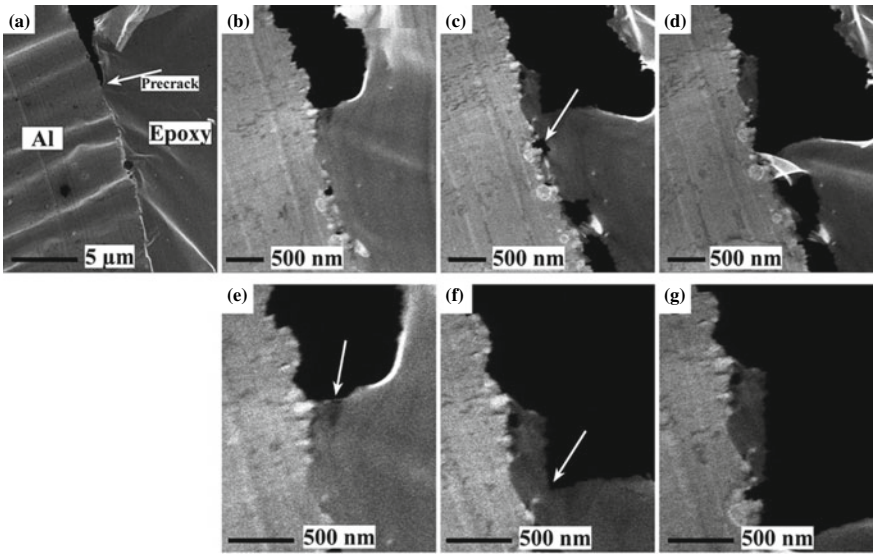

Fig. 69 STEM-HAADF images of the in situ observation of the crack propagation of Al5052/epoxy adhesive interface under tensile loading. The left and the right sides correspond to the Al and adhesive, respectively: **a** shows the interface with pre-crack before applying tensile load. **b–d** Show the failure process at the crack tip. **e–g** Are the high-magnification views of **b–d**, respectively. Reprinted with permission from Ref. [132] Copyright 2021, Elsevier. All Rights Reserved

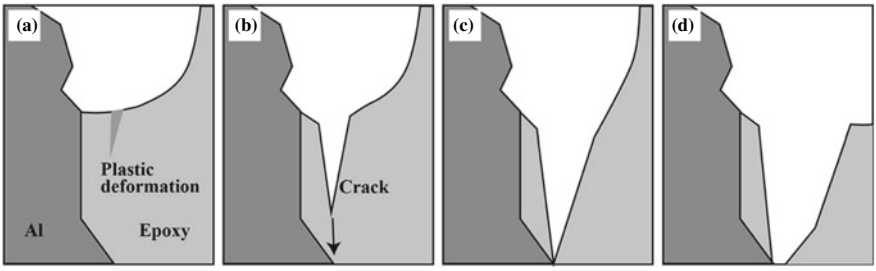

Fig. 70 Schematic illustration presenting the failure behavior of the epoxy/Al adhesive interface as was observed by in situ tensile experiment under the STEM observation

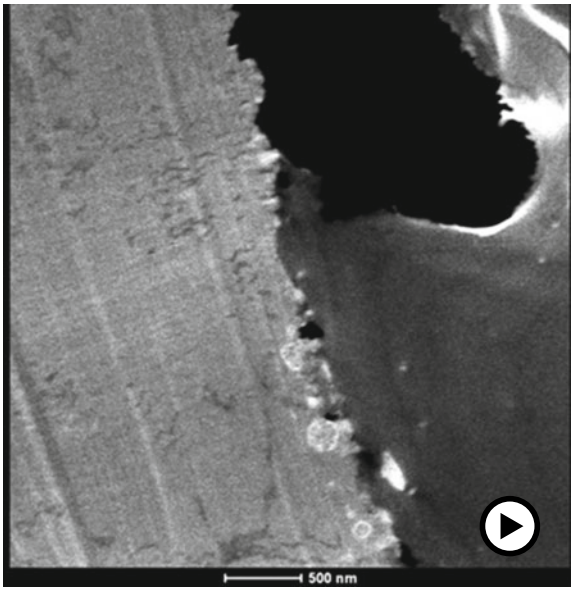

Fig. 71 Video presenting the in situ tensile experiment under STEM observation exhibiting the failure of the interface between Al6061 and an epoxy adhesive (► https://doi.org/10.1007/000-ayh)

8 Specimen Damages by Electron Beam Irradiation

Electron beam irradiation poses a significant challenge for investigating polymers, which are highly sensitive to it due to their organic nature. The literature has extensively discussed the effects of irradiation on polymers, with many papers and reviews dedicated to the topic [133]. The primary damage process is inelastic scattering, which results in molecular excitation or ionization. This energy dissipation can produce molecular vibrations (heat) or cause bond scission, such as hydrogen loss and forming radicals. Secondary effects include chain scission or cross-linking, mass loss, reduced crystallinity, and heat generation. The imaging of soft materials has spatial resolution limitations due to radiation damage to the specimens. Unlike the TEM studies of inorganic materials, where the spatial resolution is primarily limited by electron optics, soft-material imaging's resolution limit depends on the total electron dose they can withstand before undergoing structural changes.

The scission of carbon chains and side units can inflict significant damage on polymer specimens, forming low molecular weight molecules and radicals. Aliphatic chains are more prone to C–H bond breakage than aromatic compounds that can dissipate energy through the π-electron system of benzene rings. The low molecular weight molecules and radicals can also lead to reactions with radicals, thermal diffusion, and evaporation of low atomic weight fragmented atoms and molecules like H_2, CH4, CO_2, and NH_3. The degradation of PMMA and PS under radiation has been extensively studied, and their degradation schemes have been proposed [134,

135]. PMMA undergoes main-chain scission and pendant unit removal, forming methyl and formyl radicals. Breakage of the main chain causes a decrease in molecular weight, and the low molecular weight PMMA terminal group can be either a C=C double bond or a tertiary radical. In contrast, PS undergoes cross-linking, with breakage of the phenyl ring [136].

Another problem that limits high-resolution imaging and analysis is the specimen contamination induced by electron beam irradiation. When a small specimen area is irradiated, the hydrocarbon molecules are highly prone to diffusion on the surface and subsequent cracking, ultimately leading to fixation by the electron beam. Here, our investigations associated with the specimen damages of polymers by electron beam irradiation are summarized.

8.1 Mass Loss in Polymer Thin Sections

The effect of electron beam irradiation on polymer specimens was studied by evaluating the changes in specimen thickness as a function of dose. The local thickness (t) of the specimen is estimated from an EELS spectrum using the formula:

$$t/\lambda = \ln (I_t/I_0), \tag{4}$$

where I_0 is the area under the zero-loss peak, I_t is the total area beneath the overall spectrum, and λ is the total mean free path for inelastic scattering [137]. Thin polymer films of polymethyl methacrylate (PMMA) and styrene-acrylonitrile random copolymer (SAN), with 40 and 50 nm thicknesses, respectively, were prepared by spin-coating on cleaved NaCl crystals from dilute solutions and transferred onto TEM meshes after lifting off with water. The relative thicknesses t/λ estimated from the EELS spectra are plotted against the radiation dose in Fig. 72 [72]. The films were measured by ellipsometry to determine their thicknesses. The figure indicates that the specimens with the same thickness irradiated at room temperature and 120 K exhibit quite different relative thicknesses. Their relative thicknesses were estimated from the EELS spectra. The results indicate that the PMMA and SAN films show lower relative thicknesses when irradiated at room temperature than at 120 K. The thicknesses of the films irradiated at room temperature remain almost constant with the increase in dose, while those irradiated at 120 K gradually decrease in thickness. This suggests that the degradation process causing a mass loss in the specimen is completed at a significantly lower dose at room temperature, whereas cooling the specimen retards the degradation process. The results also show that PMMA tends to degrade much faster than SAN.

The study suggests that cryogenic conditions effectively retard radiation damage but cannot prevent the damage completely. This experiment shows that electron beam irradiation should be minimized, even in cryogenic conditions, to avoid the damaging effect on polymer specimens.

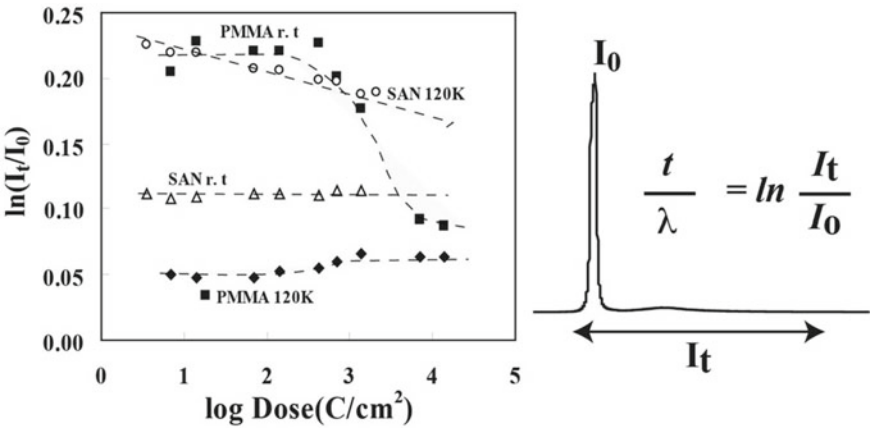

Fig. 72 The plot of the relative thicknesses of PMMA and SAN films versus the irradiation dose at room temperature and 120 K. Reprinted with permission from Ref. [72]. Copyright 2005, John Wiley & Sons. All Rights Reserved

Cooling the specimen results in a cage or frozen-in effect, which is the most effective way of reducing secondary processes at low temperatures. In some instances, cooling can increase the likelihood of scission products recombining or cross-linking before leaving the specimen. Nonetheless, primary processes remain unaffected by temperature and cannot be prevented by cooling the specimen.

8.2 Chemical Damages of Polymers Evaluated by ELNES

As mentioned in Sect. 5.2, the C K-edges of polymers contain ELNES that sensitively reflect chemical structures such as aromatic, carbonyl, ether, and methyl groups. Changes in the structure of molecules can be detected by their influence on the ELNES. O K-edges of the oxygen-containing polymers also exhibited the ELNES features that were sensitive to the polyester's chemical structures. The elimination of the particular peak in the O K-edge ELNES reflects the resistivity of the polymers against the dose of the electron beam, as shown in Fig. 39. To investigate chemical damage caused by electron beam irradiation in polymer specimens, C K-edge ELNES of several polymers was acquired under different acquisition conditions by varying the acquisition time and point-to-point distance in STEM-SI mode at 200 kV. Figure 73 displays the C K-edge ELNES of aromatic (left column) and non-aromatic (right column) polymers. The measurements were carried out in a cryogenic condition at 110 K with a beam size of 0.74 nm and a beam current of 0.293 nA. 10 × 10 spectra were acquired and summed up into one spectrum with the acquisition time for one spectrum of 100 ms. Therefore, the exhibited spectra are the average of 100 spectra. Two spectra are shown for each polymer acquired with long (black)

and short (red) point-to-point distances with an acquisition time of 100 ms for one spectrum.

The presence of oxygen in PET and PBT leads to an increase in the number of peaks when compared to saturated polyolefins. PBT and PET bond assignments can be carried out using previously reported EELS results [103]. When the point-to-point distance is 50 nm, the first and most prominent peak at 286 eV is assigned to the π* C=C transition in the phenyl ring. The second and third peaks at 289 ± 0.5 and 292 ± 0.5 eV, respectively, are assigned to the π* C=O transitions and the σ* C–O transition. The peak assigned to the π* C=O transition can also be detected as a broad shoulder in the poly(benzyl methacrylate) (PBzMA). The second and third peaks are eliminated when the point-to-point distance is decreased to 2 nm. A broad peak at around 287–288 eV is generated instead, indicating that the spectral acquisition at the narrow interval significantly caused chemical damage to the polymers. It is known that both chain scission and cross-linking occur when PET undergoes electron beam damage [138]. It has been said that intramolecular dehydrogenation occurs, leading to carbonyl group rearrangement.

PS contains a phenyl pendant group on every alternating carbon in the main hydrocarbon chain. The first peak at around 285 eV is a signature of π* transition in the phenyl group. According to the radiation damage mechanism shown in Scheme 3, PS undergoes cross-linking, which changes the environment of the main-chain C–C bonds. The damage effect can be seen in the spectral features associated with the first peak assigned to the π* C=C transition, which becomes broader and shifts to lower energy.

PC and PPO show the peak at 288.0 eV in addition to the intense peak at 286.0 eV assigned to the π* C=C transition in the phenyl ring, which is attributed to the σ* C–H transition in the methyl groups. This ELNES feature can be identified in the spectra taken with a 50 nm point-to-point distance. In contrast, with the narrow interval of 10 nm, the peak in PPO eliminates, suggesting that the methyl groups attached to the phenyl ring are lost due to the scission of the bonds. As observed in PS, the π* C=C transition at 286 eV becomes broader and shifts to lower energy in PPO. It is therefore suggested that the phenyl rings are cross-linked after removing the methyl groups. Polyphenylene sulfide (PPS) exhibits no peak elimination and shifts with minor changes in the peak heights by decreasing the spectral acquisition interval. Therefore, PPS is the highest resistivity against electron beam irradiation among the polymers evaluated in this study.

The C K-edge ENLESs of PMMA and poly(*tert*-butyl methacrylate) (P*t*BuMA) show similar features. The first peak at 285 is a characteristic of π* C=C transition. Since no such bond is present, this spectral feature implies degradation under the electron beam, as shown in Scheme 2. The second peak at 289.5 eV is a signature of the carbonyl group. For PMMA, we observed slight increases and decreases in the peak heights at 286 ± 0.5 and 289 ± 0.5 eV, respectively, and no dramatic changes due to the reduced acquisition intervals. In contrast, for P*t*BuMA, the peak at 286 eV is enlarged and the peak at 289.5 eV disappears. These results suggest that acquiring damage-free C K-edge ELNES for both methacrylate polymers is challenging.

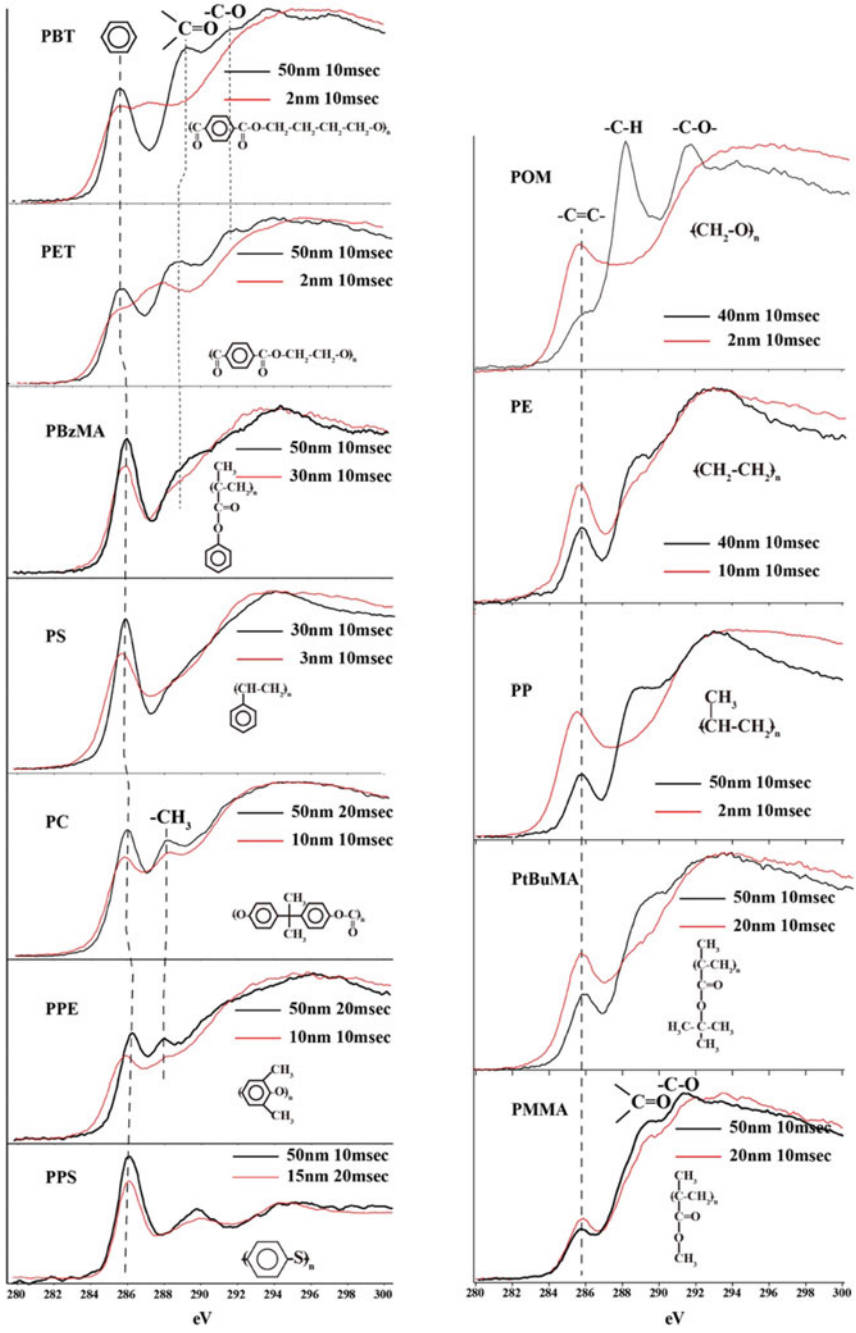

Fig. 73 C K-edge ELNESs of polymers taken by STEM-SI mode with two acquisition conditions. The black and red spectra were acquired with long and short point-to-point distances. The intensities are normalized at the maximum points

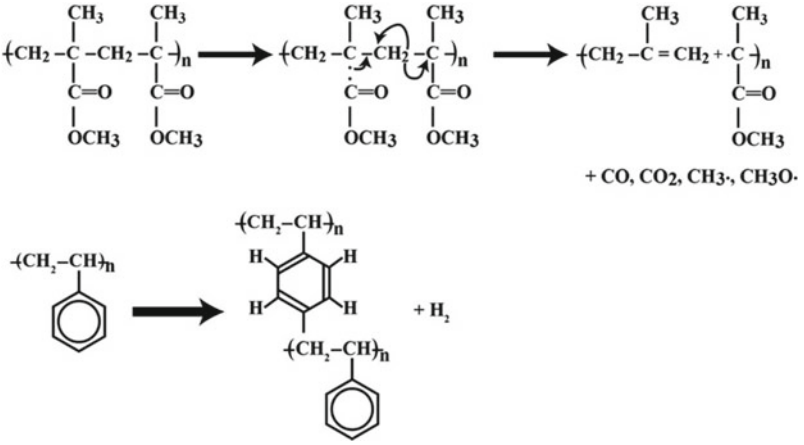

Scheme 3 The degradation processes of PMMA and PS under electron beam irradiation

Polyethylene and PP are fully saturated and therefore expected to display relatively simple C K-edges. These two polymers are structurally different due to a methyl group on every other carbon atom. EELS measurements of PE and PP reveal that the processed spectra can be decomposed into three peaks for each polymer. The first peak at 285.0 eV in both polymers corresponds to the π^* C=C transition. These unsaturated bonds are created due to electron beam damage during irradiation. The second peak at 288.5 $\pm$ 1 is attributed to the σ^* C−H transition. The third peak at 292.0 eV in both polymers is associated with the σ^* C−C transitions. Under beam irradiation, the second peak disappears and the height of the π^* C=C transition peak increases.

POM showed two distinct peaks at 288 and 291.5 eV when the point-to-point distance is 40 nm. These peaks can be assigned to σ^* C–H and σ^* C–C transitions, respectively, according to X-ray absorption spectroscopy (NEXAFS) of polyethylene oxide [139]. The characteristic peaks are unfortunately eliminated by the reduction of the acquisition interval to the spectra to 2 nm and only the peak of the π^* C=C transition at 286 eV can be seen as a result of the damage.

As discussed in Sect. 5.2, ELNES phase mapping in STEM-SI mode is a powerful technique for imaging polymer nanostructures. To improve the spatial resolution of the mapping, the acquisition of EEL spectra should be performed with a distance between points as small as possible. The results indicate that the ELNES features of the C K-edge are lost when the distance is less than 10 nm. Therefore, phase mapping using C K-edge ELNES in polymers is challenging.

8.3 Electron-Induced Contamination

The spatial resolution has limits in the imaging of soft materials, mainly due to radiation damage. Additionally, specimen contamination can cause a loss of resolution, which is especially pronounced when imaging soft materials. This contamination manifests as a carbonaceous layer deposited on the specimen surface due to electron bombardment. The contamination arises from the hydrocarbons present in the TEM chamber that react with the electron beam to form hydrocarbon ions that condense and form a carbon-rich, polymerized film on the irradiated area. Figure 74a shows contamination spots created on a thin carbon foil by an electron beam with an intensity of 5.6×10^4 el/nm s at an accelerating voltage of 200 kV. The thickness of the contamination spots can be estimated using EELS, as shown in Fig. 74b. As the irradiation period increased, the intensity of the zero-loss peak decreased, but the overall intensities in the energy-loss regions of the spectra increased. The thickness (D) of the contamination can be estimated using Eq. (4). The thickness of the contamination rises and reaches about 600 nm with 10 min of irradiation.

Hydrocarbons in a TEM chamber can come from various sources, such as vacuum pump oils, outgassing specimens, or poor vacuum practices. Even with ultra-high vacuum conditions, some sources of contamination can remain and cannot be easily removed. Carbon is a principal element in organic compounds, and utilizing carbon ionizations in ESI and EELS could result in higher data-collection efficiency.

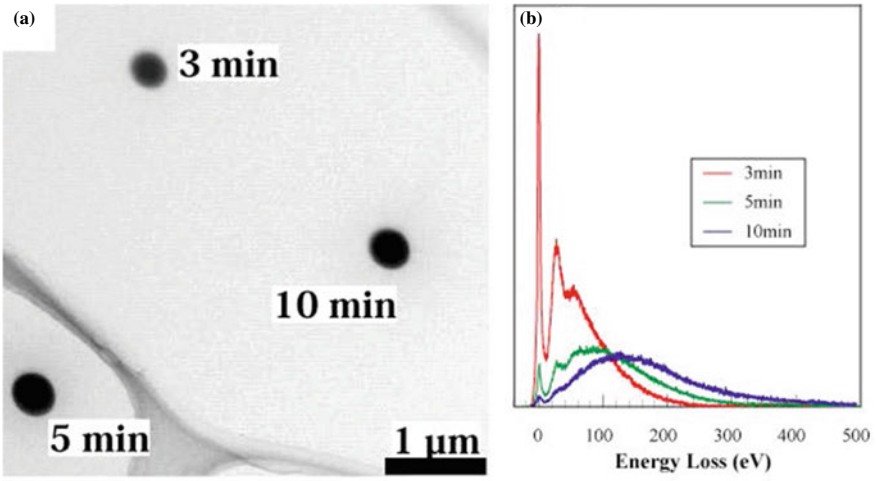

Fig. 74 The electron beam, with an intensity of 5.6 × 104 el/nm s, resulted in the production of beam-induced specimen contamination on a carbon thin foil through irradiation: **a** TEM micrograph showing the contamination spots created by irradiation for 3, 5, and 10 min; **b** EELS spectra acquired from the contamination spots. Reprinted with permission from Ref. [140] Copyright 2009, American Chemical Society. All Rights Reserved

However, the presence of specimen contamination leads to the formation of carbon-rich deposits in areas of interest, which disrupts carbon analysis and imaging of the specimen.

A process for cleaning the TEM chamber has been developed, utilizing activated oxygen radicals [140]. To achieve this, a low-temperature plasma generator (Evactron 45, XEI Scientific, Inc., USA) was installed on one of the accessory ports near the specimen chamber, as shown in Fig. 75a. The device produces oxygen radicals from the air, which can chemically etch the contaminants from the interior of a vacuum chamber [141]. The oxygen radicals oxidized hydrocarbons and other organic compounds, forming volatile oxides that can be easily pumped out of the TEM chamber. The plasma was confined within the generator chamber, preventing ion bombardment damage to the microscope. This device has also been used successfully to clean SEM. The oxygen radicals were carried by convection flow from the plasma into the specimen chamber and then toward the roughing pump. Although using a plasma generator to produce oxygen radicals could clean a TEM chamber's interior, it was ineffective in reducing beam-induced specimen contamination. This is because the narrow vacuum path of the TEM doesn't allow enough oxygen radicals to enter the chamber through the roughing pump alone. To overcome this limitation, an additional pumping system was installed at the objective aperture port (see Fig. 75b). This system created a viscous flow of oxygen radicals that reacted with hydrocarbons in the chamber atmosphere and surfaces. To clean the chamber, a high-frequency power of 10 Watts was applied to generate plasma using room air as the feed gas. The chamber was gently cleaned for 3 min, and then nitrogen gas was purged to flush out the reactant products. This cleaning/purging cycle was repeated 20 times while maintaining a pressure of 0.4 torr at the objective aperture port.

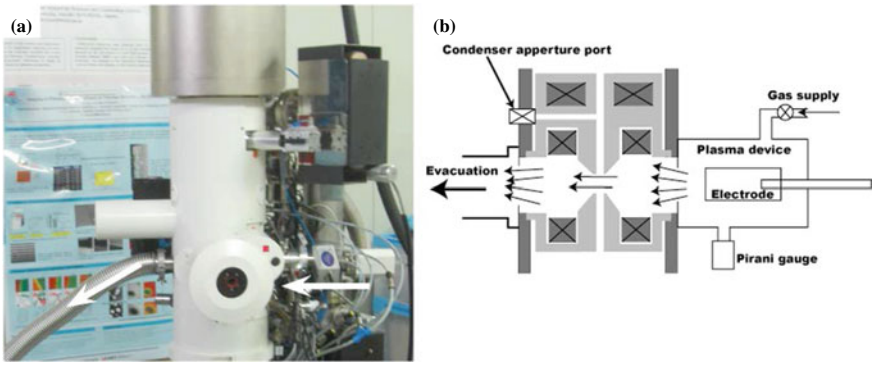

Fig. 75 Cleaning of a TEM chamber using a compact plasma generator: **a** A picture displaying the plasma generator installed on an accessory port near the specimen chamber. Arrows indicate the direction of the flow of activated oxygen radicals; **b** Schematic illustration shows the flow of activated oxygen radials in the TEM chamber. Reprinted with permission from Ref. [140] Copyright 2009, American Chemical Society. All Rights Reserved

After cleaning, we observed no signs of contamination even after exposing the electron beam for 30 min without using an anticontamination device. Figure 76 depicts contamination spots formed on a plasma-polymerized thin osmium tetroxide (OsO_4) film. Due to the carbon-rich nature of the contamination, the non-carbon supporting film presents the contamination as high-contrast areas. However, the contamination spots are thin and barely discernible in the zero-loss image (Fig. 76a). However, they can be slightly enhanced when viewed as an energy-filtered image at the 50 ± 10 eV energy loss (Fig. 76b).

Through gentle chemical cleaning of the specimen chamber with activated oxygen radicals, we can achieve a "contamination-free TEM". To demonstrate the benefits of this approach, we investigated the structure of a single polymer layer immobilized on the surface of a silica nanoparticle (SiNP), as depicted in Fig. 77. The surface initiator (2-bromo-2-methyl) propionyloxyhexyltriethoxysilane (BHE) was immobilized on the SiNP surface. Then poly(2-methacryloyloxyethyl phosphorylcholine) (PMPC) was grafted onto the BHE-immobilized SiNP using surface-initiated atom-transfer radical polymerization. The hydrodynamic radius of the PMPC-immobilized SiNP (PMPC-SiNP) in water was estimated at 48.1 nm using dynamic light scattering. The dimensions of the PMPC polymer chains immobilized on SiNP are much larger than those of the corresponding free polymer, indicating that the PMPC chains form a "polymer brush" where the radially oriented chains stretch perpendicularly against the silica surface [142]. We obtained a PMPC-SiNP distribution on an OsO_4 thin film, where only the SiNPs were visible.

Figure 78a, b exhibits images of a single PMPC-SiNP particle obtained by the ESI technique, capturing an individual particle with energy losses of 270 ± 10 and 315 ± 10 eV, respectively, corresponding to pre- and post-edge images for the carbon K-edge at 285 eV. The contrast change observed beyond the carbon K-edge indicates the presence of the PMPC brush layer surrounding the SiNP. Using "contamination-free TEM", it is possible to observe the polymer chains extending from the SiNP surface. Comparing the two images, it is apparent that the pre-edge image (Fig. 78a) shows only the silica particle. In contrast, the post-edge image (Fig. 78b) reveals the complete PMPC-SiNP structure. Figure 78c displays intensity profiles of the gray value measured along a horizontal line across the center of the SiNP. The pre-edge image's profile (green line) shows an SiNP diameter of around 20 nm, while the post-edge image's profile (red line) estimates the PMPC brush thickness at approximately

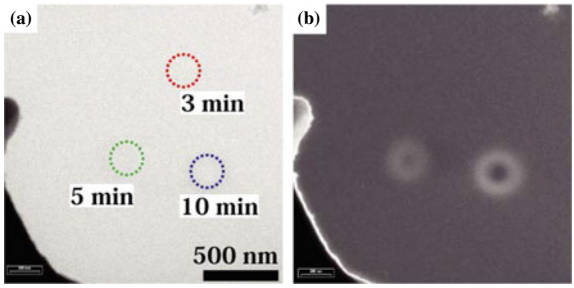

Fig. 76 Contamination marks produced on an OsO_4 thin film after cleaning recognized in zero-loss image (**a**) and energy-filtered image at 50 ± 10 eV (**b**). Reprinted with permission from Ref. [140]. Copyright 2009, American Chemical Society. All Rights Reserved

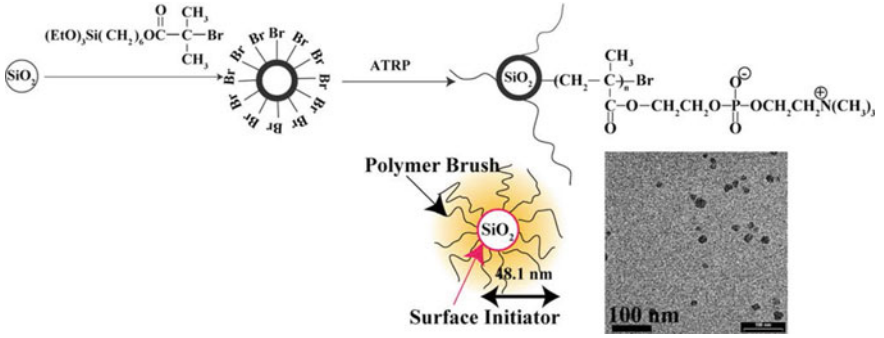

Fig. 77 Synthesis process of PMPC brushes on SiNPs, an illustration of the PMPC-SiNPs brush structure, and a global TEM image that displays the distribution of PMPC-SiNPs on an OsO_4 thin film. Reprinted with permission from Ref. [140]. Copyright 2009, American Chemical Society. All Rights Reserved

40 nm. The intensity profile from the post-edge image also shows two peaks at the SiNP edge, representing the bright ring surrounding the SiNP, which is believed to be the surface initiator (BHE) immobilized on the SiNP surface. Therefore, the surface initiator can be differentiated from the polymer brush layer, and its thickness can be estimated at approximately 5 nm.

The polymer brushes to modify inorganic surfaces have improved materials' dispersion, wetting, and adhesion properties, making them a promising method for industrial development. In the context of EFTEM analysis of polymers, carbon is more accessible to detect than other light elements due to its high concentration. As a result, images with a high signal-to-noise ratio can be obtained with lower electron doses compared to other elements. This suggests that EELS carbon analysis with

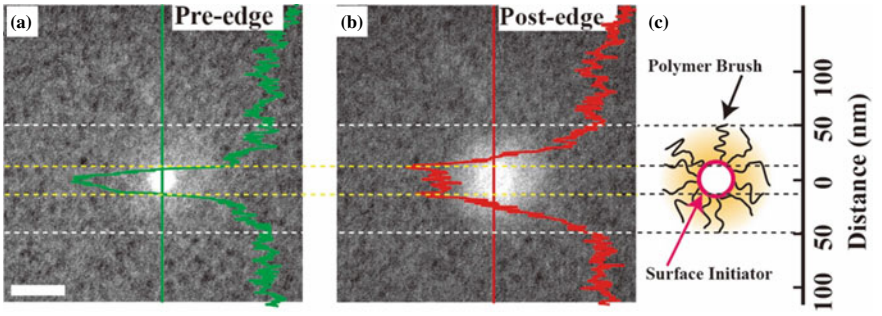

Fig. 78 The intensity profiles of pixels measured by taking horizontal lines across the center of the PMPC-SiNP in pre-edge (**a**) and post-edge (**b**) images. The red and green lines represent the profiles obtained from the respective images. An illustration depicting the hypothesized structure, featuring the initiator and polymer brush portions, is also provided (**c**). The scale bar corresponds to 50 nm. Reprinted with permission from Ref. [140]. Copyright 2009, American Chemical Society. All Rights Reserved

the high spatial resolution has the potential to advance the field of nano-analysis for soft materials. Additionally, contamination-free TEM can assist in various analytical techniques that require extended exposure times, such as electron tomography, EELS, and nanobeam diffraction.

9 Conclusions

This chapter provided an overview of electron microscopy techniques to investigate the interfaces present in polymeric materials and adhesive bonds. The basic components of EFTEM, STEM, and SEM instruments and EELS and EDX spectroscopy principles were explained. To perform the techniques, it is necessary to prepare artifact-free specimens. Ultramicrotomy is preferred for making thin sections of polymers and polymer/metal interfaces. The use of FIB should be limited to the samples that are difficult to cut by ultramicrotomy, such as composite materials containing large amounts of carbon fibers and inorganic fillers. Advanced electron microscopy techniques such as STEM-EDX tomography, ELNES phase mapping, energy-filtered SE imaging, and in situ tensile TEM were also introduced with the applications to the surface and interface characterizations of polymer alloys and composites, crystalline polymer, adhesive bonds, and metal substrates. Polymers are particularly sensitive to electron beam irradiation. This is a significant problem for polymer analysis by electron microscopy, especially for EELS. Scission of chemical bonds and cross-linking by electron beam irradiation cannot be avoided. It should be noted that imaging and analysis of polymers at high spatial resolution is limited due to structural changes upon electron beam irradiation rather than instrumental performance. In the next chapter, these electron microscopy techniques are used to discuss interfacial phenomena and mechanisms of adhesion and adhesive bonding.

Acknowledgements SH thanks Mr. Hideki Hakukawa, Ms. Yuri Shigemto, Dr. Takeshi Hanada, Dr. Kazunori Kawasaki, Dr. Yida Liu, Dr. Lingyun Lyu (AIST), Prof. Yongjin Li (Hangzhou Normal University), and Prof. Yonggui Liao (Huazhong University of Science and Technology) for their contribution to the works described in this chapter. Parts of the work were commissioned by JST-Mirai Program Grant Number JPMJMI18A2, Japan (Sects. 5.2, 7, and 8.3) and by the New Energy and Industrial Technology Development Organization (NEDO) Grant Numbers JPNP16010, Japan (Sects. 5.1.2 and 5.3.2) and JPNP20005, Japan (Sect. 5.5.3).

References

1. J. van den Brand, P.C. Snijders, W.G. Sloof, H. Terryn, J.H.W. de Wit, J. Phys. Chem. B **108**, 6017–6024 (2004)
2. S. Horiuchi, N. Terasaki, M. Itabashi, Manuf. Rev. **7**, 11 (2020)
3. K. Shimizu, C. Phanopoulos, R. Loenders, M.L. Abel, J.F. Watts, Sur. Interface Anal. **42**, 1432–1444 (2010)

4. M.L. Abel, J.F. Watts, Surf. Interface Anal. **41**, 508–516 (2009)
5. H. Téllez, J.M. Vadillo, J.J. Laserna, Rapid Commun. Mass Spectrom. **23**, 2357–2362 (2009)
6. T.N. Zittberg, J.D. Wolf, P.S. Wang, J. Mater. Sci. **23**, 1745–1747 (1988)
7. P.M.A. Sherwood, Surf. Sci. Spectra **5**, 1–3 (1998)
8. H. Dunlop, M. Benmalek, *J. Phys. IV* **7**, C6-163–C6-174 (1997)
9. M. Amstutz, M. Textor, Sur. Interface Anal. **19**, 595–600 (1992)
10. A. Kurian, S. Prasad, A. Dhinojwala, Langmuir **26**, 17804–17807 (2010)
11. T. Miyamae, H. Nozoye, Appl. Phys. Lett. **85**, 4373–4375 (2004)
12. J. van den Brand, O. Blajiev, P.C.J. Beentjes, H. Terryn, J.H.W. de Wit, Langmuir **20**, 6318–6326 (2004)
13. P. Taheri, J.R. Flores, F. Hannour, J.H.W. de Wit, H. Terryn, J.M.C. Mol, J. Phys. Chem. C **117**, 3374–3382 (2013)
14. B. Salgin, O. Özkanat, J.M.C. Mol, H. Terryn, M. Rohwerder, J. Phys. Chem. C **117**, 4480–4487 (2013)
15. R.J. Composto, E.J. Kramer, J. Mater. Sci. **26**, 2815–2822 (1991)
16. E.L. Jablonski, R.E. Gorga, B. Narasimhan, Polymer **44**, 729–741 (2003)
17. T.P. Lodge, Phys. Rev. Lett. **83**, 3218–3221 (1999)
18. P.F. Nealey, R.E. Cohen, A.S. Argon, Macromolecules **26**, 1287–1292 (1993)
19. R.J. Composto, E.J. Kramer, Macromolecules **25**, 4167–4174 (1992)
20. E. Kim, W.C. Wu, P.D. Garrett, Polymer **35**, 5706–5715 (1994)
21. E. Kim, E.J. Kramer, J.O. Osby, Macromolecules **28**, 1979–1989 (1995)
22. R.J. Composto, E.J. Kramer, Polymer **31**, 2320–2328 (1990)
23. P.F. Green, B.L. Doyle, Macromolecules **20**, 2471–2474 (1987)
24. N.C. Stoffel, C.A. Dai, E.J. Kramer, T.P. Russell, V. Deline, W. Volksen, W. Wu, S. Satija, Macromolecules **29**, 6880–6891 (1996)
25. M. Sferrazza, C. Xiao, R.A.L. Jones, D.G. Bucknall, J. Webster, J. Penfold, Phys. Rev. Lett. **78**, 3693–3696 (1997)
26. D.G. Bucknall, S.A. Butler, J.S. Higgins, Macromolecules **32**, 5453–5456 (1999)
27. B.B. Sauer, D.J. Walsh, Macromolecules **24**, 5948–5955 (1991)
28. J. Klein, Science **250**, 640–646 (1990)
29. T.E. Shearmur, A.S. Clough, D.W. Drew, M.G.D. van der Grinten, R.A.L. Jones, Macromolecules **29**, 7269–7275 (1996)
30. T.E. Shearmur, A.S. Clough, D.W. Drew, M.G.D. van der Grinten, R.A.L. Jones, Phys. Rev. E **55**, R3840-3843 (1997)
31. N. Clarke, F.R. Colley, S.A. Collins, L.R. Hutchings, R.L. Thompson, Macromolecules **39**, 1290–1296 (2006)
32. H. Qiu, M. Bousmina, Macromolecules **33**, 6588–6594 (2000)
33. M. Bousmina, H. Qiu, M. Grmela, J.E. Klemberg-Sapieha, Macromolecules **31**, 8273–8280 (1998)
34. S.E. Harton, T. Koga, F.A. Stevie, T. Araki, H. Ade, Macromolecules **38**, 10511–10515 (2005)
35. S. Hüttenbach, M. Stamm, G. Reiter, M. Foster, Langmuir **7**, 2438–2442 (1991)
36. G.A. O'Neil, J.M. Torkelson, Macromolecules **30**, 5560–5562 (1997)
37. J.P.S. Farinha, O. Vorobyova, M.A. Winnik, Macromolecules **33**, 5863–5873 (2000)
38. A. Ohshima, A. Yamagata, T. Sato, A. Teramoto, Macromolecules **32**, 8645–8654 (1999)
39. G. Dlubek, J. Pionteck, V. Bondarenko, G. Pompe, C. Taesler, K. Petters, R. Krause-Rehberg, Macromolecules **35**, 6313–6323 (2002)
40. S. Wang, E.D. von Meerwall, S.Q. Wang, A. Halasa, W.-L. Hsu, J.P. Zhou, R.P. Quirk, Macromolecules **37**, 1641–1651 (2004)
41. K.E. Price, S.J. Broadwater, A.R. Bogdan, I. Keresztes, J.L. Steinbacher, D.T. McQuade, Macromolecules **39**, 7681–7685 (2006)
42. L. Reimer (ed.), *Energy-Filtering Transmission Electron Microscopy* (Springer, Berlin, 1995), pp. 347–400
43. R. Brydson, *Electron Energy Loss Spectroscopy* (Taylor and Francis, London and New York, 2006), pp. 39–58

44. M. Kociak, O. Stéphan, M.G. Wall, M. Ténce, C. Colliex, in *Scanning Transmission Electron Microscopy, Imaging and Analysis*, ed. by S.J. Pennycook, P.D. Nellist (Springer, 2011), pp. 163–206
45. R. Pal, A.K. Sikder, K. Saito, A.M. Funston, J.R. Bellare, Polym. Chem. **8**, 6927–6937 (2017)
46. F. Hofer, P. Warbichler, in *Transmission Electron Energy Loss Spectroscopy in Material Science and the EELS ATLAS*, 2nd edn, ed. by C. Ahn (Wiley-VCH, Weinheim, 2004), p. 159
47. R. Brydson, *Electron Energy Loss Spectroscopy* (Taylor and Francis, London and New York, 2001), pp. 79–96
48. S. Horiuchi, Y. Liu, T. Hanada, A. Akiyama, Appl. Surf. Sci. **599**, 153964 (2022)
49. R. Leapman, in *Transmission Electron Energy Loss Spectrometry in Materials Science and the EELS ATLAS*, ed. by C.C. Ahn (Wiley-VCH, Weinheim, Germany, 2004), pp. 49–96
50. L.C. Sawyer, D.T. Grubb, G.F. Meyers, *Polymer Microscopy*, 3nd edn. (Chapman and Hall, London, 2008), pp. 146–160
51. G.H. Michler, *Electron Microscopy of Polymers* (Springer, Berlin, 2008), pp. 199–217
52. L.C. Sawyer, D.T. Grubb, G.F. Meyers, *Polymer Microscopy*, 3nd edn. (Chapman and Hall, London, 2008), pp. 160–180
53. J.S. Trent, J.I. Scheinbeim, P.R. Couchman, Macromolecules **16**, 589–598 (1983)
54. S. Horiuchi, N. Matchariyakul, K. Yase, T. Kitano, Macromolecules **30**, 3664–3670 (1997)
55. L.A. Giannuzzi, F.A. Stevie (eds.), *Introduction to Focused Ion Beams* (Springer, Berlin, 2005)
56. N.J. Severs, Nat. Protoc. **2**, 547–576 (2007)
57. J.A. Zasadzinski, J. Schneir. J. Gurley, V. Elings, P.K. Hansma, Science **239**, 1013–1015 (1988)
58. A. Igarashi, T. Terasawa, M. Kanie, T. Yamanobe, T. Komoto, Polym. J. **37**, 522–528 (2005)
59. Y. Liu, Y. Shigemoto, T. Hanada, T. Miyamae, K. Kawasaki, S. Horiuchi, A.C.S. Appl, Mater. Interfaces **13**, 11497–11506 (2021)
60. R. Brydson, *Electron Energy Loss Spectroscopy* (Taylor and Francis, London and New York, 2001), p. 46
61. L. Reimer, in *Energy-Filtering Transmission Electron Microscopy*, 1st edn, ed. by L. Reimer (Springer, Berlin, 1995), p. 383
62. R. Brydson, *Electron Energy Loss Spectroscopy* (Taylor and Francis, London and New York, 2001), pp. 101–109
63. K.H. Körtje, Scanning Microsc. **8**, 22 (1994)
64. S. Abolhas Sani-Dadras, G.H. Vàzquez-Nin, O.M. Echeverría, S. Fakan, J. Microsc. **183**, 215–222 (1996)
65. P.J. Thomas, P.A. Midgley, Ultramicroscopy **88**, 179–186 (2001)
66. S. Horiuchi, T. Hamanaka, T. Aoki, T. Miyakawa, R. Narita, H. Wakabayashi, J. Electron. Microsc. **52**, 255–266 (2003)
67. S. Horiuchi, T. Fujita, T. Hayakawa, Y. Nakao, Langmuir **19**, 2963–2973 (2003)
68. S. Horiuchi, T. Hayakawa, Angew. Chem. Int. Ed. **42**, 2285–2289 (2003)
69. M.R. Krejsa, J.L. Koenig, in *Rubber Technology Handbook*, ed. by N.P. Cheremisnoff (CRC Press, Boca Raton, Florida, 1993), p. 476
70. S. Horiuchi, H. Dohi, Langmuir **22**, 4607–4614 (2006)
71. H. Dohi, S. Horiuchi, Polymer **48**, 2526–2530 (2007)
72. S. Horiuchi, D. Yin, T. Ougizawa, Macromol. Chem. Phys. **206**, 725–731 (2005)
73. S. Goossens, B. Goderis, G. Groeninckx, Macromolecules **39**, 2953–2963 (2006)
74. G.A. Buxton, N. Clarke, Macromolecules **38**, 8929–8938 (2005)
75. J.B. Nephew, T.C. Nihei, S.A. Carter, Phys. Rev. Lett. **80**, 3276–3279 (1998)
76. Q. Tran-Cong, A. Harada, Phys. Rev. Lett. **76**, 1162–1165 (1996)
77. H. Furukawa, J. Phys. Soc. Jpn. **63**, 3744–3750 (1994)
78. A. Harada, Q. Tran-Cong, Macromolecules **30**, 1643–1650 (1997)
79. K. Kimura, H. Inoue, S.I. Kohama, Y. Yamashita, Y. Sakaguchi, Macromolecules **36**, 7721–7729 (2003)
80. E. Girard-Reydet, J.P. Pascault, Macromolecules **33**, 3084–3091 (2000)

81. W. Li, A.J. Ryan, I.K. Meier, Macromolecules **35**, 5034–5042 (2002)
82. V. Rebizant, A.S. Venet, F. Tournilhac, E. Girard-Reydet, C. Navarro, J.P. Pascault, L. Leibler, Macromolecules **37**, 8017–8027 (2004)
83. S. Swier, B. Van Mele, Macromolecules **36**, 4424–4435 (2003)
84. Y. Ishii, A.J. Ryan, Macromolecules **33**, 158–166 (2000)
85. R.W. Venderbosch, H.E.H. Meijer, P.J. Lemstra, Polymer **35**, 4349–4357 (1994)
86. J. Nunoshige, Y. Shibasaki, M. Ueda, Chem. Lett. **36**, 238–239 (2007)
87. Y. Liao, S. Horiuchi, J. Nunoshige, H. Akahoshi, M. Ueda, Polymer **48**, 3749–3758 (2007)
88. A.E. Coode, A.E. Porter, M.M. Klosowski, M.P. Ryan, S. Heutz, D.W. McComb, Curr. Opin. Solid State Mater. Sci. **21**, 55–67 (2017)
89. W. Dong, H. Hakukawa, N. Yamahira, Y. Li, S. Horiuchi, ACS Appl. Polym. Mater. **1**, 815–824 (2019)
90. Y. Liu, A.L. Hamon, P. Haghi-Ashtiani, T. Reiss, B. Fan, D. He, J. Bai, A.C.S. Appl, Mater. Interfaces **8**, 34151–34158 (2016)
91. J. Bertho, V. Stolojan, M.L. Able, J.F. Watts, Micron **41**, 130–134 (2010)
92. G. Radtke, G.A. Botton, in *Scanning Transmission Electron Microscopy: Imaging and Analysis*, ed. by S.J. Pennycook, P.D. Nellist (Springer, Berlin, 2011), pp. 207–245
93. R. Arenal, F. de la Peña, O. Stéphan, M. Walls, M. Tencé, A. Loiseau, C. Colliex, Ultramicroscopy **109**, 32–38 (2008)
94. J. Scott, P.J. Thomas, M. MacKenzie, S. McFadzean, J. Wilbrink, A.J. Craven, W.A.P. Nicholson, Ultramicroscopy **108**, 1586–1594 (2008)
95. J. Bodynko, I. Maclaren, A.J. Craven, Ultramicroscopy **149**, 9–20 (2015)
96. F. Voisard, N. Brodusch, M.L. Trudeau, H. Demers, K. Zaghib, R. Gauvin, Microsc. Microanal. **24**, 464–465 (2018)
97. D.R. Paul, J.W. Barlow, H. Keskkula, in *Encyclopedia of Polymer Science and Engineering*, vol. 1, 2, 2nd edn., ed. by J.I. Kroschwitz (Wiley, New York, 1988)
98. W. Baker, C. Scott, G.H. Hu, *Reactive Polymer Blending* (Hanser Publisher, Munich, 2001), pp. 1–279
99. S. Wu, H.-K. Chung, *J. Polym. Sci. Polym. Phys.* **24**, 148–169 (1986)
100. Z. Fu, H. Wang, X. Zhao, S. Horiuchi, Y. Li, Polymer **132**, 353–361 (2017)
101. U. Sundararaj, C.W. Macosko, Macromolecules **28**, 2647–2657 (1995)
102. B. Schaffer, L. Spillane, P.J. Thomas, Microsc. Microanal. **25**, 648–649 (2019)
103. R. Pal, L. Bourgeois, M. Weyland, A.K. Sikder, K. Saito, A.K. Funstron, J.R. Bellare, ACS Omega **6**, 23934–23942 (2021)
104. J. Frank, *Electron Tomography* (Springer, New York, 2006)
105. P. Ercius, O. Alaidi, M.J. Rames, Adv. Mater. **27**, 5638–5663 (2015)
106. H. Jinnai, Y. Shinbori, T. Kitaoka, Macromolecules **40**, 6758–6764 (2007)
107. M. Weyland, P.A. Midgley, Mater. Today **7**, 32–40 (2004)
108. R.D.J. De, A. Klug, Nature **217**, 130–134 (1968)
109. R.G. Hart, Science **159**, 1464–1467 (1968)
110. P.A. Midgley, R.E. Dunin-Borkowski, Nat. Mater. **8**, 271–280 (2009)
111. R. Brydson, *Electron Energy Loss Spectroscopy* (Taylor & Francis, London & New York, 2001), p. 60
112. P.A. Midgley, M. Weyland, Ultramicroscopy **96**, 413–431 (2003)
113. G. Möbus, R.C. Doole, B.J. Inkson, Ultramicroscopy **96**, 433–451 (2003)
114. S.M. Collins, P.A. Midgley, Ultramicroscopy **180**, 133–141 (2017)
115. T.J.A. Slater, A. Janssen, P.H.C. Camargo, M.G. Burke, N.J. Zaluzec, S.J. Haigh, Ultramicroscopy **162**, 61–73 (2016)
116. P. Burdet, Z. Saghi, A.N. Filippin, A. Borras, P.A. Midgley, Ultramicroscopy **160**, 118–129 (2016)
117. L. Lyu, T. Hanada, N. Yamahira, J. Morita, R. Yamamoto, K. Itomi, T. Adachi, S. Kubouchi, S. Horiuchi, J. Appl. Polym. Sci. **138**, e51443 (2021). https://doi.org/10.1002/app.51443
118. H. Hoeft, P. Schwaab, X-Ray Spectrom. **17**, 201–208 (1988)

119. R. Sundar, P. Ganesh, R.K. Gupta, G. Ragvendra, B.K. Pant, V. Kain, K. Ranganathan, R. Kaul, K.S. Bindra, *Lasers Manuf. Mater. Process.* **6**, 421–463 (2019)
120. A. Fukuda, H. Matsukawa, H. Goto, M. Suzuki, M. Nakamoto, R. Matsumoto, H. Utsunomiya, T. Tanaka, Mater. Trans. **56**, 1852–1856 (2015)
121. P. Ganesh, R. Sundar, H. Kumar, R. Kaul, K. Ranganathan, P. Hedaoo, P. Tiwari, L.M. Kukreja, S.M. Oak, S. Dasari, G. Raghavendra, Opt. Laser. Eng. **50**, 678–686 (2012)
122. L. Reimer, *Scanning Electron Microscopy*, 2nd edn. (Springer, Berlin, 1998), p. 164
123. K. Kumagai, T. Sekiguchi, Ultramicroscopy **109**, 368–372 (2009)
124. R. Rasch, A. Stricher, R.W. Truss, J. Appl. Polym. Sci. **131**, 39572 (2014)
125. O. Hollricher, U. Schmidt, S. Breuninger, Microsc. Today **22**, 36–39 (2014)
126. U. Schmidt, J. Muller, J. Koenen, *Confocal Raman Microscopy*, 2nd edn., ed. by J. Toporski, T. Dieing, O. Hooricher (Springer, Berlin, 2011), pp. 487–492
127. S. Horiuchi, A. Nakagawa, Y. Liao, Macromolecules **41**, 8063–8071 (2008)
128. S. Horiuchi, H. Hakukawa, Y.J. Kim, H. Nagata, H. Sugimura, Polym. J. **48**, 473–479 (2016)
129. Y. Wang, Z. Guo, R. Ma, G. Hao, Y. Zhang, J. Lin, M. Sui, Prog. Nat. Sci. **24**, 121–127 (2014)
130. Z.Q. Feng, Y.Q. Yang, Y.X. Chen, B. Huang, M.S. Fu, M.H. Li, J.G. Ru, Mater. Sci. Eng. A **586**, 259–266 (2013)
131. A. Nie, H. Wang, Mater. Lett. **65**, 3380–3383 (2011)
132. S. Horiuchi, Y. Liu, Y. Shigemoto, T. Hanada, K. Shimamoto, Inter. J. Adhes. Adhes. **117**(Part B), 103003 (2022)
133. L. Reimer, *Transmission Electron Microscopy*, 4th edn. (Springer, Berlin, 1997), pp. 463–493
134. K. Varlot, J.M. Martin, D. Gonbeau, C. Quet, Polymer **40**, 5691–5697 (1999)
135. K. Varlot, J.M. Martin, C. Quet, Micron **32**, 371–378 (2001)
136. K. Varlot, J.M. Martin, C. Quet, J. Microsc. **191**, 187–194 (1998)
137. R. Brydson, *Electron Energy Loss Spectroscopy* (Taylor and Francis, London and New York, 2001), pp. 59–68
138. L. Bourgeois, M. Weyland, A.K. Sikder, K. Saito, A.M. Funston, J.R. Bellare, Polym. Chem. **11**, 5484–5492 (2020)
139. J. Kikuma, B.P. Tonner, J. Electron. Spectrosc. Relat. Phenom. **82**, 53–60 (1996)
140. S. Horiuchi, T. Hanada, M. Ebisawa, Y. Matsuda, M. Kobayashi, A. Takahara, ACS Nano **3**, 1297–1304 (2009)
141. R. Vane, V. Carlino, Microsc. Microanal. **11**, 900–901 (2005)
142. Y. Matsuda, M. Kobayashi, M. Annaka, K. Ishihara, A. Takahara, Langmuir **24**, 8772–8778 (2008)